5-10-2017

FUNDAMENTAL PROPERTIES, ACTIVITY, AND PLANET-HOSTING POTENTIAL OF YOUNG SUNS NEAR EARTH

Nicole E. Cabrera Salazar
Georgia State University

FUNDAMENTAL PROPERTIES, ACTIVITY, AND PLANET-HOSTING POTENTIAL OF YOUNG SUNS NEAR EARTH

by

NICOLE ESTEFANIA CABRERA SALAZAR

Under the Direction of Russel J. White

ABSTRACT

In this dissertation, we conduct a census and assessment of the nearest young Sun-like stars and investigate the potential for finding giant planets orbiting spotted stars using the radial velocity (RV) method at optical and near-infrared wavelengths. Based in part on new spectroscopic measurements conducted here, we have assembled a complete list of 129 young (<150 Myr), nearby Sun-like stars and their fundamental parameters, including rotational and multiplicity information. We also provide a statistical analysis of their stellar parameters, including projected rotational velocity and inclination. Sixteen of these stars have no close companions and have low projected rotational velocities ($v \sin i \leq 10$ km/s) that are ideal for precision RV planet searches. Seven of these rotate nearly edge-on and are ideal targets for upcoming transiting planet searches, assuming low obliquity.

We conduct precision RV planet search of 7 young Sun-like stars using the TRES spectrograph, mounted on the 1.5-m Tillinghast Reflector at the Fred L. Whipple Observatory,

and with the SOPHIE spectrograph, mounted on the 1.93-m Telescope at the *Observatoire de Haute Provence*; we achieve a precision of ∼10 m/s for both. Four stars are identified as having larger RV variations that are periodic, possibly caused by an orbiting companion. However, the RV variations are correlated with asymmetries in the spectral absorption features, which instead suggests that the variations are caused by spots. Nevertheless our observations provide new independent measures of the rotation periods of these stars. Through this analysis we tentatively confirm the planetary companion around BD+20 1790 in the presence of activity. We additionally investigate the use of comparing red orders of the optical spectrum to the blue orders in order to distinguish spots from planets; we find that this method can be effective for observations that span the full wavelength range of the optical. We also investigate our detection limits at optical wavelengths and find that we are sensitive to over 90% of short period giant planets. Next, we assemble the stellar jitter measurements of our stars with previous studies of all Sun-like stars younger than 1 Gyr to investigate how stellar jitter declines with stellar age. We find that stellar jitter decreases with stellar age as $\tau^{0.53\pm0.13}$, similar to the relationship between stellar rotation period and stellar age. The implication is that it will be difficult to find planets orbiting stars younger than 100 Myr without using techniques that mitigate star spot noise.

Furthermore, we present a near-infrared RV search for giant planets orbiting 8 stars observed with CSHELL at the NASA Infrared Telescope Facility (IRTF). Because of the limited wavelength coverage (29 Å) and older (1980s) detector technology, the achieved precision of 200 m/s inhibits finding the majority of exoplanets, but is nevertheless sufficient to identify short-period brown dwarfs for these stars. We also analyze our detection limits at IR wavelengths and find that we are only sensitive to roughly 50% of short period giant

planets. Finally, we present a new orbital solution for V835 Her, a spectroscopic binary with a 3 day orbital period.

INDEX WORDS: young stars, stellar activity, stellar jitter, exoplanets, radial velocity, near-infrared, optical, spectroscopy

FUNDAMENTAL PROPERTIES, ACTIVITY, AND PLANET-HOSTING POTENTIAL OF YOUNG SUNS NEAR EARTH

by

NICOLE ESTEFANIA CABRERA SALAZAR

A Dissertation Submitted in Partial Fulfillment of Requirements for the Degree of

Doctor of Philosophy

in the College of Arts and Sciences

Georgia State University
2016

FUNDAMENTAL PROPERTIES, ACTIVITY, AND PLANET-HOSTING POTENTIAL OF YOUNG SUNS NEAR EARTH

by

NICOLE ESTEFANIA CABRERA SALAZAR

Committee Chair:	Russel J. White
Committee:	Xavier Delfosse
	Carol Paty
	Sebastien Lepine
	Joshua Von Korff

Electronic Version Approved:

Office of Graduate Studies

College of Arts & Sciences

Georgia State University

December 2016

DEDICATION

This dissertation is dedicated to my past self, a brown immigrant girl who did not know that she could be a scientist but whose mother insisted that no barrier could prevent her from realizing her dreams. I honor that young girl's potential, grit, and determination, but most of all her integrity in the face of those who would cruelly and persistently stand in her way. This dissertation is her legacy, an impossible achievement in a world not built for people like her. If you are a brown girl reading this, it is also for you — to show you that you are both worthy and capable of attaining the highest goals, that your ancestors have thrived even if our stories are not told.

I also dedicate this work to Adam Szaruga, my partner and bulwark against the storms of my life. There exist no words to adequately thank you for making my career the utmost priority, sometimes even at your own expense. It is your support that gave me the freedom of mind to see this work to its end, and I will be forever grateful. *Kocham Cię serdecznie.*

Contents

List of Tables

List of Figures

– 1 –

Introduction

Since the discovery of 51 Peg b by Mayor and Queloz in 1995[1], the field of exoplanetology has grown dramatically. NASA's *Kepler* mission alone has facilitated the discovery of thousands of new exoplanet candidates, with a current 2503 unconfirmed Kepler planet candidates in addition to the the 2951 confirmed planets to date (exoplanets.org). With NASA's Transiting Exoplanet Survey Satellite (*TESS*) scheduled for launch next year, the numbers will continue to grow. With such a large sample, we have been able to discover many important statistical relationships that were previously unknown, such as the frequency-metallicity relationship for giant planets (Santos et al. 2004; Valenti & Fischer 2005), the occurrence rate for giant planets (Cumming et al. 2008), and the occurrence rate for Earth size and Earth-mass planets (e.g. Howard et al. 2010; Mayor et al. 2011; see Annual Review by Winn & Fabrycky 2015).

These statistics indicate processes unexplained by our understanding of the Solar System, which for centuries was the only planetary system available for study. Yet as much information as we have gleaned from these systems, the vast majority of exoplanet surveys to date have focused on Sun-like stars older than 1 Gyr. As discussed in detail below, young stars are typically avoided in exoplanet searches for two reasons. First, stars are only young for a short period of time ($\lesssim$ 30 Myr for the Sun, compared to its $\sim$ 10 Byr main sequence lifetime), therefore they are more rare and on average more distant. Young stars are often more rapidly rotating as well; this rotation creates surface activity in the form of spots, plages, and flares, which combine to make measuring precise radial velocities (RV) difficult.

[1]The first exoplanet is now considered to be the one identified in Latham et al. (1989), based on the now more common definition of an exoplanet ($m \sin i < 30\, M_{Jupiter}$).

Consequently, most of the conclusions about the statistical distributions of planets around Sun-like stars are made for the specific case of the main-sequence (MS) era, and with a bias toward short-period planets, which are the easiest to identify. Furthermore, phenomena such as the existence of hot Jupiters − planets with masses greater than 0.1 $M_{Jupiter}$ with an orbital period less than 10 days (Wright et al. 2012) − cannot be explained by our current knowledge because we have only a snapshot in time that provides limited insight into the timescales and processes required for such occurrences. Understanding the formation and migration of gas giants is especially important because they are often the 2nd largest dynamical influence in the system.

1.1 How Gas Giant Planets Form and Migrate

At present, the two most likely scenarios for giant planet formation are the Core Accretion and Gravitational Instability theories. Core accretion explains planet formation from the bottom up, with small bodies building up to planetesimals via accretion of rock and ice particles and later hydrogen and helium gas (e.g. Pollack et al. 1996). This theory can explain the increasing frequency of giant planets with stellar metallicity (a higher abundance of metals in the protoplanetary disk equates to more solid material available for accretion), however it would take longer to form planets beyond 10 AU than the disk dissipation timescale. Planets formed by gravitational instabilities, on the other hand, are produced by the gravitational fragmentation and collapse of dense pockets in the protoplanetary disk, a small-scale analog of star formation (Boss 1997). This process can form planets well within the disk lifetime, but requires a more massive disk, which would need to cool quickly to enable fragmentation.

The current known statistics on exoplanets, because they apply only at billion-year ages, do not allow us to distinguish between these two formation scenarios.

Obtaining a complete picture of hot Jupiters' early stages also involves understanding how they arrive at such close orbits. Giant planets are likely to form beyond the snow line – the distance from a star at which water and other molecules can exist as ices – where large amounts of gas can be accrued with less disturbance from strong stellar winds typical at young ages (Martin & Livio 2012). This means hot Jupiters must migrate toward their parent star after forming, which could be explained in a number of ways. Disk migration, which occurs when angular momentum is transferred between the giant planet and gas in the disk, is currently held to be the most effective explanation for migration. This process depends on the the timescale of disk dissipation, which is cleared out within $\sim$ 10 Myr. However, gravitational interactions with other planets in the system (dynamical scattering) or with a nearby stellar companion (Kozai cycles) could also contribute to migration but have much longer timescales ($\sim$ 100 Myr; Fabrycky & Tremaine 2007). It seems clear that the way answer both the questions of giant planet formation and migration is to go "back in time" – that is, to conduct a statistical survey of young stars in search of planetary companions.

1.2 The Challenges of Finding Young Planets

To begin addressing questions of formation, some recent work has targeted young stars in search of planets through radial velocity (RV) surveys but encountered several difficulties. Two troublesome characteristic of young stars is that they are both heavily spotted and relatively rapid rotators. Compared to their MS counterparts, the cool surface spots typical of

young stars causes their brightness to vary, and can make identifying transiting planet more challenging. These spots can also produce periodic radial velocity (RV) variations similar to those that a planet would induce (Queloz et al. 2001). Furthermore, absorption line broadening from rapid rotation limits the precision at which we can detect possible companions (e.g. Weise et al. 2010). Intrinsic RV variations caused by stellar activity, whether from spots, plages, or flares, is referred to as the stellar jitter (e.g. Boisse et al. 2011).

Research over the last decade has revealed that for observations in the near-infrared (NIR), the contrast between the stellar surface and cool spots is significantly reduced (by a factor of 3-5), minimizing the effect on the measured RV signal (Bailey et al. 2012). Still, the NIR RV amplitude may be too large for most active stars, and could mask the signal of a planet. Comparing optical with red and/or NIR observations could help distinguish between stellar activity and an orbiting companion, as the activity signal is wavelength-dependent while that of companions is not (Mahmud et al. 2011). RV variations that exhibit the same period in the optical and NIR, but have different amplitudes must be associated with stellar activity. In principle these "false" signals could be subtracted to probe possible planetary variations beneath, as periodic signals of similar amplitudes in both wavebands are most likely caused by a companion (e.g. Donati et al. 2015, 2016).

1.3 Recent Discoveries of the Youngest Planets

The interest in young planets and their potential for explaining giant planet formation has led to two significant discoveries this year. The first is K2-33b, a Neptune-sized planet orbiting a 5-10 Myr star at 1/20th the Earth-Sun distance, discovered independently by both David et al. (2016) and Mann et al. (2016). Unfortunately the mass of the planet

cannot be determined because the host star is too spotted to detect an RV signature of the planet. This discovery was made based on multiple transits seen with Kepler-2 (K2) photometric data.

Donati et al. (2016) discovered V830 Tau b, to date the youngest known hot Jupiter orbiting a 2 Myr, Solar-mass star. This planet was discovered with high resolution spectra from the MaTYSSE Large Program, using a sophisticated Doppler Imaging technique to reconstruct the stellar surface spots and other markers of activity. In this case, the RV signal was only identified after removing a star spot signal that is 10 times larger; longer term monitoring of this unusual case would provide a valuable confirmation.

While these two discoveries are encouraging efforts toward understanding the mechanisms of giant planet formation, migration, and their timescales, they emphasize the extreme challenge of targeting the very youngest stars. A better, more effective approach may be to conduct an exoplanet survey of slightly older "adolescent age" stars (e.g. $\gtrsim$ 10 Myr).

1.4 Outstanding Questions and Motivation for This Work

With this brief summary of exoplanet discoveries and planet formation and migration theories in mind, here we summarize four outstanding questions in this field that we address in this dissertation.

What Are the Nearest Sun-like Stars and How Suitable are They for Exoplanet Searches?

An essential aspect of any exoplanet survey is assembling fundamental stellar parameters of the potential planet hosts. Not only does the environment for formation and evolution

of exoplanets depend completely on the host star, certain stellar properties can inhibit exoplanet detection. Thick disks can obscure planets orbiting the youngest stars, light from stellar companions can contaminate data meant for planet detection, and fainter stars require longer exposures or observation time with larger telescopes, which is challenging to acquire. Knowing the properties of potential planet hosts saves precious telescope time by allowing the observer to be selective of the stellar sample. Most importantly, a census of the nearest young Suns establishes a solid foundation for the exoplanet searches of the future.

How Effective Are Spectroscopic Activity Diagnostics at Distinguishing Planets From Spots?

False RV modulations induced by stellar spots can mimic those caused by a true planetary companion (e.g. Queloz et al. 2001), and thus it is necessary to be able to distinguish one from the other. Comparing the periodicity of measured RV variations to the phase of stellar rotation can be useful, but only if the rotation period is known; many young stars do not have reliable rotation periods listed in the literature because of the difficulty and high observational cost of monitoring young stars photometrically. Another way to test for activity is to compare the RV variations to the asymmetry of stellar absorption lines or to the width of absorption lines, both of which may vary in the presence of star spots. A negative correlation has been shown to exist between the RV and bisector span if activity is present; however, the usefulness of this metric for stars with projected rotational velocities greater than the resolution element of the spectrograph, which is common for young stars, is not well known.

How Effective Are Multiwavelength Observations at Distinguishing Planets from Spots?

Comparing RVs taken in the optical wavelength regime to RVs in the near-IR is also a useful tool, as effects from spots are wavelength dependent while those from planetary companions are not. In fact, a few would-be discoveries of young exoplanets observed in the optical have been refuted by near-IR studies, such as the famous case of TW Hydra (Setiawan et al. 2008; Huélamo et al. 2008). However, these comparisons have been made with data taken months apart, during which the topology of the surface spots could have evolved. Obtaining observing time simultaneously or contemporaneously on two different telescopes to observe young stars at optical and NIR wavelengths would be ideal. Unfortunately, this can be difficult to accomplish because of telescope overprescription as well as scheduling constraints. Additionally, the concept of separating optical spectra into their blue and red orders for similar comparisons has been proposed but its effectiveness has not yet been tested.

An additional challenge of multi-wavelength monitoring is that IR instrument technology has historically lagged behind that of the optical, making IR observations less precise and detailed comparisons between the two wavelengths difficult. Recent advancements in IR detectors as well as methods of wavelength calibration in this regime have opened a new route through which to pursue high-precision RV measurements of young stars, although most have focused on lower mass stars (e.g. K and M spectral type). This is because of the appeal of finding smaller, perhaps even Earth-mass companions, which are easier to detect around lower-mass stars due to the increased reflex motion resulting from a higher planet-star mass ratio. Compared to more massive stars, the Habitable Zone (HZ) – the distance range in which liquid water can exist on the surface of a planet – is closer to the star in K

and M dwarf systems because these dwarfs have cooler surface temperatures, which means potentially habitable planets are more easily detected around these stars. Thus, because most IR spectroscopic work has focused on lower-mass stars, comparatively little RV work in the near-IR has been done on young Sun-like stars, so the effectiveness of this method for mitigating activity effects has not been well documented.

How Does the Radial Velocity Noise Caused by Star Spots Vary with Age?

Previous studies have attempted to define how stellar rotation and activity change over time. Skumanich (1972) famously derived a relationship between the rotational velocities of stars and their ages, which falls off as $\sim \tau^{1/2}$, and numerous studies have shown that slower rotation translates to less activity (e.g. Mamajek & Hillenbrand 2008). Because of this, we would expect a similar decline in the RV noise induced by stellar activity, but the functional form of this has never been investigated. Because stellar jitter is a limiting factor for measuring precise RVs, knowing the relationship between stellar jitter and stellar age is important for assessing how effective young exoplanet searches will be.

In this work, we begin to probe these questions by assembling a list of the nearest young, Sun-like stars and their fundamental parameters. In Chapter 2 we provide an overview of their rotational properties, multiplicity, and inclinations - the characteristics most salient to exoplanet searches. In Chapter 3, we present new optical RV spectroscopic observations of young Sun-like stars obtained with the TRES spectrograph at the Fred L. Whipple Observatory and also with the SOPHIE spectrograph at the Observatoire de Haute Provence. An analysis of their RVs and stellar activity is presented in Chapter 4 along with an analysis

of chromatic effects of activity at two optical wavelength regions. We also compile measurements of the stellar jitter from multiple young star surveys from the literature and explore its dependence on stellar age in Chapter 5. Finally, in Chapter 6 we present the results of our NIR survey of young stars obtained with the CSHELL spectrograph at the NASA Infrared Telescope Facility (IRTF). A summary of the seminal results is presented in Chapter 7.

– 2 –

Nearby Sun-like Stars

The first steps in an effort to find planets orbiting young Sun-like stars involves a complete assessment of the population amenable to survey work. The nearest young Sun-like stars, such as those in nearby young moving groups (d < 100 pc; Zuckerman & Song 2004), are especially advantageous as their proximity allows us to examine them in better detail than those in the nearest star forming regions (d > 100 pc; e.g. Taurus-Auriga, Torres et al. 2009).

Of the 9 well established young moving groups assembled in Torres et al. (2008), whose estimated ages range from 10 to 150 Myr (Bell et al. 2015), 4 have mean distances within 50 parsecs (pc) of the Sun: AB Doradus (AB Dor), β Pictoris (β Pic), TW Hydrae (TWA), and Tucana Horologium (Tuc Hor). According to the list assembled by Torres et al. (2008), the vast majority (83%) of TWA members are M dwarfs; just two TWA members of spectral type K5 fit our definition of a Sun-like star. Thus, only the moving groups AB Dor, β Pic, and Tuc Hor, with respective ages of 149^{+51}_{-19} Myr, 24±3 Myr, and 45±4 Myr (Bell et al. 2015), were considered in the present study.

For these 3 moving groups we first identified all known members, from which we selected the Sun-like members. Moving group membership for β Pic and AB Dor was obtained from Torres et al. (2008) and from the updated list by McCarthy & White (2012); membership for Tuc Hor was also obtained from Torres et al. (2008) and supplemented by Kiss et al. (2011) and Zuckerman et al. (2011). Spectral types for AB Dor and β Pic members were those assembled in McCarthy & White (2012), while those for Tuc Hor members are mostly

from Zuckerman et al. (2011) and Torres et al. (2008); two stars in Tuc Hor have spectral types from Kiss et al. (2011).

For the purposes of this study, we consider stars to be Sun-like if they have spectral types between F6 and K5 (inclusive). We adopted the use of spectral types for this classification since that information is available for all members. We note that this spectral type range roughly corresponds to a mass range of 1.3 - 0.7 $M_{\odot}$ (e.g. Gray 2008). The 129 stars meeting this Sun-like criterion from AB Dor, β Pic, and Tuc Hor are listed in Tables 2.1 - 2.3. For each star, we provide its Henry Draper number (HD), Hipparcos number (HIP), and common name. Spectral types are listed from the references noted above.

Stellar distances were obtained in most cases using *Hipparcos* parallaxes (van Leeuwen 2007), and in other cases calculated based on an assumed stellar radius and temperature (see McCarthy & White 2012). K magnitudes were obtained from the 2MASS catalog (Cutri et al. 2003), while B and V magnitudes are mostly from the *Tycho-2* catalog (Høg et al. 2000).

Table 2.1. Young Sun-like stars in AB Doradus[a]

HD	HIP	Other	SpT[b]	Distance[c]	K[d]	$B-V$[e]	$v \sin i$	$v \sin i$[f]	P_{rot}[g]	Known[h]	Mult.[i]
				(pc)	(mag)		(km/s)	Ref.	(d)	Mult.	Ref.
1405	···	PW And	K2	27	6.387	1.159	21	H07	1.762	S	L07,NC10,E12
4277 A	3589 A	BD+54 144 A	F8	48.6H	[6.361]	0.668	35	H07	···	B	E12
6569	5191	BD-15 200	K1	50.0H	7.340	1.075	4.4	M14	7.13	S	E12
···	6276	BD-12 243	G9	35.1H	6.549	0.996	4.2	W10	···	S	E12
···	···	TYC 1752-63-1	K5	38.5	7.642	2.529	···	···	···	···	MW12
···	···	CD-46 644 A	K3	70	[8.614]	2.140	36	M10	1.116	V: 21.7	M10
13482	10272	BD+23 296 A	K1	32.3H	[5.727]	0.938	6	H07	6.13	B	M10
···	···	BD+23 296 B	K4:	32.3*	···	1.434	···	···	6.13	B: 1.8	T08
16760 Aa	12638 Aa	BD+37 604 Aa	G2	50.2H	[7.033]	0.847	3	H07	···	T	E12
16760 B	12635 B	BD+37 604 B	K2	44.9H	7.762	1.237	···	H07	···	T: 14.6	2M, E12
17332 A	13027 A	BD+18 347 A	G1	32.6H	5.517	0.730	15.5	C03	···	B	E12
17332 B	13027 B	BD+18 347 B	G6	32.6*	5.636	0.902	···	C03	···	B: 3.6	E12
19668	14684	IS Eri	G5	40.2H	6.701	0.970	7.1	W10	5.46	S	E12
···	14809	BD+21 418 A	G1	49.4H	6.968	0.764	7.6	M14	···	T	E12
···	14807 A	BD+21 418 Ba	K6	51.7H	[7.652]	1.452	···	···	···	T: 33.1	E12
···	···	HW Cet	K4:	46c	8.019	1.405	···	···	···	···	MW12
21845 A	16563 A	V577 Per A	G5	33.8H	6.370	0.878	8.9	M14	1.43	B	NC10,E12
24681	···	BD-02 754	G8	53	7.253	0.909	···	···	···	···	MW12
25457	18859	BD-00 632	F8	19.2H	4.181	0.607	23.86	W07	···	S	L07,NC10,E12
25953	19183	BD+01 699	F7	55.3H	6.582	0.601	30	H07	···	S	E12
···	···	TYC 0091-0082-1	K0	37c	8.645	0.910	···	···	···	···	MW12
31652	···	BD-09 1034	G8	88	8.352	0.977	5.7	M14	···	···	MW12
···	···	CD-40 1701	K4:	42	8.050	1.136	6.8	M10	6.53	S	M10
32981	···	BD-16 1042	F9	81	7.743	0.771	···	···	0.985	S	M10
293857	···	BD-04 1063	G8	78	7.360	0.934	8.6	M14	···	···	MW12
33999 A	···	CD-34 2128 A	F8	106	[7.20]*	0.677	2	H07	···	T	···
36705 A	25647	AB Dor A	K0	14.9H	[4.686]	1.033	···	···	0.514	Q	M10
···	···	UX Col	K3	57	7.759	1.451	41.5	M10	2.29	S	M10
···	···	CD-34 2331	K3	78	9.122	1.394	···	···	7.82	S	M10
37572 A	26373 A	UY Pic A	K0	23.9H	5.811	1.071	9	H07	4.52	B	NC10
37572 B	26369 B	UY Pic B	K6	24.3H	6.61*	1.515	···	H07	4.52	B: 18.3	2M
37551 A	26401	WX Col A	G7	74.7H	7.663	0.889	3	H07	···	B	M10
37551 B	26401 B	WX Col B	K1	74.7*	7.865	1.168	···	···	···	B: 3.9	T08
···	···	Parenago 2752	G8	116	9.138	0.798	···	···	···	···	MW12
···	···	CPD-19 878	K1	71	8.116	1.109	···	···	1.49	···	MW12
···	···	TYC 7605-1429-1	K4	128	9.120	1.120	···	···	2.75	S	M10
···	···	CD-26 2425	K2	70	8.468	1.119	···	···	1.83	···	MW12
39576	27727	TZ Col	G3	87.6H	7.517	0.777	···	···	2.84	···	MW12
···	···	TY Col	G6	68	7.628	0.928	55	M10	3.73	S	M10
···	···	BD-13 1328	K4	39	7.769	1.405	···	···	···	···	MW12
···	···	CD-34 2676	G9	72	8.195	1.028	18.1	W10	3.38	S	M10
45270 A	30314	CD-60 1425 A	G1	23.5H	[5.045]	0.731	17.2	W10	···	S*	NC10
48189 A	31711	AK Pic A	G2	21.7H	[4.544]	0.689	16.5	W10	2.6	B	NC10
48189 B	31711 B	AK Pic B	K5:	21.7*	···	1.531	···	W10	2.6	B: 0.8	T08
···	···	TYC 7627-2190-1	K2	78	8.814	1.528	···	···	2.67	···	MW12
···	···	GSC 8544-1037	K4	143**	8.925	0.900	7	M10	6.05	S	M10
···	···	CD-57 1654	G2	103	8.931	0.876	29.2	M10	2.94	S	M10
···	···	BD+20 1790	K5	26	6.879	1.394	12.85	W07	2.79	S	E12
59169 A	36108	CD-49 2843 A	G7	118H	[7.928]	0.554	···	···	3.89	B	M10
59169 B	36108 B	CD-49 2843 B	K3:	118*	···	1.315	···	···	3.89	B: 1.2	T08
···	···	CD-84 80	G9	71	7.906	1.070	7.7	W07	4.94	S	M10
64982 A	37855 A	CD-79 300 A	G0	83.5H	[7.586]	0.665	···	···	···	B	···
···	···	BD-07 2388	K1	93	6.917	1.007	···	···	···	···	MW12
···	···	CD-45 5772	K4	70	8.068	1.612	···	···	···	···	MW12

Table 2.1 (cont'd)

HD	HIP	Other	SpT[b]	Distance[c]	K^d	$B-V^e$	$v \sin i$	$v \sin i^f$	$P_{rot}{}^g$	Known[h]	Mult.[i]
				(pc)	(mag)		(km/s)	Ref.	(d)	Mult.	Ref.
113449 A	63742 A	PX Vir A	K1	22.1H	[5.509]	1.094	18.04	W07	6.54	B	M10
139751 A	76768	BD-18 4125 A	K5	42.6H	[6.948]	1.714	···	···	3.7	B	M10
152555	82688	BD-04 4194	G0	47.6H	6.363	0.737	17.8	W10	···	S	E12
317617	···	TYC 7379-279-1	K3	56	7.669	1.201	4	M10	···	···	MW12
159911	···	BD-13 4687	K4	45	6.835	1.372	···	···	0.447	S	M10
176367 A	93375 A	CD-28 15269 A	G1	62.8H	7.151	0.716	17	H07	···	B: 11.2	T08
178085	94235	CD-60 7126	G1	57.2H	6.881	0.775	24	C03	2.24	B	M10
···	···	TYC 486-4943-1	K3	71	8.656	1.114	11	M10	1.35	S	M10
189285	···	BD-04 4987	G7	95	7.841	0.926	···	···	4.85	S	M10
···	···	BD-03 4778	K1	70	7.921	1.502	8	M10	4.68	S	M10
199058	···	BD+08 4561	G6	75	6.965	0.809	···	···	···	···	MW12
···	···	TYC 1090-543-1	K4	75	8.823	1.639	18	M10	2.28	···	MW12
···	106231	LO Peg	K5	25.1H	6.382	1.258	···	···	0.42312	S	NC10, E12
207278	107684	CD-40 14502	G7	83.7H	7.979	0.868	11.2	W10	4.14	S	M10
217343	113579	CD-26 16415	G5	32.0H	5.943	0.775	10.56	W07	2.169	S	E12
218860 A	114530	CD-45 14955 A	G8	50.6H	7.032	0.882	7	H07	5.17	B	M10
···	115162	BD+41 4749	G4	49.4H	7.224	0.915	4.4	M14	···	S	E12
222575	116910	CD-36 15990	G8	62.3H	7.624	0.843	···	···	2.294	S	M10
224228	118008	GJ 4377	K2	22.1H	5.907	1.233	2.7	W10	···	S	NC10, E12

Note. —

[a] SpT, Distance, and K were assembled from McCarthy & White (2012).

[b] Only stars with known spectral types are shown. Spectral types followed by a colon are estimated from B-V color.

[c] Distances marked with an H are from Hipparcos parallax measurements, those marked with an asterisk are assumed to be that of their companion, and those marked with a "c" are calculated based on an assumed radius and temperature (see McCarthy & White 2012). The distance for GSC 8544-1037 was determined by Messina et al. (2010).

[d] K magnitudes were assembled from the 2MASS catalog (Cutri et al. 2003). Values in brackets indicate measurements that may be biased by a spatially unresolved companion.

[e] B magnitudes are mostly from the *Tycho-2* catalog (Høg et al. 2000). The B magnitude for GSC 8544-1037 was determined by Messina et al. (2010).

[f] $v \sin i$ References: H07 = Holmberg et al. (2007); M14 = McCarthy & Wilhelm (2014); W10 = Weise et al. (2010); M10 = Messina et al. (2010); C03 = Cutispoto et al. (2003); W07 = White et al. (2007).

[g] Rotation periods were assembled from Messina et al. (2010).

[h] Multiplicity abbreviations: S = Single, B = Binary, T = Triple, Q = Quadruple; HD 45270 A is a wide binary according to Torres et al. (2008).

[i] Multiplicity References: L07 = Lafrenière et al. (2007); NC10 = Nielsen & Close (2010); E12 = Evans et al. (2012); MW12 = McCarthy & White (2012); M10 = Messina et al. (2010); T08 = Torres et al. (2008); 2M = 2MASS.

Table 2.2. Young Sun-like stars in β Pic[a]

HD	HIP	Other	SpT[b]	Distance[c]	K[d]	$B-V$[e]	$v \sin i$	$v \sin i$[f]	P_{rot}[g]	Known[h]	Mult.[i]
				(pc)	(mag)		(km/s)	Ref.	(d)	Mult.	Ref.
···	···	BD+17 232 A	K3	52.6	[6.72]	1.303	···	···	···	B	···
···	···	BD+17 232 B	K5	52.6	···	1.514	···	···	···	B: 1.8	M00
14082 A	10680	BD+28 382 A	F8	39.4	5.79	0.62	45	H07	···	B	E12
14082 B	10679	BD+28 382 B	G1	34	6.26	0.767	8	H07	···	B: 13.8	2M
15115	11360	BD+05 338	F8	44.8	5.82	0.47	···	···	···	···	MW12
···	···	TYC 7558-655-1	K5	35.7	7.23	1.377	···	···	8.8	···	MW12
35850 A	25486 A	AF Lep A	F7	26.8	[4.93]	0.648	55.18	W07	···	B	E12
45081	29964	AO Men	K4	38.5	6.81	1.371	15.9	W10	2.67	S	B07,K07,NC10
139084 A	76629 A	V343 Nor A	K0	39.8	5.85	1.052	16	H07	4.3	B	NC10
155555 A	84586 A	V824 Ara A	G7	31.4	[4.70]	1.008	40	H07	1.688	T	B07,NC10
···	···	CD-54 7336	K1	66	7.36	1.06	35.5	M10	1.819	S	M10
160305	86598	CD-50 11467	F9	76	6.99	0.675	···	···	1.341	···	MW12
161460 A	···	CD-15 7414 A	K0	74	[6.78]	1.068	10.1	W10	2.61	B	M10
164249 A	88399 A	CD-51 11312 A	F6	46.9	5.91	0.513	21	H07	···	B	M10
168210	89829	CD-29 14813	G5	75.5	7.05	0.78	114.7	M10	0.57	S	M10
172555 B	92024 B	CD-64 1208 A	K5	29	[6.10]	1.23	···	···	0.345	T;AB:0.18	M10
174429 A	92680 A	PZ Tel A	G9	49.7	6.37	···	69	M10	0.997	B	NC10
···	···	CD-26 13904 A	K4	80	[7.37]	1.087	9.8	M10	5.65	V: 1.1	M10
181327	95270	Eta Tel C	F6	50.6	5.91	0.551	18	H07	···	···	MW12
199143 A	103311 A	BD-17 6127 A	F7	47.7	[5.81]	0.626	115.8	W07	···	B	NC10

Note. —
[a] SpT, Distance, and V were assembled from McCarthy & White (2012).
[b] Only stars with known spectral types are shown.
[c] Distances marked with an H are from Hipparcos parallax measurements, those marked with an asterisk are assumed to be that of their companion, and those marked with a "c" are calculated based on an assumed radius and temperature (see McCarthy & White 2012).
[d] K magnitudes were assembled from the 2MASS catalog (Cutri et al. 2003). Values in brackets indicate measurements that may be biased by a spatially unresolved companion.
[e] B magnitudes are mostly from the *Tycho-2* catalog (Høg et al. 2000). The B magnitude for HD 172555 B was determined by Torres et al. (2008).
[f] $v \sin i$ References: H07 = Holmberg et al. (2007); W07 = White et al. (2007); M10 = Messina et al. (2010); W10 = Weise et al. (2010). [g]Rotation periods were assembled from Messina et al. (2010).
[h] Multiplicity abbreviations: S = Single, B = Binary, T = Triple, Q = Quadruple.
[i] Multiplicity References: M00 = Morlet et al. (2000); E12 = Evans et al. (2012); 2M = 2MASS; MW12 = McCarthy & White (2012); B07 = Biller et al. (2007); K07 = Kasper et al. (2007); NC10 = Nielsen & Close (2010); M10 = Messina et al. (2010).

Table 2.3. Young Sun-like stars in Tucana Horologium[a]

HD	HIP	Other	SpT[b]	Distance	K^c	$B-V^d$	$v \sin i$	$v \sin i^e$	$P_{rot}{}^f$	Known[g]	Mult.[h]
				(pc)	(mag)		(km/s)	Ref.	(d)	Mult.	Ref.
17250	12925	BD+04 439	F8	63	6.517	0.608	···	···	···	Q	R15
20121	14913	CD-44 1025	F6	44	4.827	0.674	···	···	···	T; AB:0.7	Z11
23524	17782	BD+51 777	G8	51	6.747	0.948	9	H07	···	B: 0.36	Z11
36869	···	AH Lep	G3	59	6.852	0.718	27.34	LS10	···	···	···
38397	26990	CD-39 2142	G0	52	6.756	0.742	15.9	W10	···	S	M16
41071	28474	CD-44 2382	G8	54	7.321	0.884	8	H07	···	···	···
155915	84642	V857 Ara	G8	55	7.527	0.978	11.3	T06	···	B: 0.22	C10
···	···	BD+44 3670	G2	65	6.947	0.722	···	···	···	···	···
25402	18714	CD-42 1335 A	G3	48.5	6.875	0.590	5	H07	···	S	M16
105	490	CD-42 16587	G0	40	6.117	0.696	18.19	W07	···	S	M10
987	1113	CD-75 4	G8	44	6.962	0.882	7.3	W10	3.72	S	M10
1466	1481	CD-64 6	F8	41	6.149	0.660	22.7	W10	···	···	···
3221	2729	TYC 8841-652-1	K4	46	6.533	1.506	122.8	M10	0.37	S	M10
···	···	CD-78 24	K3	50	7.529	1.501	19.5	M10	2.57	S	M16
8558	6485	CD-58 290	G7	49	6.847	0.860	13.8	M10	3.59	S	M10
9054	6856	CC Phe	K1	37	6.834	1.505	2.7	T06	···	S	M10
12039	9141	DK Cet	G4	42	6.472	0.223	13.46	W07	3.02	V: 0.2	M10
13183	9892	CD-53 410	G7	50	6.894	0.865	23	C03	2.24	B	M10
13246	9902	CD-60 415	F7	45	6.204	0.629	35.6	T06	···	···	···
···	···	CD-60 416	K5	48	7.537	0.946	10.8	T06	···	V*	M10
···	···	CD-58 553	K5	50	7.784	1.411	5.6	M10	7.38	S	M10
···	···	CD-46 1064	K3	44	7.103	1.434	10	M10	3.74	S	M10
22213	···	BD-12 674	G7	48	6.790	0.873	···	···	···	···	···
22705	16853	CD-50 1090	G2	42	6.137	0.705	19	M10	···	B*	M10
···	···	BD-12 943	K0	69	7.765	0.971	···	···	···	···	···
29615	21632	CD-27 1816	G3	55	6.866	0.747	17.53	M10	4.25	S	M10
32195	22295	CD-80 167	F7	60	6.868	0.637	60	H07	···	···	···
···	···	BD-20 951	K1	72	7.331	0.899	···	···	5.2	···	···
···	···	BD-19 1062	K3	68	8.066	1.204	···	···	4.06	S	M16
···	···	BD-09 1108	G5	78	8.084	0.806	···	M10	2.72	S	M10
···	···	CD-30 2310	K4	65	8.304	1.793	7	M10	1.7	S	M16
202917	105388	CD-53 8813	G7	46	6.908	0.820	14.9	W10	3.36	S	M10
207575	107947	TYC 9116-257-1	F6	45	6.027	0.594	36.5	W10	···	···	···
···	···	CD-86 147	G8	60	7.500	0.904	73.9	T06	2.31	S	M16
222259 A	···	TYC 9339-551-1	G6	46	···	0.691	18.3	M10	2.85	B: 5.3	M10
222259 B	···	TYC 9339-2157-1	K3	46	7.032	0.780	15.5	C03	2.85	B	M10

Note. —

[a] SpT, Distance, and V magnitudes were assembled from: 1) Zuckerman et al. (2011) through BD+44 3670, 2) Kiss et al. (2011) for HD 25402, and 3) Torres et al. (2008) for HD 105 through HD 222259B.

[b] Only stars with known spectral types are shown.

[c] K magnitudes were assembled from the 2MASS catalog (Cutri et al. 2003).

[d] B magnitudes were assembled from the *Tycho-2* catalog (Høg et al. 2000).

[e] $v \sin i$ References: H07 = Holmberg et al. (2007), LS10 = (López-Santiago et al. 2010), W10 = Weise et al. (2010), T06 = (Torres et al. 2006), W07 = White et al. (2007), M10 = Messina et al. (2010), C03 = Cutispoto et al. (2003).

[f] Rotation periods were assembled from Messina et al. (2010).

[g] Multiplicity abbreviations: S = Single, B = Binary, T = Triple, Q = Quadruple. CD-60 416 is a wide companion to HIP 9902 according to Messina et al. (2010); HD 22705 is a wide binary with an astrometric orbit (P = 200 d).

[h] Multiplicity References: R15 = Roberts et al. (2015); Z11 = Zuckerman et al. (2011); M16 = Moór et al. (2016); C10 = Chauvin et al. (2010); M10 = Messina et al. (2010).

2.1 Characteristics of the Nearest Young Sun-like Stars

The compilation of young Sun-like stars in Tables 2.1 − 2.3 provides a snapshot of the properties of Sun-like stars at adolescent ages ($25 - 150$ Myr; (Bell et al. 2015)). This sample consists of 73 stars in AB Dor, 20 in β Pic, and 36 in Tuc Hor. Distances range from 15 pc to 143 pc with a median of 50 pc; 95% of the stars are within 100 pc. V magnitudes range from 5.378 to 13.401 with a median of 9.042.

2.2 Stellar Rotation

Because stellar absorption line broadening from rotation and high stellar activity are important limiting factors for the RV precision that can be obtained, it is necessary to assess the rotation rates of these young Sun-like stars. This is commonly assessed via 2 measures. The first is the amount of spectral line broadening caused by the projected ($\sin i$) rotational velocity (v) of the star. Here i is the inclination of the star's rotation axis, where $i = 0°$ is defined to be pole-on while $i = 90°$ is defined to be edge-on. High dispersion spectra can be used to measure $v \sin i$ (e.g. Gray 2008). The second is a more direct measure of the rotational period (P_{rot}) of a star that can be determined from the brightness variations caused by spots on a star that rotate in and out of our view. It is often easier to measure rotation periods for young stars because they usually have larger spots and a more rapid rotation than old Sun-like stars do (e.g. Meibom et al. 2015).

In Tables 2.1 − 2.3 we have compiled the $v \sin i$ and rotation periods of the nearest young Sun-like stars. Of these 129 stars, only 83 have $v \sin i$ values (64%) and 70 have known rotation periods (54%). Of the stars with known $v \sin i$, 41 are AB Dor members, 14 are β Pic Members, and 28 are Tuc Hor members; this represents 56%, 70%, and 78% of

each group, respectively. Of the stars with known rotation periods, 42 are AB Dor members, 11 are β Pic members, and 17 are Tuc Hor members this represents 58%, 55%, and 47% of each group, respectively.

The distributions of $v \sin i$ for these stars are illustrated in Figure 2.1. The vertical dotted, dashed, and dash-dotted lines in Figure 2.1 represent the median $v \sin i$ for β Pic (35.5 km/s), Tuc Hor (13.8 km/s), and AB Dor (10.6 km/s). We note that these projected rotational velocities decline with age, as expected. Since it is known that for high $v \sin i$ values (>6 km/s) the achievable RV precision declines linearly with increasing $v \sin i$ (Bouchy, Pepe, & Queloz 2001), the achievable RV precision for these stars will be (at best) 10-35 times worse than that of more slowly rotating field stars.

The distributions of P_{rot} for these stars are illustrated in Figure 2.2. The vertical dotted, dashed, and dash-dotted lines in Figure 2.2 represent the median P_{rot} for β Pic (2.42 days), Tuc Hor (3.02 days), and AB Dor (2.94 days). These rotation periods, which are roughly a factor of 10 faster than the Sun's equatorial rotation period (24.5 days), imply that the achievable RV precisions may be much worse since rapidly rotating stars are much more variable (e.g. Saar & Donahue 1997). We also note that these rotation periods are comparable to the orbital periods of hot Jupiters, and may inhibit finding them while young.

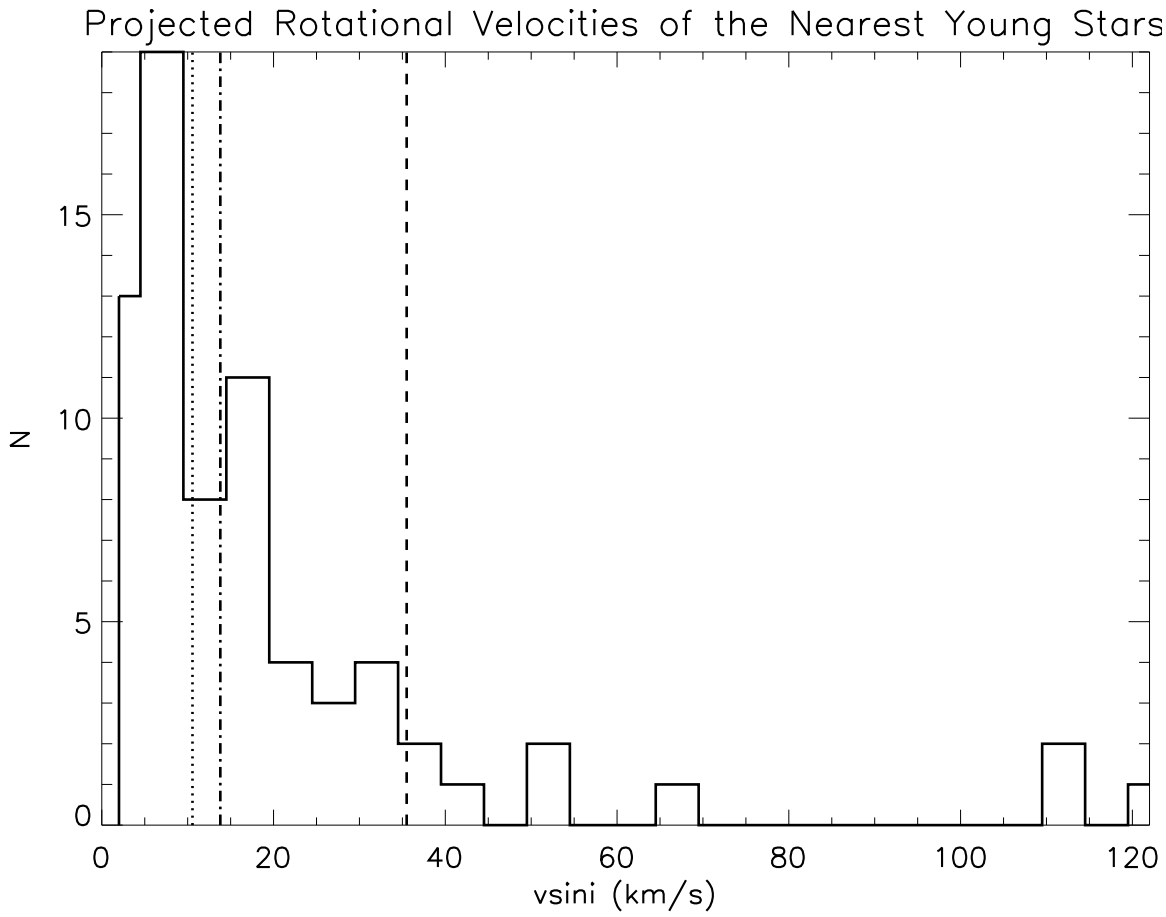

Figure 2.1 Histogram of known projected rotational velocities for Sun-like stars in nearby young moving groups. The dotted, dashed, and dash-dotted lines represent the median $v \sin i$ for AB Dor, β Pic, and Tuc Hor, respectively. Of the 83 stars with known $v \sin i$ represented here, 41 are AB Dor members, 14 are β Pic Members, and 28 are Tuc Hor members.

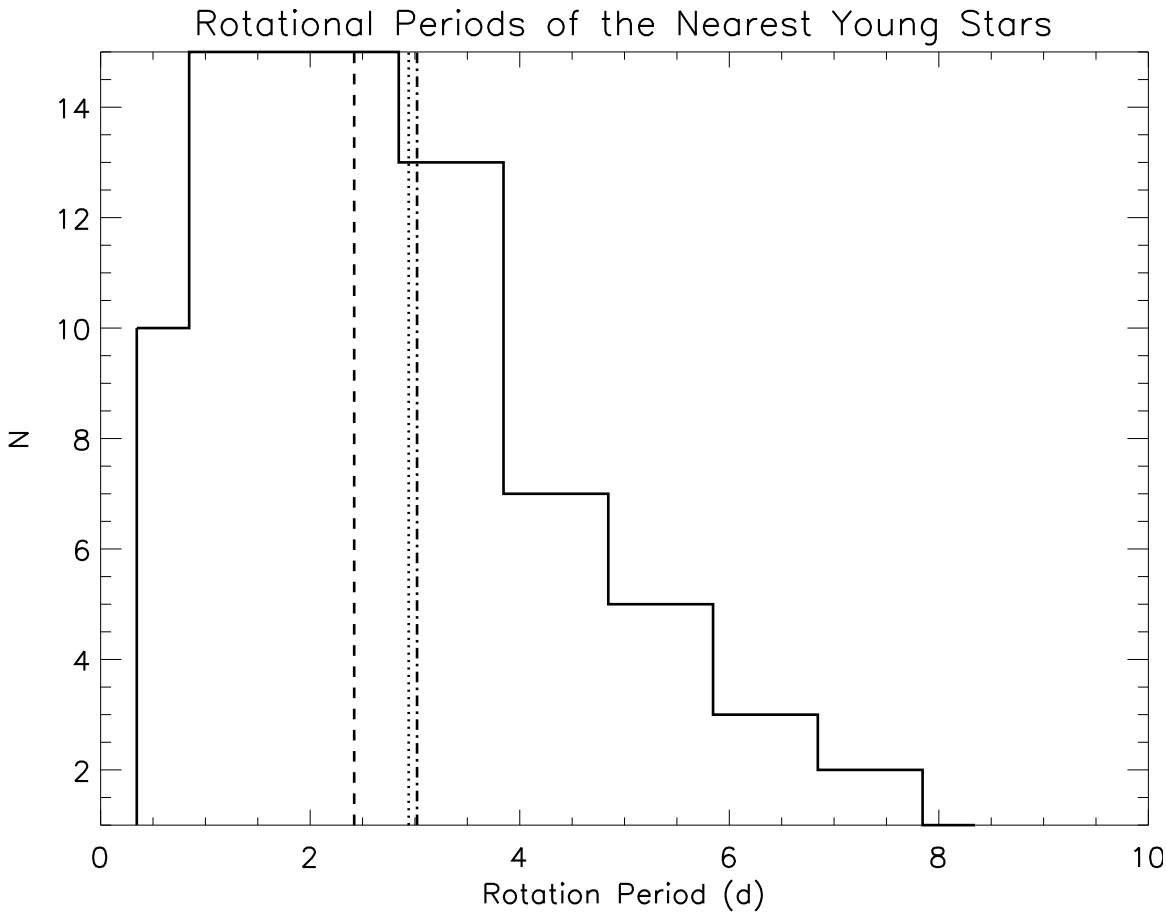

Figure 2.2 Histogram of known rotation periods for Sun-like stars in nearby young moving groups. The dotted, dashed, and dash-dotted lines represent the median rotation period for AB Dor, β Pic, and Tuc Hor, respectively. Of the 70 stars with known P_{rot} represented here, 42 are AB Dor members, 11 are β Pic Members, and 17 are Tuc Hor members.

2.3 Multiplicity

A stellar companion can inhibit planet detection with the RV method if its projected separation is small enough to contaminate the light of the suspected planet host. A separation smaller than the spectrograph slit or fiber would produce a combined spectrum of both stellar components in the spectrograph, making it difficult to extract an accurate RV for the target star. Likewise, the extra light from a stellar companion to a star with a transiting planet will significantly bias the inferred planet properties (Buchhave et al. 2011). Therefore it is helpful to know the stellar multiplicity prior to conducting any exoplanet search. We have provided known multiplicity information for the young Sun-like stars in AB Dor, β Pic, and Tuc Hor as compiled by McCarthy & White (2012) and from the literature; all multiplicity references are listed in Tables 2.1 − 2.3. Two stars were identified as spectroscopic binaries in this study: V835 Her and BD+05 4576 (Chapter 3).Stars are only listed as single if no companion was identified in the high spatial resolution imaging surveys of Kasper et al. (2007), Biller et al. (2010), Nielsen & Close (2010), and Evans et al. (2012).

Projected separations are given for multiples if the pair has been spatially resolved. The separations for pairs closer than 10.0 are as assembled in Torres et al. (2008), while the separation of wider pairs were calculated from the reported positions of the stars in the 2MASS all-sky infrared catalog (Cutri et al. 2003). We note that wide binary companions pose no threat to planet detection with the RV method, as long the individual spectra can be obtained without contamination from the other component.

Of the 20 young Sun-like stars in β Pic, 13 are in multiple systems, compared to 26 of 73 young Sun-like stars in AB Dor and 10 of 36 young Sun-like stars in Tuc Hor. Of these 49 known multiples, only 19 have projected separations that have been measured. These

include 4 members of β Pic, 10 members of AB Dor, and 5 members of Tuc Hor. Of these, there are just 7 systems that are "effectively single" for observational exoplanet searches (projected separations >5), 5 of which are members of AB Dor and 1 each a member of β Pic and Tuc Hor. This list does not include stars for which the multiplicity is unknown.

2.4 Stellar Inclination Angles

If the rotation period P_{rot}, projected rotation velocity $v \sin i$, and the radius of a star R_* are known or can be estimated, the inclination angle of the star's rotation axis (i_*) can be calculated:

$$\sin i_* = \frac{v \sin i P_{rot}}{2\pi R_*} \tag{2.1}$$

This is useful for comparing the rotation axis of the star to the orbital plane of a planetary companion, which is more constrained for transiting planets[1] or for planets detected via astrometry. It is also useful for planets detected by the RV method since, if we suppose that the stellar rotation and planetary orbit are coplanar, we can use this $\sin i$ determine the planet's true mass.

Here we provide a description of how to estimate the sine of the stellar inclination when P_{rot} and $v \sin i$ are available. For now, we calculate $\sin i_*$ rather than taking the inverse of sine to obtain the inclination itself because measurement errors may result in unphysical measurements ($\sin i_* > 1$).

Although P_{rot} and $v \sin i$ for many young stars have been measured (see Tables 2.1 - 2.3), the radii of these stars are not usually measured. While long baseline optical and IR interferometers offer great promise, they have been successful in measuring the radii of

[1]While any transiting planet has an orbital plane nearly along our line of sign, the azimuthal orientation is not known. Thus a star with $i_* = 90^\circ$ and a transiting planet could have a large obliquity

young stars in only a few cases (Simon & Schaefer 2011). In order to estimate the radius, first we determined the $V-K$ color using 2MASS K magnitudes and Tycho V magnitudes. Bolometric luminosities were determined from K magnitudes and a bolometric correction (BC_K) was then obtained from the calibrated color-temperature relations of Houdashelt et al. (2000 , see their Table 5; hereafter HBS00). Using parallaxes obtained from Hipparcos (van Leeuwen 2007), we calculated the target distances. The absolute K magnitudes were then determined via the distance modulus and used to obtain the bolometric magnitudes. The stellar luminosities (L_*) were thus determined, using $\mu_{Sun} = 4.83$.

Next, we used the empirical color-temperature relations from HBS00 in order to estimate the effective stellar temperatures, using the coefficients corresponding to the Johnson-Cousins filter system for dwarf stars ($0.82 \leq (V-K) \leq 3.29$ for spectral types of F2 to K7):

$$T_{eff} = a + b(V-K) + c(V-K)^2, \tag{2.2}$$

with $a = 8686.22$, $b = -2441.65$, and $c = 334.789$. The stellar radii were estimated with the Steffan-Boltzmann law using the calculated values for T_{eff} and L_*. Based on comparisons with directly measured radii using interferometry, McCarthy & White (2012) determined that this prescription provides a stellar radius estimate that is accurate to $\pm 8\%$. We adopt this uncertainty for our radius estimate.

$v \sin i$ values were obtained from the following sources: Holmberg et al. (2007), Weise et al. (2010), White et al. (2007), Messina et al. (2010), and Cutispoto et al. (2003). Not every star has a listed $v \sin i$ uncertainty, but the 8 stars with $v \sin i$ uncertainties have values of <3 km/s. We adopted for all the stars a 10% $v \sin i$ uncertainty, which is listed as the typical value in Messina et al. (2010), our main source for $v \sin i$.

With these quantities, Equation 2.1 can be used to estimate $\sin i_*$. Of equal importance is the uncertainty in $\sin i_*$, which can be expressed in terms of the uncertainties in the 3 quantities:

$$\left(\frac{\sigma_{\sin i_*}}{\sin i_*}\right)^2 = \left(\frac{\sigma_{v \sin i_*}}{v \sin i_*}\right)^2 + \left(\frac{\sigma_{P_{rot}}}{P_{rot}}\right)^2 + \left(\frac{\sigma_R}{R}\right)^2 \tag{2.3}$$

These stars are listed in Table 2.4 along with the measured $v \sin i$ and P_{rot} values, calculated radii, and $\sin i_*$ values. Since it is easier to visualize the geometry of an inclination angle rather than the sine of that inclination, we also calculate a direct inclination i_* for comparison. As both P_{rot} and $v \sin i$ values are needed to calculate a star's inclination angle, only 16 nearby young Sun-like stars fit this criterion.

The calculated $\sin i_*$ values range from 0.14 to 3.31, and have uncertainties that range from 0.128 to 0.151. Six stars have $\sin i_*$ values that are > 1.0 and therefore have i_* values that are unphysical. We suspect that in most cases this is a consequence of the stellar radius being underestimated since it is the most difficult to determine accurately. We consider these 6 systems to have "edge-on" (i.e. 90°) orientations. One other star has an i_* within 20° of 90°; thus, there are a total of 7 nearly edge-on systems. The median $\sin i_*$ has a value of 0.80, and an uncertainty in this median of 0.2. This corresponds to a median inclination of $i_* = 53.1°$, with 1σ limits of $i_* = -0.32°$ and $i_* = 0.32°$.

For a small sample of stars with random orientations, the median $\sin i_*$ should be 0.866, corresponding to $i_* = 60°$. This is statistically consistent with the values measured here. However, as discussed in Morton & Winn (2014), observational uncertainties often bias inclination estimates toward small values (see the discussion of their Figure 2). This illustrates their point, and exemplifies the challenge of estimating the inclination of an individual

Table 2.4. Inclination Angles of Young Nearby Suns

Name	Moving Group	V-K	SpT[a]	$v \sin i$[b] (km/s)	$v \sin i$[c] Ref.	P_{rot}[d] (d)	P_{rot}[e] Ref.	L_{bol}[f] ($L_\odot$)	R_*[g] ($R_\odot$)	$\sin i$	$\sin i_{unc}$	i[h] (°)
HD 13482	AB Dor	2.205	K1	6.0	H07	6.13±0.03	M10	1.46	0.76	0.96	0.132	73.74
IS Eri	AB Dor	1.791	G5	7.1	W10	5.46±0.08	M10	2.57	1.3	0.59	0.151	36.12
HD 37572 A	AB Dor	2.098	K0	9.0	H07	4.52±0.02	M10	0.44	2.1	0.38	0.13	22.47
HD 48189 A	AB Dor	1.713	G2	16.5	W10	2.6±0.02†	C99	0.97	0.44	1.91	0.13	[90]
HD 113449 A	AB Dor	2.191	K1	18.04	W07	6.54±0.02†	G00	0.43	2.17	1.07	0.13	[90]
HD 207278	AB Dor	1.635	G7	11.2	W10	4.14±0.02	M10	0.18	0.62	1.48	0.13	[90]
HD 217343	AB Dor	1.541	G5	10.56	W07	2.169±0.007	M10	1.04	0.7	0.65	0.128	40.64
HD 218860 A	AB Dor	1.771	G8	7.0	H07	5.17±0.02	M10	0.3	0.95	0.76	0.13	49.2
V577 Per A	AB Dor	1.88	G5V	7.0	M10	1.43±0.006	M99	1.28	1.41	0.14	0.128	8.04
HD 987	Tuc Hor	1.818	G8	7.3	W10	3.72±0.01	M10	2.55	1.41	0.38	0.128	22.38
HD 3221	Tuc Hor	3.077	K4	122.8	M10	0.37±0.002	KE02	0.16	2.84	0.32	0.128	18.45
HD 8558	Tuc Hor	1.663	G7	13.8	M10	3.59±0.01	KE02	2.53	0.72	1.37	0.128	[90]
HD 12039	Tuc Hor	2.188	G4	13.46	W07	3.02±0.01	M10	0.34	1.35	0.6	0.128	36.64
HD 13183	Tuc Hor	1.736	G7	23	C02	2.24±0.03	M10	0.46	0.74	1.38	0.132	[90]
HD 29615	Tuc Hor	1.604	G3	17.53	M10	4.25±0.02	KE02	0.69	0.44	3.31	0.13	[90]
HD 202917	Tuc Hor	1.782	G7	14.9	W10	3.36±0.01	M10	1.39	1.17	0.85	0.128	57.89

Note. —
[a] SpT was assembled from McCarthy & White (2012).
[b] Because most $v \sin i$ values from the literature did not include uncertainties, we adopt a typical $v \sin i$ uncertainty of 10%.
[c] $v \sin i$ References: H07 = Holmberg et al. (2007), W10 = Weise et al. (2010), 3) W07 = White et al. (2007), 4) M10 = Messina et al. (2010), 5) C03 = Cutispoto et al. (2003).
[d] Values denoted with a dagger (†) indicate stars with no P_{rot} uncertainties listed in the literature. We have assigned these stars the median P_{rot} uncertainty value for the stars with a listed uncertainty.
[e] P_{rot} References: 1) M10 = Messina et al. (2010), 2) C99 = Cutispoto et al. (1999), 3) M98 = Messina (1998), 4) KE02 = Koen & Eyer (2002).
[f] L_{bol} values were calculated using bolometric magnitudes based on bolometric K corrections from Houdashelt et al. (2000); they are listed in terms of Solar luminosities ($L_\odot$).
[g] R_* values were calculated from bolometric luminosities (Houdashelt et al. 2000); they are listed in terms of Solar radii ($R_\odot$).
[h] Inclinations are shown for visual reference only. Values in brackets are those we consider edge-on, as $\sin i$ values >1 and thus unphysical.

star, as opposed to the probability distribution of an ensemble population. The assembled $\sin i_*$ values nevertheless provide first estimates of this important quantities for these young, nearby Sun-like stars.

We note that a Bayesian-type analysis (e.g. Hirano et al. 2014) could be a useful check on the most probable inclination for each system and avoid unphysical values. Moreover, this could provide realistic uncertainties in the inclinations, which are geometrically asymmetric. The presented approach of calculating uncertainties in $\sin i_*$, while more simplistic, is at least reasonable if the errors in $v \sin i$, P_{rot}, and R_* are Gaussian-like. We argue that this

is more likely to be the case for modestly rotating stars with $v \sin i$ values well above the instrumental resolution, and have P_{rot} measured over many rotation periods.

2.5 An Optimal Sample of Young Suns for Exoplanet Surveys

We have assembled the properties of 129 young Suns near Earth with spectral types between F6 and K5, inclusive. 64 are either single or effectively single, having no known companions within 5. Of these 64, 16 (25%) have known $v \sin i$ values $\leq$10 km/s, a rotational value that should allow velocity precisions better than 100 m/s (Beatty & Gaudi 2015); we do caution that the activity associated with these stars may cause stellar jitter well above this value, affecting the precision of RV measurements and inference of exoplanet properties from transits. Finally, 7 stars appear to have nearly edge-on orientations and are ideal candidates for upcoming transit surveys (e.g. NASA's Transiting Exoplanet Survey Satellite Ricker et al. 2016). However, we must note that these are simply the properties of Sun-like stars in nearby young moving groups.

– 3 –

Optical Spectroscopy of Young Stars

We obtained high dispersion optical spectra of a representative sample of 12 young Sun-like stars to empirically assess the potential to find young exoplanets. Our sample consists of young Sun-like stars identified in the field (White et al. 2007) and as members of the moving groups AB Dor and β Pic (e.g. McCarthy & White 2012). All of the stars are effectively single, having no visible companions within 5; however, some of the stars could be spectroscopic binaries.

We chose stars with $v \sin i < 20$ km/s, as higher rotational velocities result in broader lines whose bisectors are harder to detect precisely. The observed sample includes 8 stars with known $v \sin i$ that were monitored strategically for RV variation as well as 4 stars with no known $v \sin i$ that were observed solely for the purpose of determining their $v \sin i$ (dubbed Reconnaissance stars; see Table 3.1). Reconnaissance stars determined to have $v \sin i < 20$ km/s could be included in future young planet searches with the RV method. The full sample includes spectral types ranging from G6 to K5, V magnitudes that range from 7.45-10.02 mag, and $v \sin i$ values that range from 7.1 - 17.8 km/s.

3.1 Observations

The 12 young Sun-like stars were observed using two different facilities: 1) the Tillinghast Reflector Echelle Spectrograph (TRES) mounted on the 1.5-m Tillinghast Reflector at the Fred L. Whipple Observatory (FLWO) on Mt. Hopkins, AZ and 2) the Spectrograph for Observation of PHenomena in stellar Interiors and Exoplanets (SOPHIE), a fiber-fed echelle

spectrograph on the 193 cm Telescope at the Observatoire de Haute Provence in Saint-Michel-l'Observatoire, France.

3.1.1 TRES Observations

High resolution spectra of HD 17332A, HD 17332B, HD 152555, as well as the RV G dwarf standard HD 182488 were taken with TRES. TRES is a temperature-controlled, fiber-fed instrument with a resolving power of R∼44,000 and a wavelength coverage of 3850-9100 Å, spanning 51 echelle orders (Fűrész et al. 2008).

Our strategy was to observe each star on two to three consecutive nights, followed by another two to three consecutive nights $\sim$ 1 week later, barring bad weather and depending on instrument availability. Given the RV precision of TRES, this observing cadence is well suited for identifying Jupiter mass planets ($m \sin i > \sim 0.5 M_{Jup}$) in short-period orbits (P $<$ 10 d; e.g. Quinn et al. 2012).

We also obtained high cadence observations of HD 152555 on two nights to investigate very short-term (∼10 min) variability; 7 epochs were taken over the course of one hour on 14 August 2012 and 5 epochs were taken in the same timespan on 21 August 2012. No significant variation was found ($\sigma_{RV} \sim 7.8 m/s$); on subsequent nights we obtained only one observation per star per night.

Exposure times ranged from 1-10 minutes, yielding a typical SNR per resolution element of at least 75. We also obtained nightly observations of the nearby IAU RV standard star HD 182488 to help track instrument stability and correct for any RV zero point drift. Precise wavelength calibration was established by obtaining Thorium-Argon (ThAr) emission-line spectra before and after each star spectrum, through the same fiber as the science exposures.

3.1.2 SOPHIE Observations

SOPHIE is temperature- and pressure-controlled and can achieve RV precisions down to 2 m/s (Courcol et al. 2015), with a wavelength coverage of 3872-6943 Å across 41 orders. SOPHIE observations were obtained in two runs of ~ 7 half-nights each scheduled about a month apart in order to be sensitive to Jupiter mass planets ($m \sin i > \sim 0.5\ M_{Jup}$) with orbital periods of a few days, as well as slightly longer period Jupiter mass companions.

We obtained calibration images at the beginning of each night to determine the flat field and the wavelength solution, including bias frames, Tungsten and ThAr lamp exposures. We also obtained 2-3 spectra per star per night in High Resolution (HR) mode ($R \sim 75,000$ at 5500 Å); bias values for each spectrum were systematically measured from 53-pixel-wide overscan areas on either side of the frame. In order to account for possible changes in the instrument that can cause apparent RV drifts (on the order of 2-3 m/s per hour), we obtained ThAr exposures at 2-3 hour intervals throughout the night. The zero RV drift is computed at the time of the observation by interpolating between the RV zero points obtained with ThAr exposures before and after the science exposure. Two optical fibers, one for the star and one for the background sky, were used; the fiber separation is $1'.8$ and the star fiber has a diameter of 3.

We aimed for SNR $\sim$ 100 (per pixel, per observation, measured at 5500 Å) for the brightest stars (HD 377, HD 38230, HD 138004, V835 Her), SNR $\sim$ 80 for slightly fainter stars (V577 Per A, IS Eri), and SNR $\sim$ 40 for the faintest stars (BD+20 1790, HD 189285, and BD+05 4576). We note that we stopped observing BD+05 4576 after 5 epochs because its significant RV variation is consistent with that of a spectroscopic binary.

3.2 Reduction, Extraction, and Cross-Correlation

3.2.1 Analysis of TRES Spectra

TRES spectra are reduced as described in Buchhave et al. (2010). First, the bias level is removed, the raw images are cropped, and cosmic rays are removed. The spectra are then optimally extracted according to the prescription in Hewett et al. (1985). The blaze function is determined and then divided into the rectified flat field to correct for pixel-to-pixel variations. Scattered light is removed by masking the Échelle orders and fitting the light between orders with a 2-dimensional (2D) polynomial. ThAr exposures before and after each science spectrum are combined and fit with a Gaussian to obtain the center of the line profile for the wavelength calibration; a 2D 5th order Legendre polynomial is fit to the ThAr exposures for the wavelength solution.

To determine the RVs for each star, the strongest exposure was chosen as a template and cross-correlated with individual spectra, order by order. We typically used ~ 25 orders, rejecting the ones with telluric absorption, fringing in the far red, and low SNR in the far blue. For each epoch, the cross correlation functions (CCFs) from all orders were added and then fit with a Gaussian to determine the relative RV for that epoch. This allows for the higher SNR orders to be weighted more than lower SNR orders when fitting the CCF, as opposed to determining an RV for each order and then averaging those. Internal error estimates (which include, but may not be limited to, photon noise) for each observation were calculated as $\sigma_{\rm int} = {\rm RMS}(\vec{v})/\sqrt{N}$, where $\vec{v}$ is the RV of each order, N is the number of orders, and RMS is the root-mean-squared velocity difference from the mean. We determined that

the observed dispersion of the standard star RVs was consistent with the estimated internal errors, indicating that the instrument was stable over the observing period.

To evaluate the significance of any potential velocity variation, we compared the observed velocity dispersions ($\sigma_{\rm RV}$) to the combined measurement uncertainties, which we assumed stem from three sources: (1) internal error, $\sigma_{\rm int}$, (2) night-to-night instrumental error, $\sigma_{\rm TRES}$, and (3) RV jitter induced by stellar activity, σ_{jitter}. Observations of the standard star are to measure these potential variations. Final errors assigned to RVs are from internal errors.

We used observations of the slowly rotating, G8 standard star HD 182488 to correct for systematic velocity shifts between runs. First we calculated the mean RV for each run, which we then used to offset the data to a common zero point. After the run-to-run corrections, the dispersion of the standard star RVs was 7.6 m/s with internal errors of only 9.5 m/s. We note that the instrument has been remarkably stable during the span of our observations, with run-to-run offsets similar to their uncertainties. We compare RV measurements of the standard star HD 182488 to those of the AB Dor members HD 17332A, HD 17332B, and HD 152555 in Figure 3.1; RV values are relative to the mean RV, which we will refer to as "relative RVs." A summary of these observations are presented in Table 3.1.

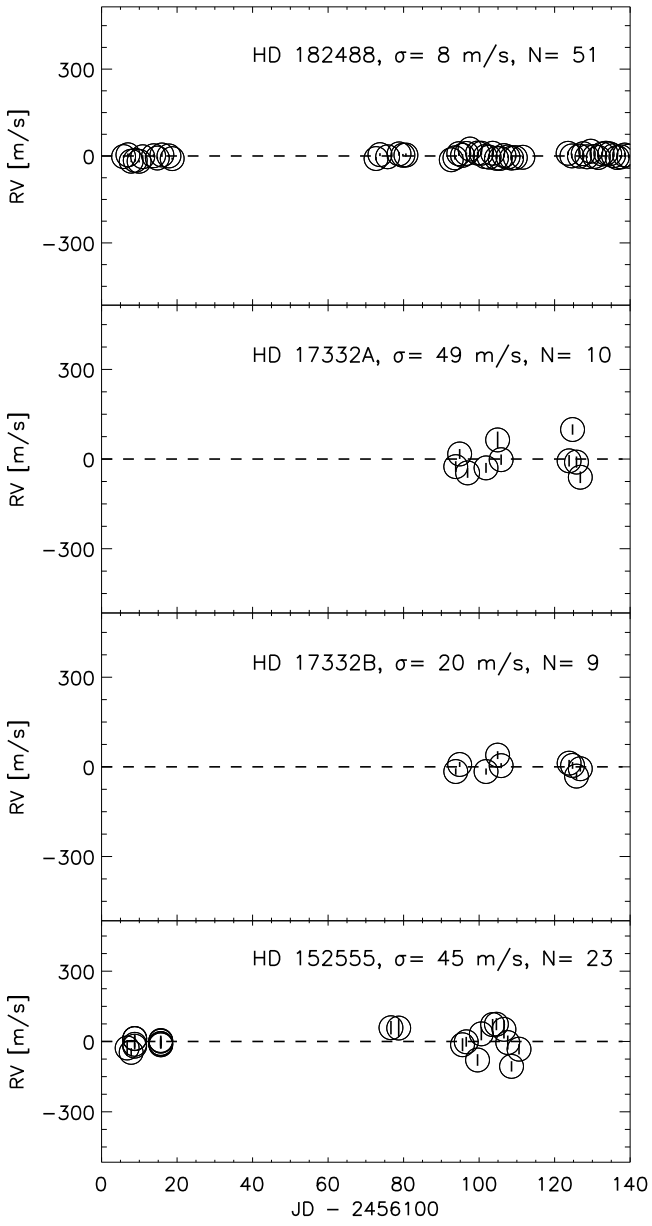

Figure 3.1 Precise radial velocities for the RV G dwarf standard HD 182488 and the young AB Dor members HD 17332A, HD 17332B, and HD 152555, observed with the TRES instrument. RV values are relative to the mean RV. The dispersions of the standard star demonstrate an observing precision of $\sim 8\ m/s$.

Table 3.1. Summary of Optical Spectroscopic Observations

Star	N	$< v \sin i >$ (km/s)	$v \sin i_{err}$[1] (km/s)	$< RV >$ (km/s)	RV_{err} (km/s)	σ_{RV} (km/s)
			TRES			
HD 17332A	10	13.3	0.5	46.309	0.0155	0.0490
HD 17332B	9	2.0	0.5	-7.920	0.0067	0.0202
HD 152555	23	18.1	0.5	11.993	0.0093	0.0447
			SOPHIE			
HD 199058[2]	1	12.53	···	-19.0204	···	···
PQ Vir[2]	1	1.82	···	21.8173	···	···
BD+28 382B	2	7.39	0.05	5.3471	0.0022	0.0030
BD+05 4576	5	2.73	0.55	-15.6023	6.9776	23.3035
V835 Her	35	8.83	0.20	-17.9714	3.6637	21.6749
BD+20 1790	32	8.50	0.20	7.8037	0.0333	0.1866
HD 377	28	14.20	0.13	1.1862	0.0090	0.0467
HD 38230	42	2.10	0.06	-28.9933	0.0012	0.0077
HD 138004	46	2.89	0.05	-14.9514	0.0093	0.0630
HD 189285	32	9.18	0.10	-18.9843	0.0095	0.0538
IS Eri	32	6.78	0.13	14.7200	0.0056	0.0317
V577 Per A	53	9.07	0.06	-5.3703	0.0098	0.0710

Note. — [1]Reported $v \sin i$ errors are the RMS of the measurements. [2]Single epoch stars, for which $v \sin i_{err}$, RV_{err}, and σ_{RV} are not reported.

3.2.2 Analysis of SOPHIE Spectra

Spectra are reduced automatically via the SOPHIE Data Reduction Software (DRS) [1] (Bouchy et al. 2009), a data reduction pipeline designed by the Geneva Observatory and modeled after the pipeline for HARPS. The blaze function and flat field are first derived for each order from Tungsten lamp exposures; the spectra are then de-blazed and divided by the flat field. Currently, no dark or scattered light corrections are performed. The DRS then finds the spectral orders, optimally extracts the spectra, rejects detected cosmic rays, applies a wavelength solution from the ThAr exposures, and applies a barycentric correction; instrumental drift is corrected using the Thorium-Argon (ThAr) lamp exposures. Data reduction for both fibers (star and sky) are performed separately.

Due to thermal variations of the spectrograph, SOPHIE spectra are affected by a seasonal change of the Line Spread Function (LSF) that creates a defect in the wavelength solution. Because stellar lines are resolved at the resolution of SOPHIE but ThAr lines are not, the small change in LSF impacts the two spectra differently. We use the seasonal correction determined by Courcol et al. (2015) from a large sequence of RV standard star observations to account for this effect.

Our data was not obtained simultaneously with ThAr calibrations because the targets are too faint and the risk of ThAr pollution of the stellar spectrum is too high; the RV is calibrated with the closest ThAr observation. We obtained ThAr calibrations roughly every 2 hours, but the spectral drift in 2 hours may be close to 5 m/s. Thus, we use a linear interpolation between ThAr taken before and after each exposure, which allows for a typical accuracy of the RV calibration to ~ 2 m/s.

[1] The SOPHIE instrument manual and the DRS software manual can be found at www.obs-hp.fr

Once the spectra have been extracted and calibrated, RVs are determined via cross-correlation with the numerical mask that most closely matches the star's spectral type (of the following available: F0, G2, K0, K5 and M4). A G2 mask was suitable for most stars (HD 138004, HD 189285, HD 377, V835 Her, V577 Per A, IS Eri), while a K5 mask was used for BD+20 1790 and HD 38230. The cross-correlation function (CCF) is calculated around the deepest peak detected and the profile is fit with a Gaussian to obtain the RV, the full-width at half-maximum (FWHM), and the contrast.

To evaluate the significance of radial velocity variations, we compared the observed velocity dispersions ($\sigma_{\rm RV}$) to the combined measurement uncertainties, which we assumed stem from three sources: (1) internal error, $\sigma_{\rm int}$, (2) night-to-night instrumental error, $\sigma_{\rm SOPHIE}$, and (3) RV jitter induced by stellar activity, σ_{jitter}. For SOPHIE, $\sigma_{\rm int}$ and $\sigma_{\rm SOPHIE}$ are not analyzed separately. Observations of the standard star were obtained without simultaneous ThAr and corrected for seasonal drift for all programs with an observing strategy similar to ours; these observations yield a typical longterm internal error of $\pm$ 3 m/s.

3.3 Radial and Rotational Velocity Measurements

3.3.1 Radial Velocity

A summary of the results for both TRES and SOPHIE observations is presented in Table 3.1. We averaged multiple epochs for each star to obtain $< RV >$, and RV uncertainties were assigned by taking the standard deviation from the mean and dividing by $\sqrt{N}$. The RV dispersion (σ_{RV}) is simply the standard deviation of the RV and encompasses internal errors and photon noise, but also physical variations such as stellar jitter. For effectively single stars, σ_{RV} ranges from 0.003 km/s to 0.187 km/s. For the most active stars, a high

σ_{RV} can be explained by stellar jitter, a detailed analysis of which is discussed in the next chapter using SOPHIE data.

The determined RV and uncertainties along with Julian date for the 3 stars monitored with TRES are presented in Appendix A, Tables A.1 to A.3. Counting multiple measures on a single night as 1 epoch, we observed a total of 16 epochs for HD 152555, 10 epochs for HD 17332A, and 9 epochs for HD 17332B. The collective observations span a temporal baseline of 6 months.

The determined RV and uncertainties along with Julian date for the 9 stars monitored with SOPHIE are presented in Appendix A, Tables A.4 to A.12. Counting multiple measures on a single night as 1 epoch, the total number of epochs for the 9 monitored stars range from $4 - 22$, spanning a temporal baseline of 2 years.

Of the 9 stars monitored with SOPHIE, two have large RV variations ($\sigma_{RV} > 20$ km/s) that indicate the presence of a stellar companion: V835 Her and BD+05 4576. Two other stars exhibit much smaller RV variation ($\sigma_{RV} < 10$ m/s); these will be used as a guide to empirically assess how well the activity markers can be measured: HD 38230 and HD 138004.

We note that while HD 138004 exhibits nontrivial RV change over the span of two observing seasons ($\sigma_{RV} = 64$ m/s), within each season RV variation is minimal ($\sigma_{RV} = 3$ m/s in season 1, $\sigma_{RV} = 7$ m/s in season 2). The RV variations HD 138004 does exhibit over a one year baseline result from the presence of a moderately distant companion, likely the companion recently imaged by Riddle et al. (2015). In contrast, the known active star BD+20 1790 (Hernán-Obispo et al. 2005) varies greatly in RV ($\sigma_{RV} = 206$ m/s, N = 33 epochs).

V835 Her, a known double-lined spectroscopic binary, has a σ_{RV} of 22 km/s (Osten & Saar 1998). BD+05 4576 was not previously known to be a spectroscopic binary, but its σ_{RV}

23 km/s is typical of binary systems; we stopped monitoring this star after we discovered its large RV amplitude in order to concentrate our efforts on possible young planet hosts. Figure 3.4 illustrates the radial velocity results for these two binaries.

SOPHIE RV results for the non-binary stars are illustrated in Figure 3.2 (for stars observed in the 2013A and 2014A semesters) and in Figure 3.3 (for stars observed in the 2012B and 2013B semesters). Their observed RV dispersions range from 8 to 206 m/s.

3.3.2 Rotational Velocity

Projected rotational velocities for TRES stars were calculated using the Stellar Parameter Classification (SPC) pipeline developed by Buchhave et al. (2012 ; see Supplemental Information). SPC was used by collaborator S. Quinn to cross-correlate a 4-dimensional grid of synthetic spectra against each observed spectrum with varying parameter values for effective temperature (T_{eff}), surface gravity (log g), metallicity, and $v \sin i$; here we report only $v \sin i$.

Projected rotational velocities for all SOPHIE stars were calculated based on the method used for the CORALIE spectrograph (Santos et al. 2002) and adapted for SOPHIE by Boisse et al. (2010). Using the calibrated relationship between $v \sin i$ and the width of the CCF (σ) in SOPHIE HR mode, for Sun-like stars:

$$v \sin i = A\sqrt{\sigma^2 - \sigma_0^2}, \tag{3.1}$$

where

$$\sigma = \frac{FWHM}{2\sqrt{2ln2}}, \tag{3.2}$$

Table 3.2. Reconnaissance Star Results

Name	BJD	RV (km/s)	RV error (km/s)	$v \sin i$ (km/s)	SNR (at 500 nm)
BD+28 382B	56218.50351	5.34926	0.010032	7.43	37.3
BD+28 382B	56252.46093	5.34495	0.010072	7.35	37.1
HD 199058	56217.26229	-19.02040	0.012357	12.53	37.4
PQ Vir	56439.39176	21.81730	0.003776	1.82	60.6

$$\sigma_{0HR} = 9.90 - 22.56(B-V) + 22.37(B-V)^2 - 6.95(B-V)^3, \tag{3.3}$$

and $A = 1.73$ in HR mode; σ_0 is the value of the CCF width we expect for a "non-rotator" of a given spectral type. In Equation 3.3, $B - V$ is used as a tracer of the effective stellar temperature, with which $v \sin i$ exhibits a dependence (Boisse et al. 2010). The full width at half-maximum (FWHM) of the CCF for each spectrum is calculated automatically by the DRS.

Average $v \sin i$ values for the monitored stars are reported in Table 3.1; these values range from 2.10 km/s to 14.2 km/s. Table 3.2 lists measured values of the individual epochs for the 3 Reconnaissance stars observed with SOPHIE. These stars were observed to obtain their $v \sin i$ values only, in order to determine their feasibility for inclusion in young planet searches with the RV method. The average $v \sin i$ values for the Reconnaissance stars were relatively low, ranging from 1.82 km/s to 12.53 km/s; thus, they could all be included in future observations for RV planet searches. We note that the two epochs of BD+28 382 are separated by 34 days and the measured RVs are consistent within 0.004 km/s.

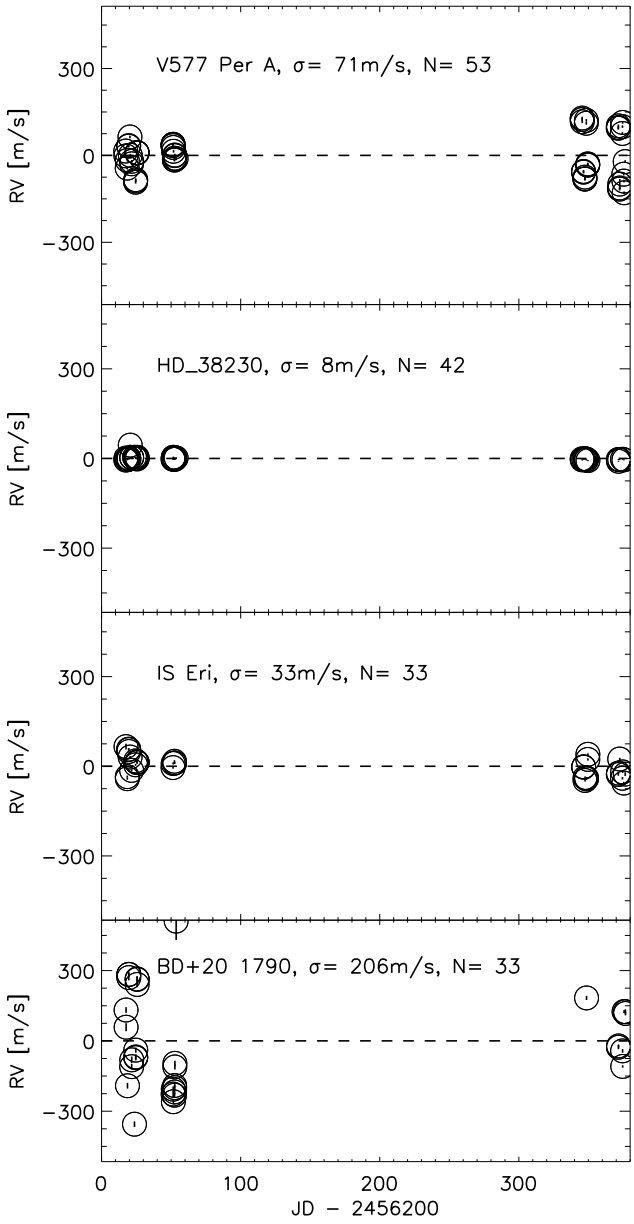

Figure 3.2 Precise relative RVs for the young AB Dor members V577 Per A, IS Eri, and BD+20 1790, and the young field star HD 38230, observed with the SOPHIE instrument.

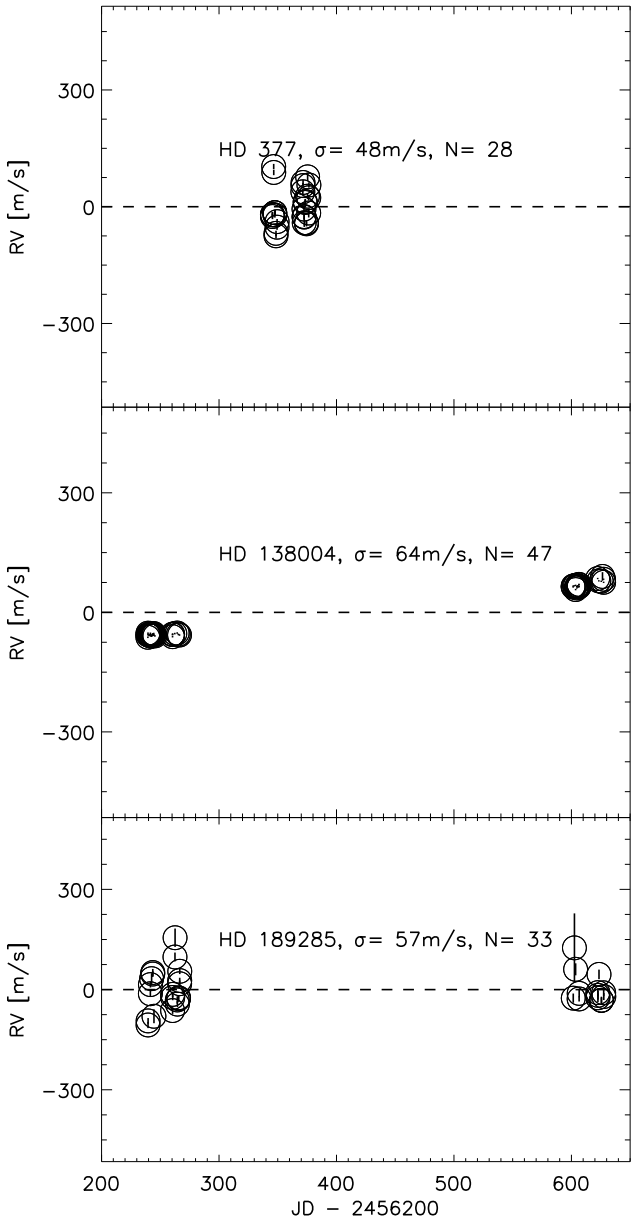

Figure 3.3 Precise relative RVs for the young field stars HD 377 and HD 138004, as well as the young AB Dor member HD 189285, observed with the SOPHIE instrument.

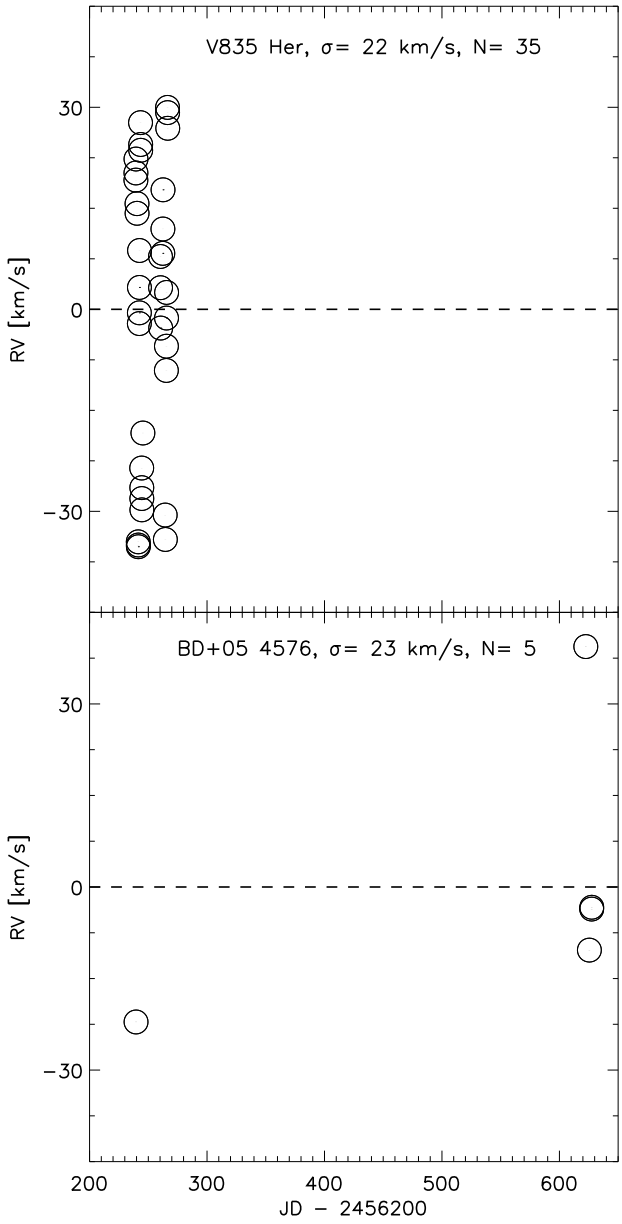

Figure 3.4 Precise relative RVs for the spectroscopic binary V835 Her and newly discovered BD+05 4576, observed with the SOPHIE instrument.

– 4 –

Activity Analysis of SOPHIE Stars

4.1 How Stellar Activity Manifests Itself

Stellar activity associated with young, active stars inhibits planet detection in several ways. These stars' rapid rotation produces broader spectral lines than older and more slowly rotating field stars, which limits the RV precision that can be obtained by introducing uncertainty in measures of the line center (e.g. Weise et al. 2010). Furthermore, cool spots and occasional flares on the surface of young stars introduce stellar jitter, which makes measuring precise RVs difficult (e.g. Saar & Donahue 1997; Reiners 2009).

The stellar jitter introduced by cool spots stems from their deformation of the stellar absorption lines as the star rotates. Figure 4.1 shows that when a spot rotates into and then out of our view, the line center will be slightly red-shifted and then blue-shifted. This is because of diminished flux from the side of the star that is approaching and then receding from us, and can convincingly mimic RV modulation induced by a companion (e.g. Queloz et al. 2001; Desort et al. 2007).

These line deformations nevertheless provide a way to distinguish between RV variations caused by a companion from those caused by spots, particularly if the $v \sin i$ is significant (> 5 km/s) (e.g. Saar & Donahue 1997; Desort et al. 2007). Two potentially useful techniques to identify line deformations are the bisector span and the full width at half maximum (FWHM) of the absorption lines. Variations of the bisector span that are anti-correlated with RV variations are known to be an excellent indicator of spot induced RV variations (e.g. Queloz et al. 2001; Hatzes 2002). It has been suggested, based on artificial spotted star models, that variations of the FWHM with respect to RV can also serve as an indicator of

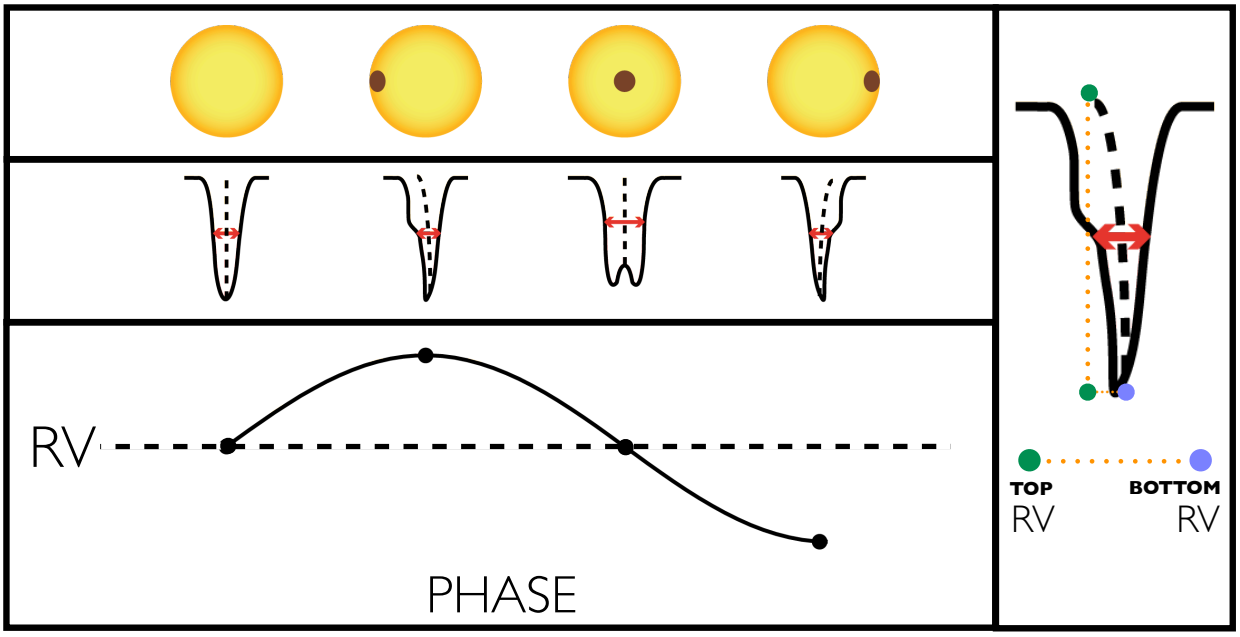

Figure 4.1 *Top Left Panel*: The location of a cool spot at different rotational phases of the star. *Middle Left Panel*: An illustration of how the spot distorts the shape of absorption lines at each rotation phase, artificially shifting the line center and distorting the bisector span and FWHM (red arrows). *Bottom Left Panel*: The line center, measured at different phases, produces a false RV modulation that can mimic the signature of a planet. *Right Panel*: The bisector span is determined by measuring the RV at the bottom of the line center and subtracting it from the RV measured at the top of the line center, near the continuum. This illustration has been exaggerated to clearly show the bisector span, which in reality is not perceptible by eye.

stellar activity (Boisse et al. 2011). We investigate these two activity diagnostics in Section 4.2.

A third technique to identify star spot induced modulations relies on the temperature difference between star spots and the photosphere, which in effect causes greater line deformations at shorter wavelengths than longer wavelengths. It has been demonstrated that RV jitter caused by star spots is significantly reduced in the near-infrared (NIR), where the contrast between the photosphere and cool spots is lower (e.g. Mahmud et al. 2011; Bailey et al. 2012). Figure 4.2 illustrates the reduced flux contrast at NIR wavelengths versus op-

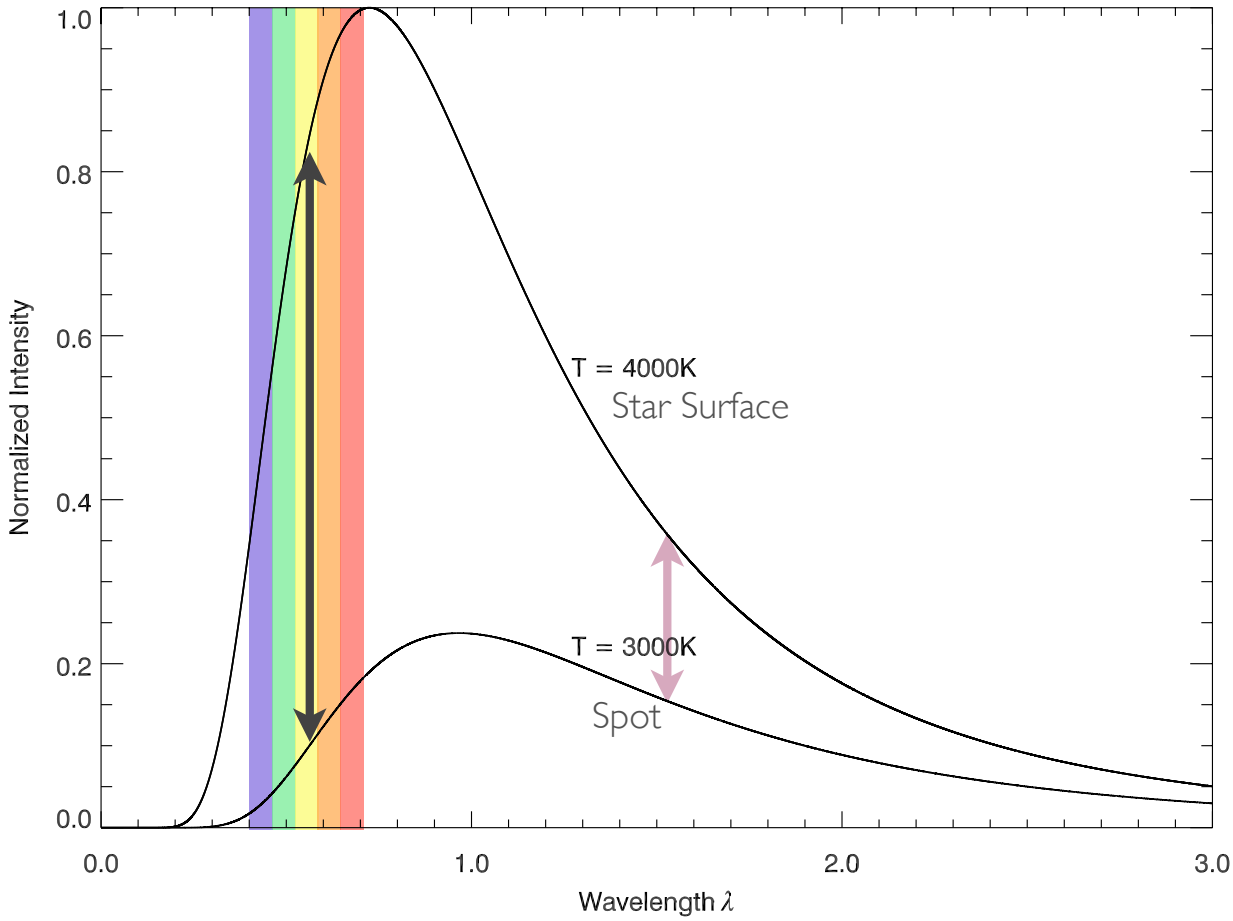

Figure 4.2 Blackbody curve for a star ($T = 4000K$) and a spot on its surface ($T = 3000K$). The colorful vertical lines represent the optical wavelength range. The black arrow highlights the large contrast between the stellar surface and the spot in the optical, while the pink arrow shows the reduced contrast between the stellar surface and the spot in the near-infrared.

tical wavelengths for a 4000 K blackbody (representing the star) and a 3000 K blackbody (representing the spot); we note that a 1000 K temperature difference between surface spots and the stellar photosphere is well established for K dwarfs (Berdyugina 2005).

We note that because of the more steeply declining light distribution across the optical region of the stellar blackbody relative to the spot blackbody, there is also a reduced flux contrast from blue to red wavelengths, which may yield reduced star spot jitter at red

wavelengths relative to blue wavelengths. We investigate this in Section 4.3 by comparing RVs determined from blue orders of SOPHIE optical spectra to RVs determined from red orders.

4.2 Markers of Stellar Activity

Of the 9 stars monitored with SOPHIE, two have RV variations indicative of stellar companions ($\sigma_{RV} > 10$ km/s) and will not be considered in the activity analysis: V835 Her and BD+05 4576. Two other stars exhibit little RV variation ($< 10\ m/s$) and will be used as guides to empirically assess how well the activity markers can be measured: HD 38230 and HD 138004. We refer to these stars as "constant RV stars." We note that while HD 138004 exhibits a clear difference in its RV over the span of two observing seasons ($\Delta RV_{mean} = 125$ m/s, $\Delta t = 388$ d), within each season RV variation is minimal ($\sigma_{RV} = 3$ m/s in season 1, $\sigma_{RV} = 7$ m/s in season 2). We interpret this difference in RV as a long-term RV modulation caused by a more distant companion, and quite likely the companion recently imaged by Riddle et al. (2015) at a separation of 0.408. The remaining stars exhibit significant RV variations (σ_{RV} of 33 - 206 m/s): BD+20 1790, HD 189285, V577 Per A, IS Eri, and HD 377. Due to bisector span calculation issues, we will not be including HD 377 in this study. We refer to the other 4 stars as "RV variables" and we explore their stellar activity in this section.

4.2.1 Bisector Span Measurements

A study by Desort et al. (2007) simulated stellar surface spots to determine their effects on observable parameters used in RV planet surveys. They found that the correlation of the bisector span with RV is a good indicator of stellar activity, but only for stars with $v \sin i$

values that are larger than the resolution of the spectrograph. As this is the case for the stars our sample, we can use the relation between the bisector span and RV values as a proxy for stellar activity.

As illustrated in Figure 4.1, the bisector span can be determined by measuring the centroid velocity at the bottom of an absorption line (at the line center) and subtracting it from the velocity measured at the top of the line, near the continuum (Queloz et al. 2001). RV variation is likely to be caused by stellar activity if the bisector span variation is correlated with the RV variation. In practice, however, measuring the velocity at the top and bottom of individual spectral lines is not practical due to the sheer volume of lines present in the SOPHIE spectra. Instead, the CCF represents an inverted average spectral absorption line and therefore provides a high SNR measurement of the stellar line shape. Bisector span values for SOPHIE data were measured at every epoch of each star from the cross-correlation of the stellar spectrum with its corresponding spectral mask (described in Section 3.2.2).

Since we do not expect stars with a constant RV to exhibit variations in their bisector spans, we can use the bisector span dispersion (σ_{BS}) of the constant RV stars as an empirical measure of the bisector span measurement precision. Both HD 38230 and HD 138004 show relatively small bisector span variations, with σ_{BS} of 3 m/s and 6 m/s, respectively. In contrast, the 4 RV variable stars all exhibit bisector span variations many times larger than the expected measurement precision. These 4 stars have dispersions σ_{BS} range from 41 to 213 m/s with a median of 59 m/s. Variations of the bisector span over time are illustrated in Figure 4.3 for the RV variable stars and Figure 4.4 for the 2 constant RV stars; bisector span values are relative to the mean, which we will refer to as the "relative bisector span."

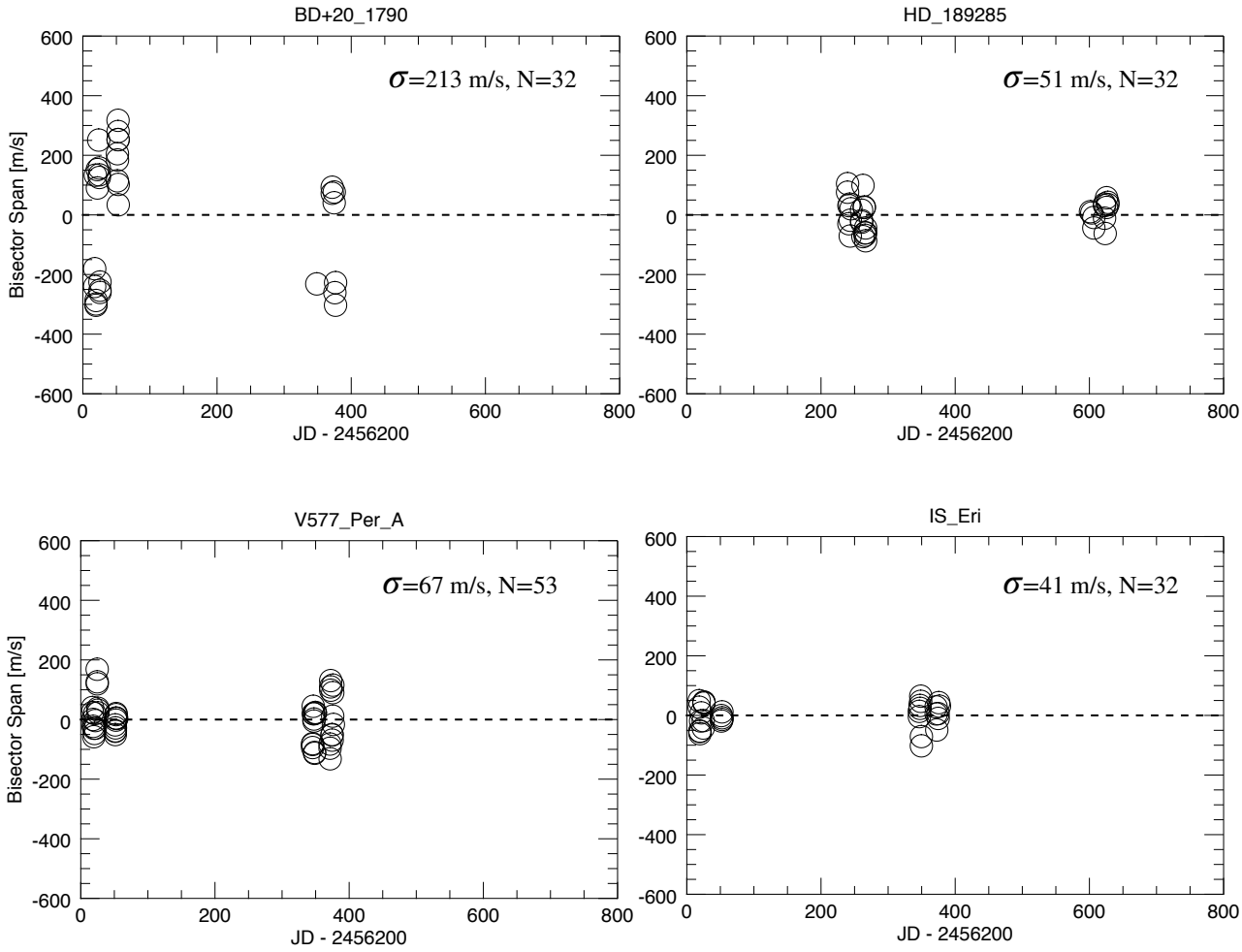

Figure 4.3 Relative bisector span variations for the RV variables BD+20 1790, HD 189285, V577 Per A, and IS Eri.

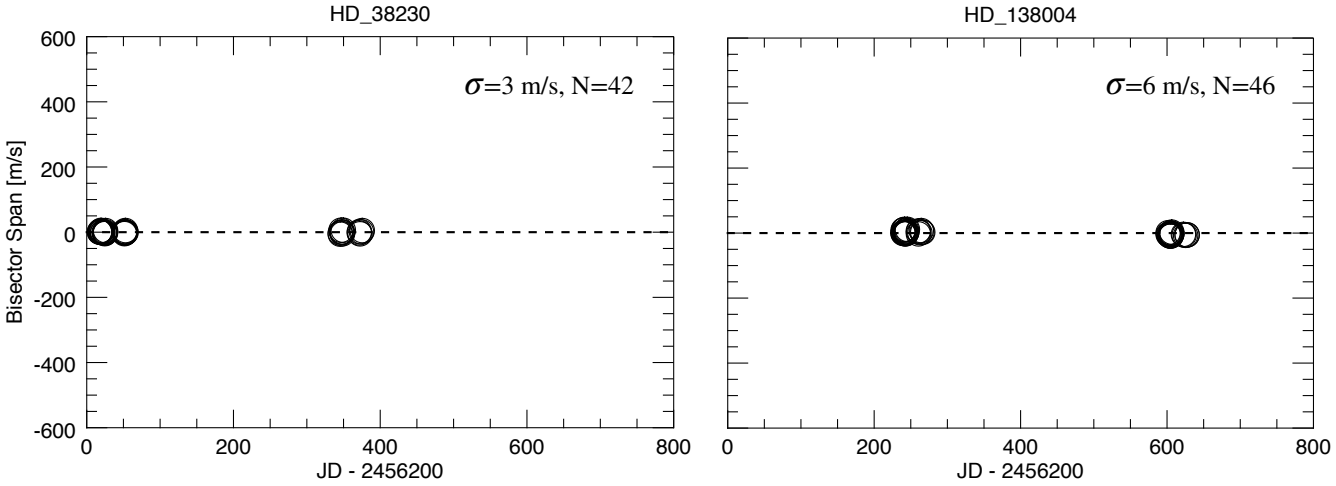

Figure 4.4 Relative bisector span variations for the constant RV stars HD 38230 and HD 138004.

As noted previously, if bisector span variations are due to activity, then variations in the bisector span and RV measurements should be anti-correlated. In other words, increases in RV caused by line deformations should decrease the bisector span because of the way it is defined (RV_{top} - RV_{bottom}; see Figure 4.1). We therefore search for a correlation between these using the Pearson coefficient (r), defined as the covariance of two variables divided by the product of their standard deviations. An r value of 1 means the two variables are totally correlated, $r = -1$ means the variables are totally anti-correlated, and $r = 0$ means no correlation.

Figure 4.5 shows the measured bisector spans versus relative RVs for the 4 RV variable stars; measured Pearson correlation coefficients are listed in Table 4.1. The bisector spans of the 4 RV variables are clearly anti-correlated with their respective RVs, with Pearson correlation coefficients r_{BS} ranging from -0.933 to -0.450 with a median of -0.791.

Table 4.1. Summary of Activity Analysis

Star	$v \sin i$ (km/s)	P_{phot} (d)	P_{phot} Ref.	P_{RV} (d)	r_{BS}	r_{FWHM}
BD+20 1790	8.50	2.79	Hernàn-Obispo et al. 2010	2.7	-0.933	-0.007
HD 189285	9.18	4.85	Messina et al. 2010	4.8	-0.450	0.325
V577 Per A	9.07	3.2	···	···	-0.879	-0.003
IS Eri	6.78	5.46	Messina et al. 2010	5.5	-0.702	-0.410

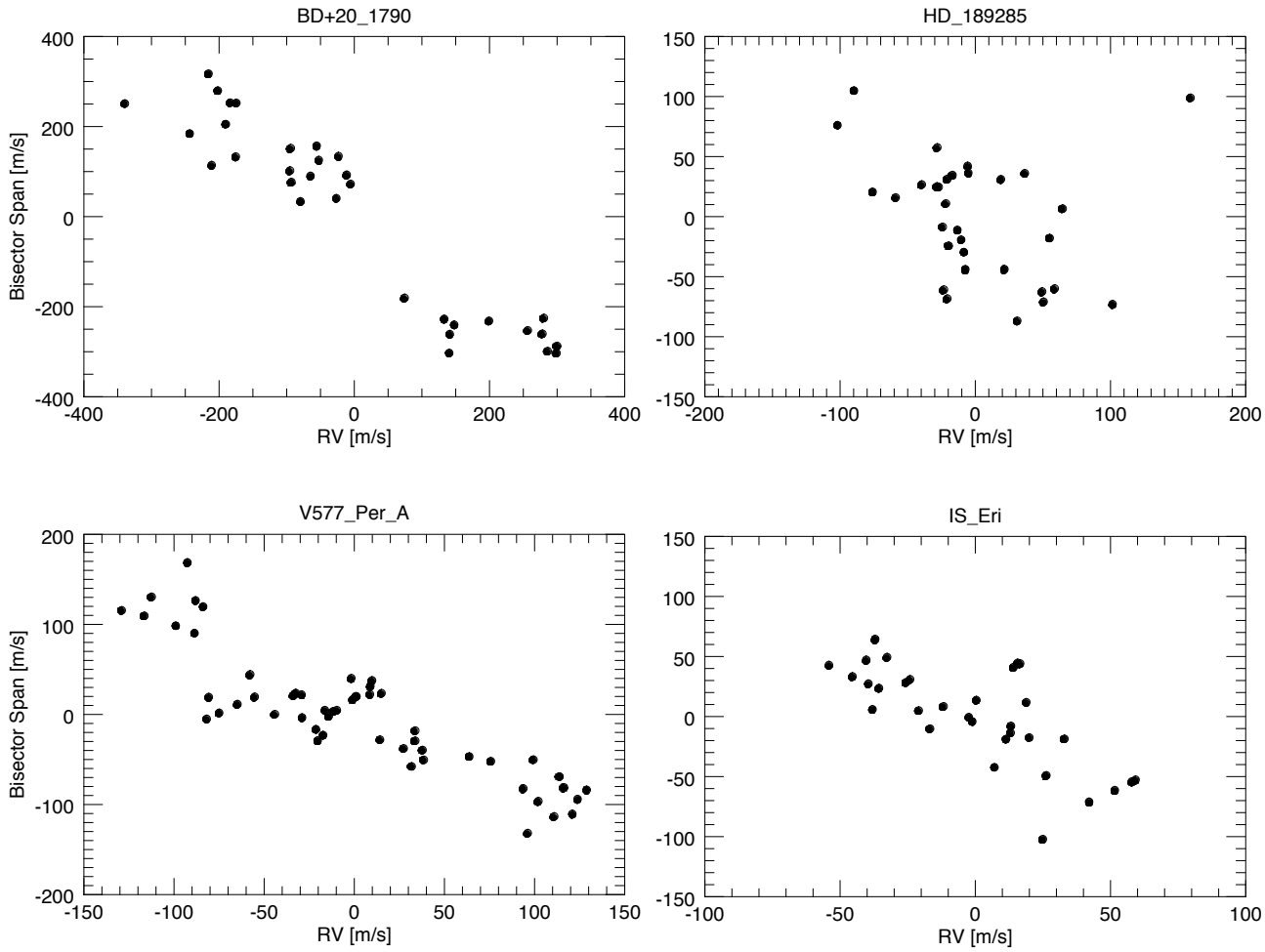

Figure 4.5 Relative bisector span versus relative RV for the 4 RV variable stars.

4.2.2 Full Width at Half-Maximum Measurements

The FWHM is determined by measuring the width of the CCF at one-half of its intensity. Figure 4.1 shows that when a spot is in front of the star, it removes light only from the center of the line and the FWHM is at its widest. However, the spot removes light from the *wings* of the line when it is on the left or right side of the star, making the FWHM narrower. In the simple case of a single spot, its presence near the limb of a star should cause the largest change in RV and decrease the FWHM the most. FWHM values for SOPHIE data were

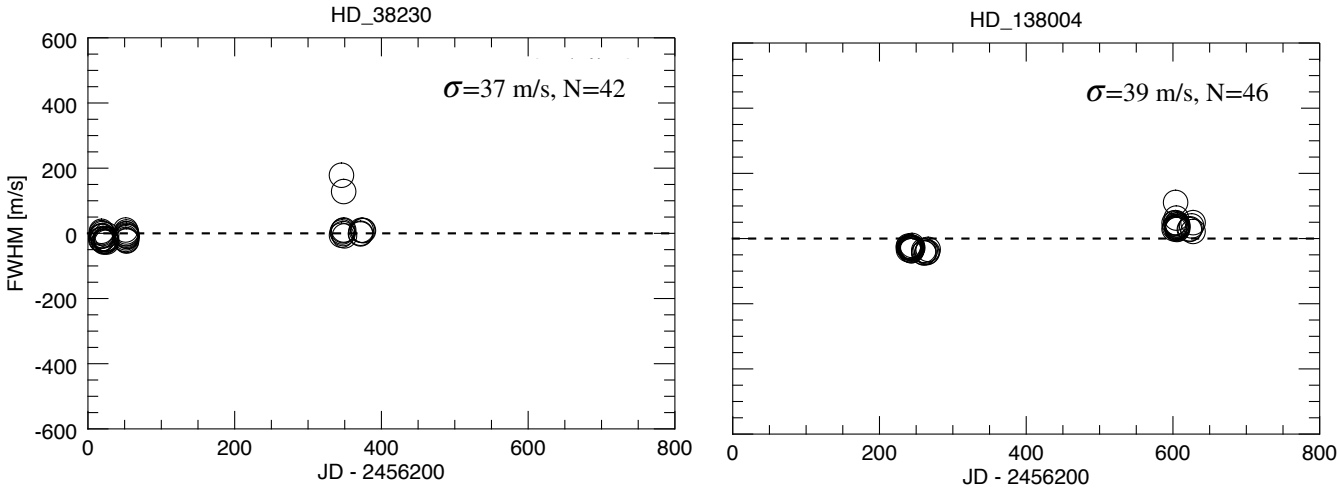

Figure 4.6 Relative FWHM variations versus time for the RV constant stars.

measured at every epoch for the 4 RV variable stars and 2 RV constant stars from the CCF of the stellar spectrum with its corresponding spectral mask.

Again, we use the RV constant stars HD 38230 and HD 138004 to determine how well FWHM values can be measured. Figure 4.6 illustrates variations of the FWHM values over time for the RV constant stars; FWHM values are relative to the mean, which we will refer to as the "relative FWHM." These RV constant stars have σ_{FWHM} values of 37 m/s and 39 m/s, respectively. In contrast, the relative FWHM dispersions σ_{FWHM} of the RV variable stars range from 77 m/s to 240 m/s with a median of 144 m/s. Figure 4.7 illustrates variations of the relative FWHM values over time for the RV variable stars.

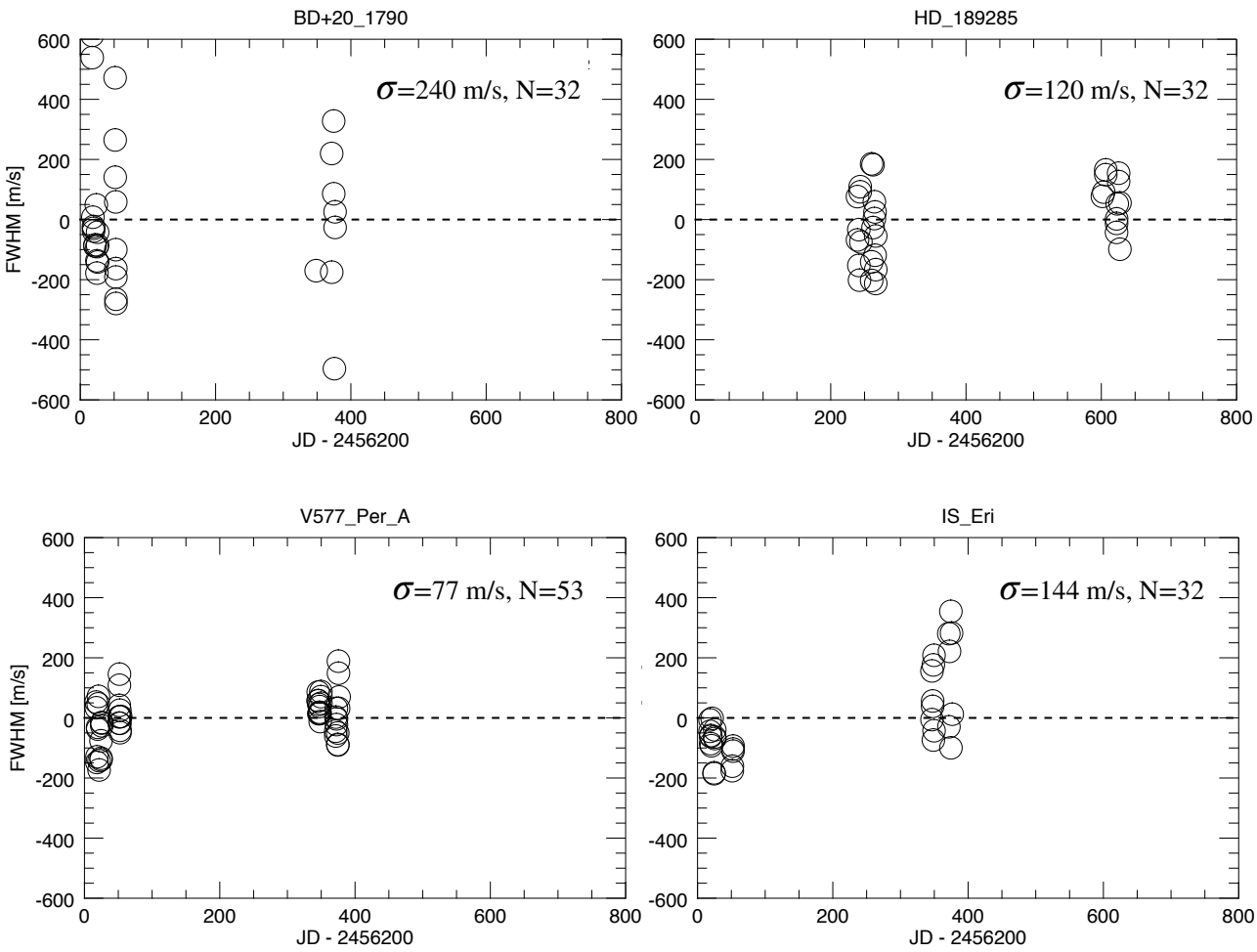

Figure 4.7 Relative FWHM variations versus time for the RV variable stars.

Boisse et al. (2011) model the effects of spots on various parameters of the CCF, including FWHM. Their study shows that there is a relationship between FWHM and RV, but it is different from the the bisector span/RV relationship. In active stars, FWHM and RV are correlated, but shifted in phase. This means that a well sampled star with many RV epochs over many rotation periods will "fill" the FWHM/RV space randomly, and therefore comparing the two would not clarify the role of activity in the data.

In Figure 4.8 we can see that a dependence of FWHM on RV is not obvious for the 4 RV variables. The RV variable stars do not exhibit a correlation between relative FWHM

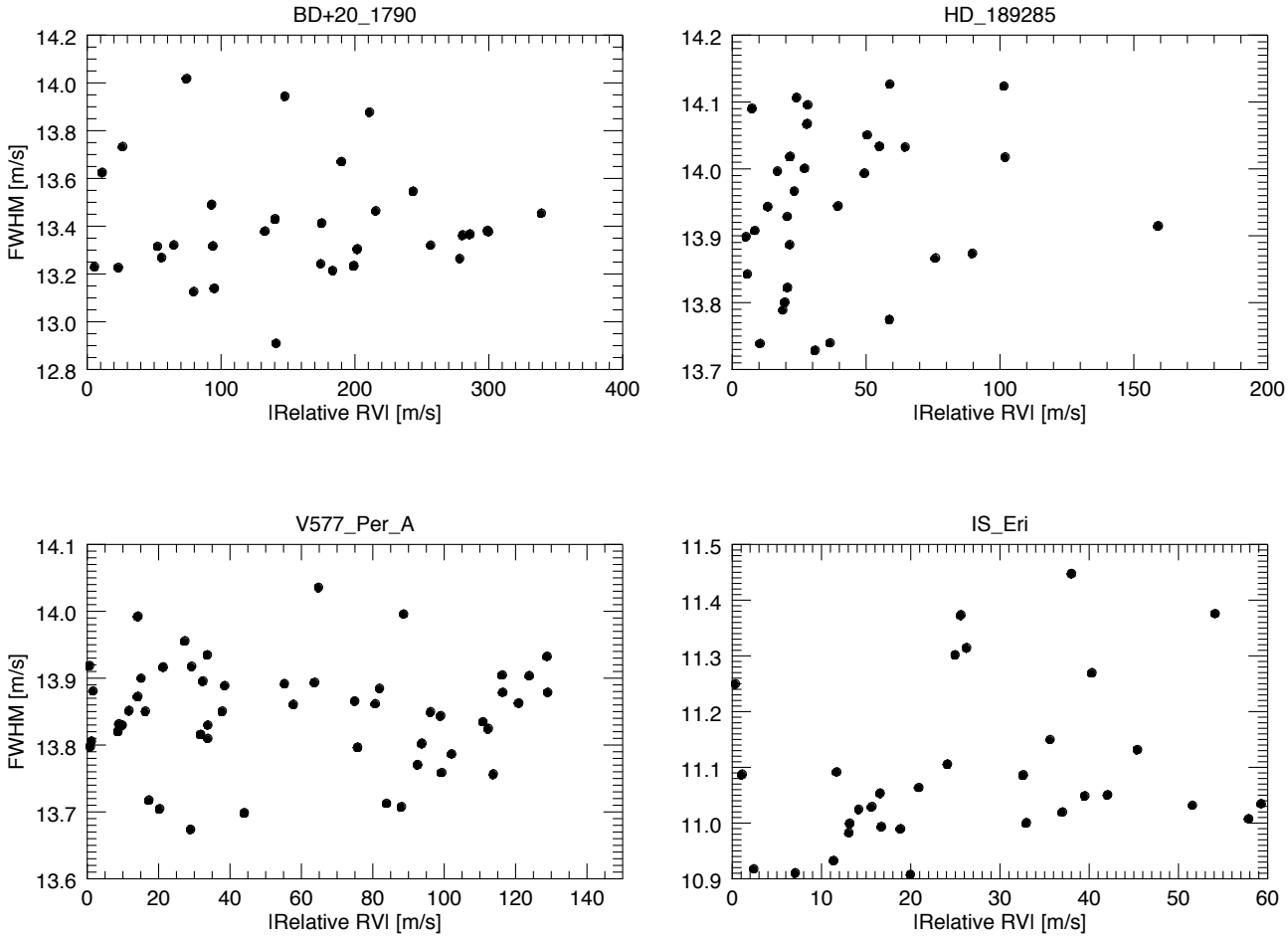

Figure 4.8 FWHM versus the absolute value of relative RV (|Relative RV|) for the 4 RV variable stars.

and relative RV. The calculated Pearson correlation coefficient r_{FWHM} for the 4 RV variable stars are listed in Table 4.1; they range from -0.410 to 0.325 with a median of -0.007.

Perhaps a better assessment of the sensitivity of the FWHM to stellar activity is to compare how it changes with the rotational phase of the star. In Figure 4.9 we compare the FWHM for the 4 RV variables to their respective rotational phase using the rotation periods we determined for each star; this analysis is described in Section 4.2.3. Even so, the FWHM does not seem to correlate with phase, with the possible exception of BD+20 1790.

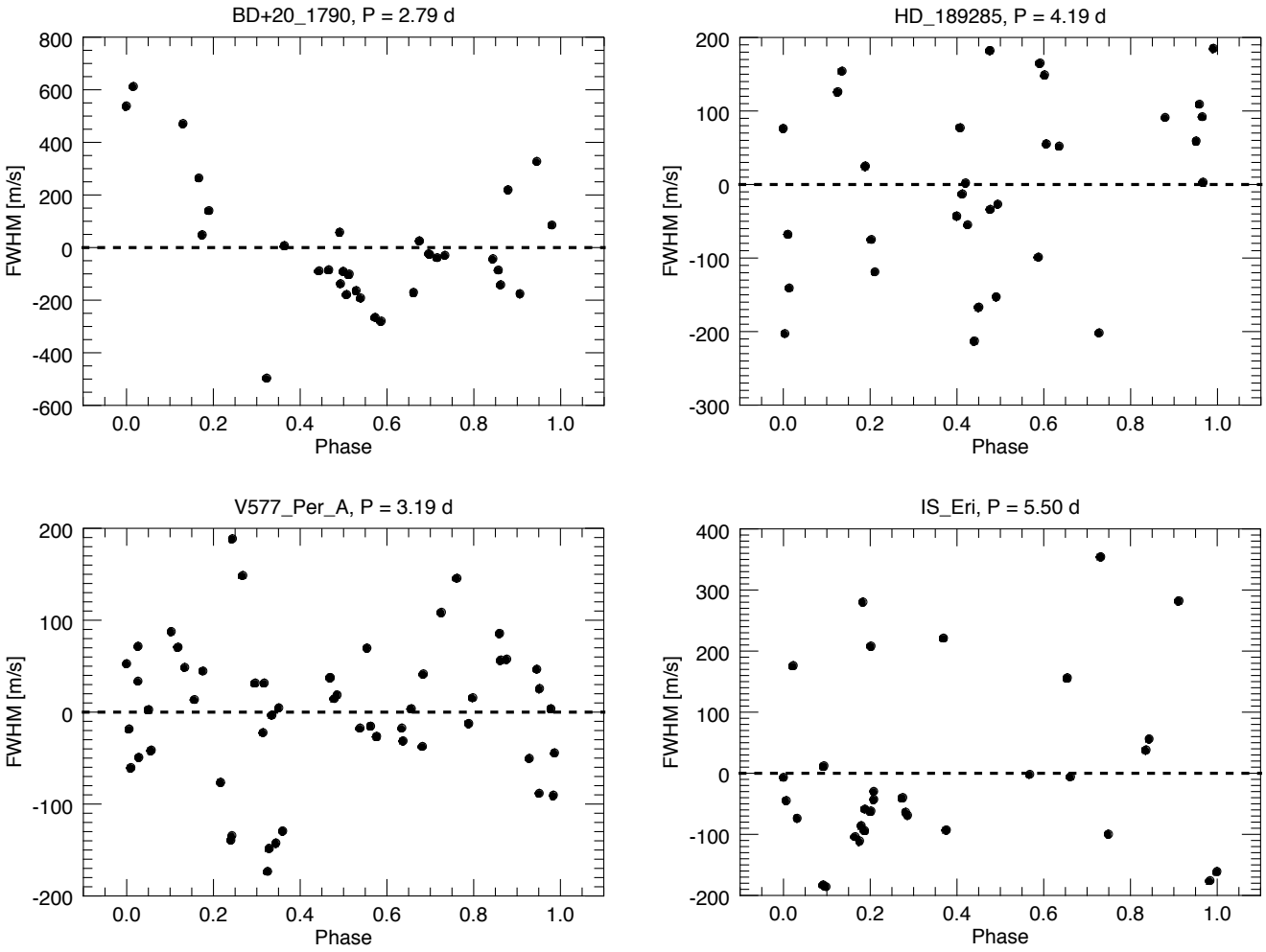

Figure 4.9 Relative FWHM versus stellar rotation phase for the 4 RV variable stars.

In Section 4.2.3 we describe the difficulty of determining stellar rotation periods from RV data due to the evolution of the spot topology over time.

4.2.3 Stellar Rotation and Periodicity in RV

One way to pinpoint activity as the cause of stellar RV modulation is to determine if the RV periodicity corresponds to the stellar rotation period. We expect that the period of RV variations for the 4 active stars will be the same as the stellar rotation period (P_{rot}, listed in Table 4.1), since the surface spots causing the variations will come in and out of view as the

star rotates. We conducted a periodogram analysis of the 4 RV variable stars to calculate the rotation period for each using YORBIT, a software package that combines standard non-linear minimizations and genetic algorithms (Segransan et al., in prep; Bonfils et al. 2013). Here we present the results of our analysis, and we compare our determined P_{rot} as well as $v \sin i$ to values from the literature. We consider a P_{rot} determined if it has a false alarm probability (FAP) less than 0.1%

4.2.3.1 HD 189285

HD 189285 is a G5 AB Dor member with a $v \sin i$ of 8.3 km/s (Desidera et al. 2015) and a 4.85 day rotation period (Messina et al. 2010). Our results are consistent with the literature: we report a $v \sin i$ of 9.18 km/s and a P_{rot} of 4.81 d (FAP $< 0.1\%$); our periodogram analysis is displayed in Figure 4.10 and the RV fit is displayed in Figure 4.11. We note that the rotation period is consistent over two observing seasons but the RV amplitudes differ by 45 m/s (see Figure 4.12). This could indicate a change in spot configuration on the stellar surface between the two observing runs, separated by ~ 1 year.

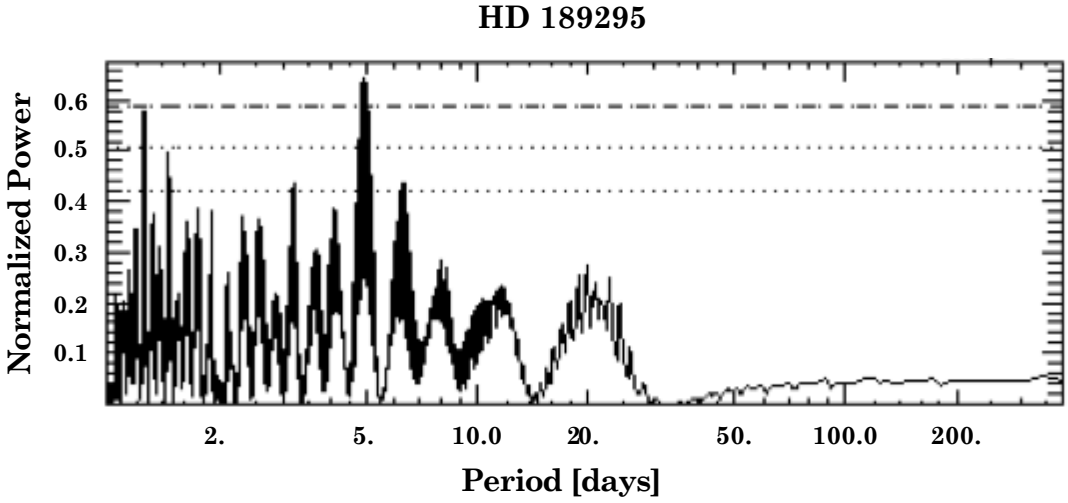

Figure 4.10 Periodogram for the G5 AB Dor member HD 189285. The strongest peak at 4.81 d has a FAP of 0.1%.

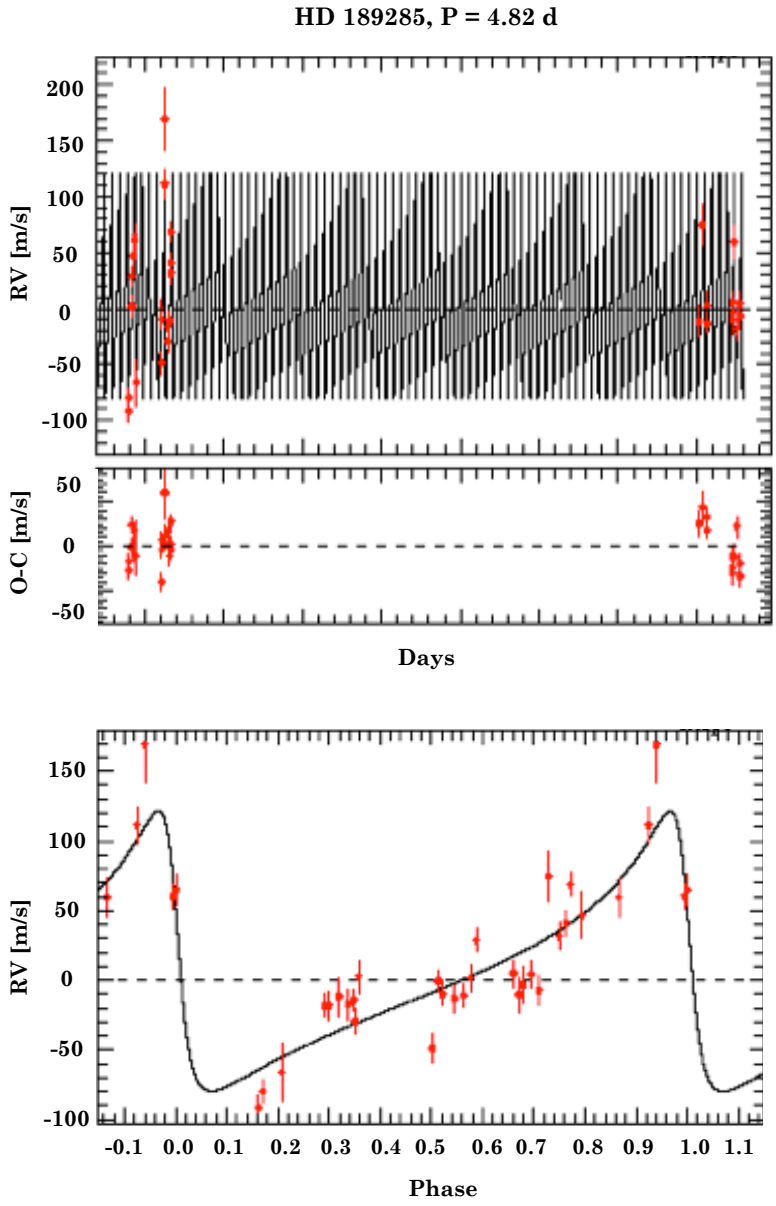

Figure 4.11 Keplerian RV fit for G2 field star HD 189285. The bottom panel shows relative RVs phased with $P_{rot} = 4.19$ d.

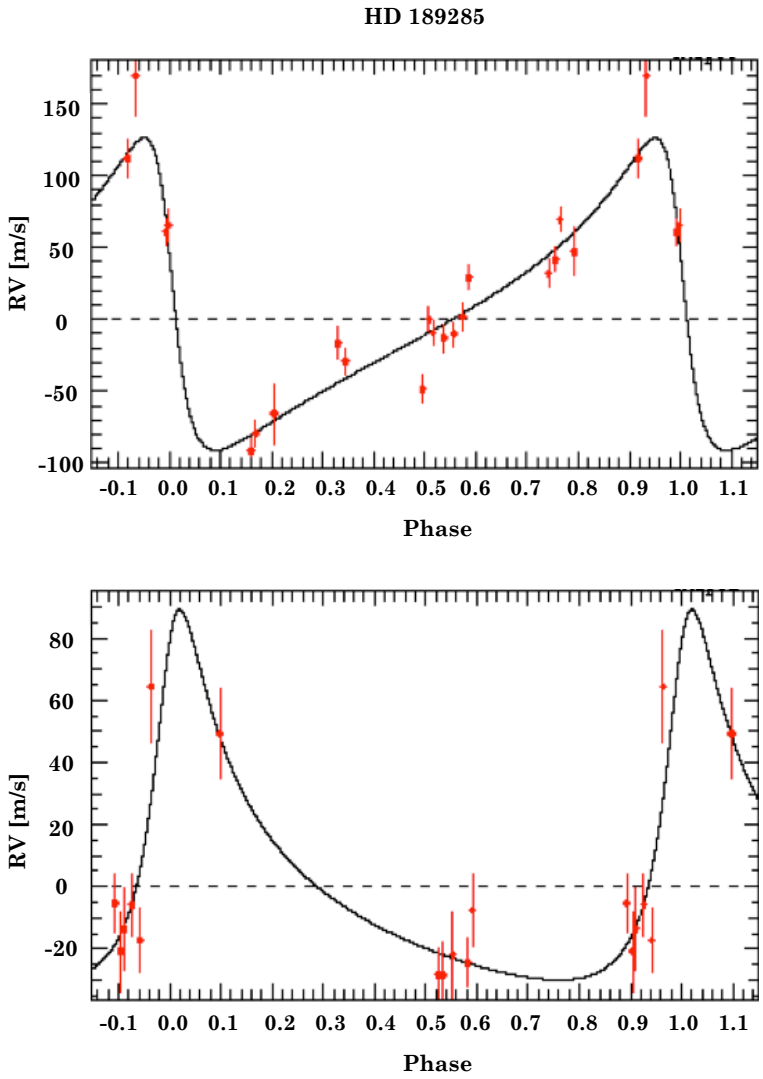

Figure 4.12 RV fit for G2 field star HD 189285 at two observing seasons ($\Delta t = 388$ d). While both seasons have a P_{rot} of 4.19 d, the RV amplitude is $\sim$ 100 m/s in the first season (top panel) and $\sim$ 65 in the second season (bottom panel), which may indicate an evolution in spot topology.

4.2.3.2 IS Eri

IS Eri is a G8 AB Dor member with a $v \sin i$ of 6.29 km/s (Desidera et al. 2015) and a P_{rot} of 5.46 d (Messina et al. 2010). Although our periodogram for IS Eri shows strong peaks with FAP $< 0.1\%$ at ~ 4.5 d and ~ 5.7 d (Figure 4.13), the first independent fit of our data using YORBIT yielded a P_{rot} solution with several outlying data points (see Figure 4.14).

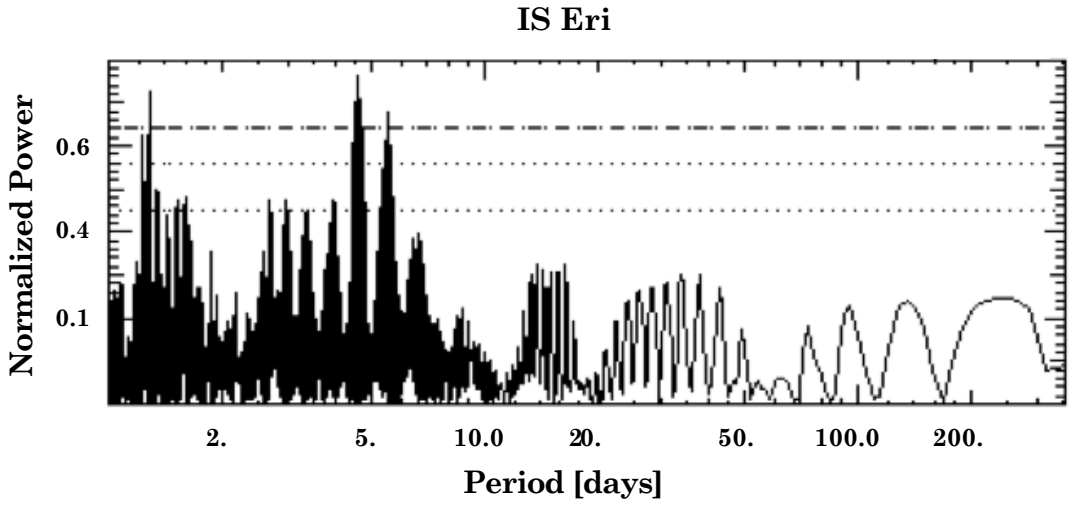

Figure 4.13 Periodogram for the G8 AB Dor member IS Eri. The strongest peak at ~ 4.5 d has a FAP of 0.1%.

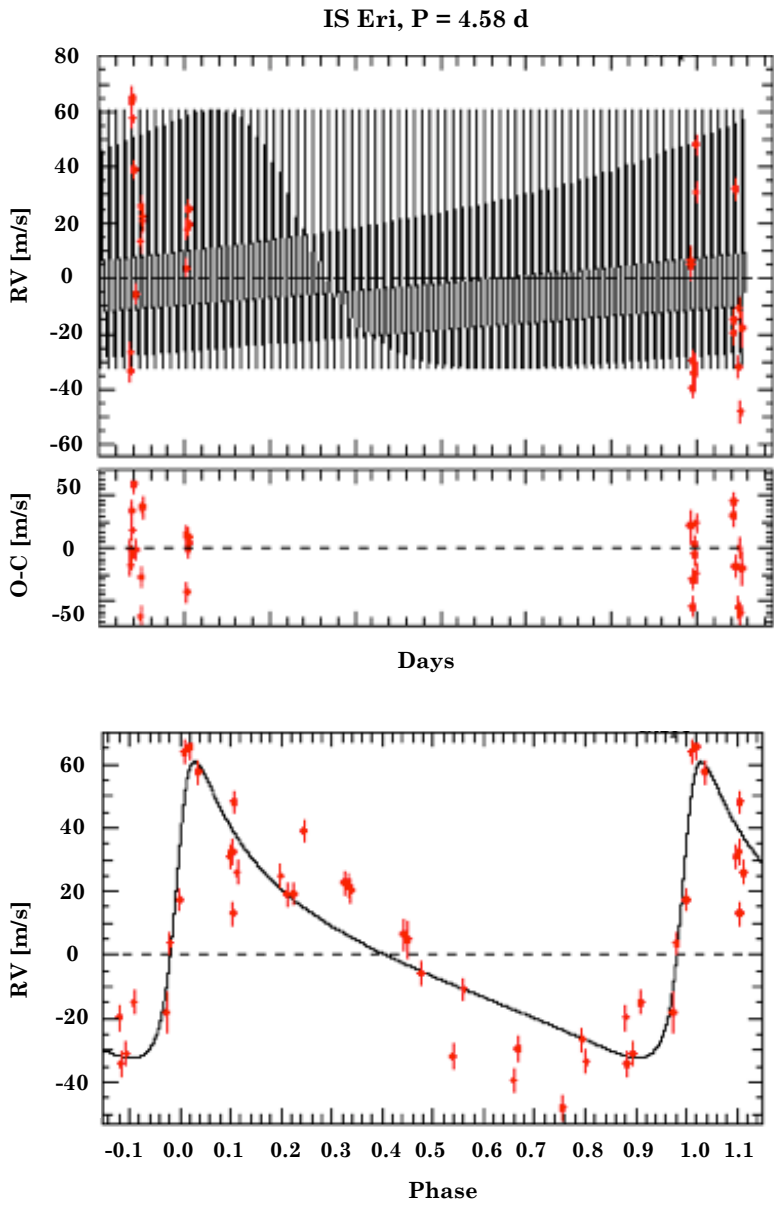

Figure 4.14 Keplerian RV fit for G8 AB Dor member IS Eri. The bottom panel shows the relative RVs phased with $P_{rot} = 4.58$ d.

In case a change in spot configuration was causing the discrepancy, we fit each season separately. The large difference in measured rotation period (~ 3.3 d in the first season vs. ~ 4.5 d in the second season) could possibly stem from differential rotation on the stellar

surface, with spots located at different latitudes. For example, the Sun rotates once every 25 days at the equator but almost 38 days at its poles, which would cause differences in the measured rotation period if observed from afar. However, since the latter rotation period is similar to that seen by Messina et al. (2010), we fit the data separately by season again but limited the possible P_{rot} solutions to a small window around their reported P_{rot}. This resulted in a fit of 5.5 d for each season of data, which is supported by the periodogram peak for the full data set (FAP $< 0.1\%$). We note that the RV amplitude in the second season is higher than that of the first ($\sim$ 100 m/s versus $\sim$ 140), which may indicate a varying spot coverage between the two seasons (see Figure 4.15).

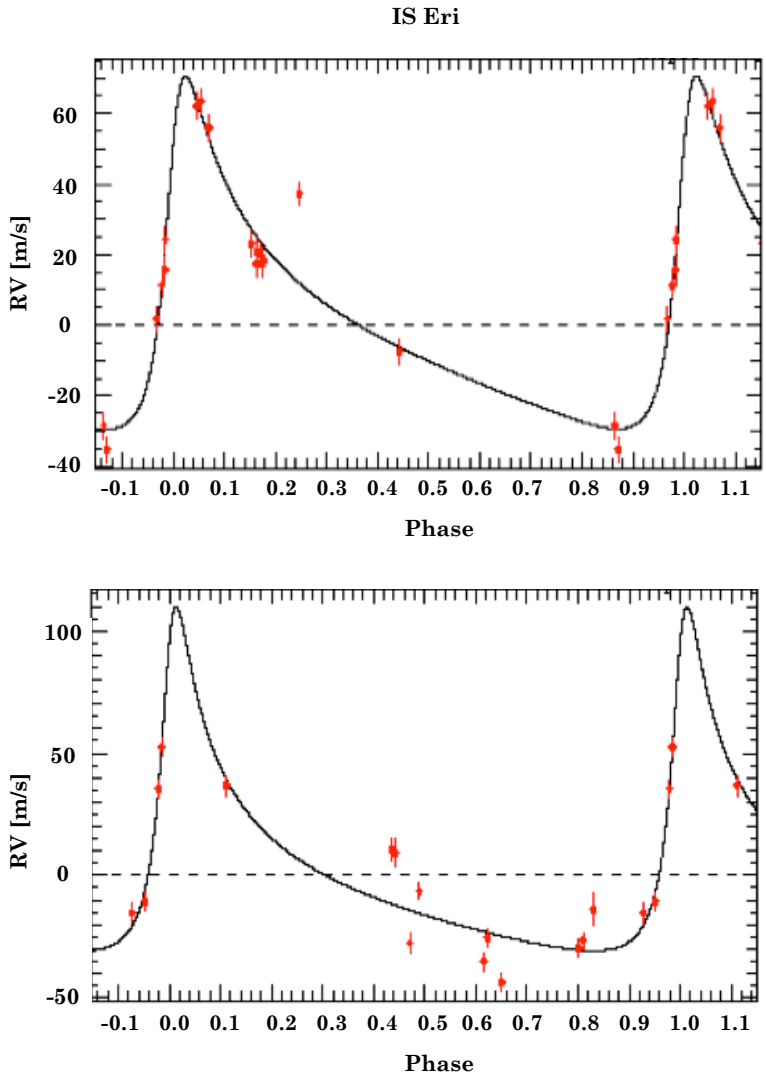

Figure 4.15 RV fit for G8 AB Dor member IS Eri at two observing seasons (Δt = 358 d). While both seasons have a P_{rot} of 5.55 d, the RV amplitude is $\sim$ 100 m/s in the first season (top panel) and $\sim$ 140 m/s in the second season (bottom panel), which may indicate an evolution in spot topology.

4.2.3.3 BD+20 1790

BD+20 1790 is a K5 AB Dor member (Reid et al. 2004) with a photometric rotation period of 2.8 d (Hernán-Obispo et al. 2010); López-Santiago et al. (2010) report a $v \sin i$ of 10.03 km/s. The discovery of a planet with a 7.78 d orbital period (P_{orb}) was reported by Hernán-Obispo et al. (2010) but later contested by Figueira et al. (2010), who suggested the RV modulation was due to stellar activity. Recently Hernán-Obispo et al. (2015) presented new data and a thorough Bayesian analysis that further supports the presence of a planet at a P_{orb} of 7.78 d.

Our periodogram analysis of BD+20 1790 (Figure 4.16) yielded two significant peaks with FAP $< 0.1\%$ at 2.78 d and ~ 7 d, but also many other secondary peaks. The initial Keplerian RV fit converged on $P_{rot} = 5.6$ d; however, the structure seemed too complex to be explained by a single Keplerian. Adopting a 2-Keplerian fit yielded $P_1 = 2.78$ d and $P_2 = 14.26$ d, but we did not have enough epochs to definitively conclude that the latter is the orbital period of a planetary companion (Figure 4.17).

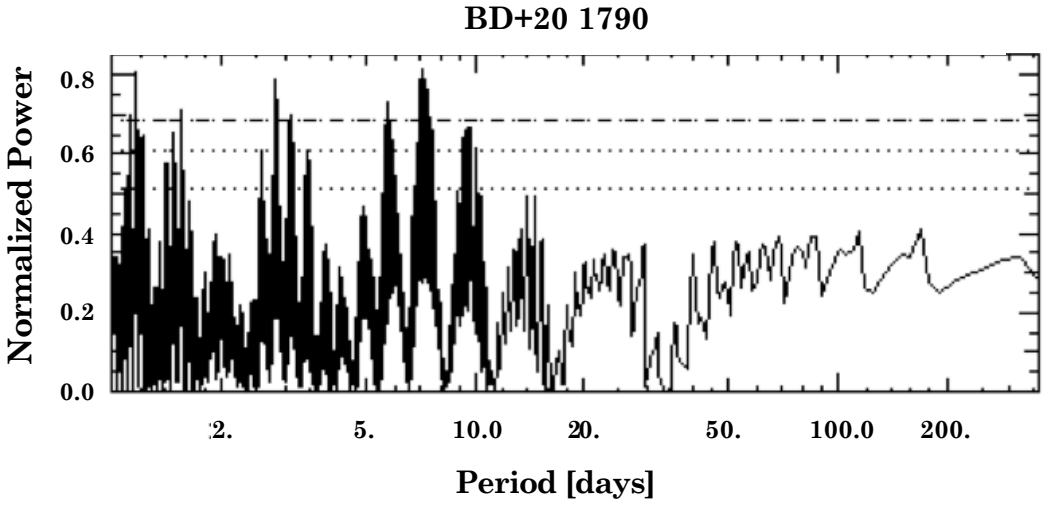

Figure 4.16 Periodogram for the K5 AB Dor member BD+20 1790. The strongest peaks at ~ 2.7 d and ~ 7 d have a FAP of $< 0.1\%$.

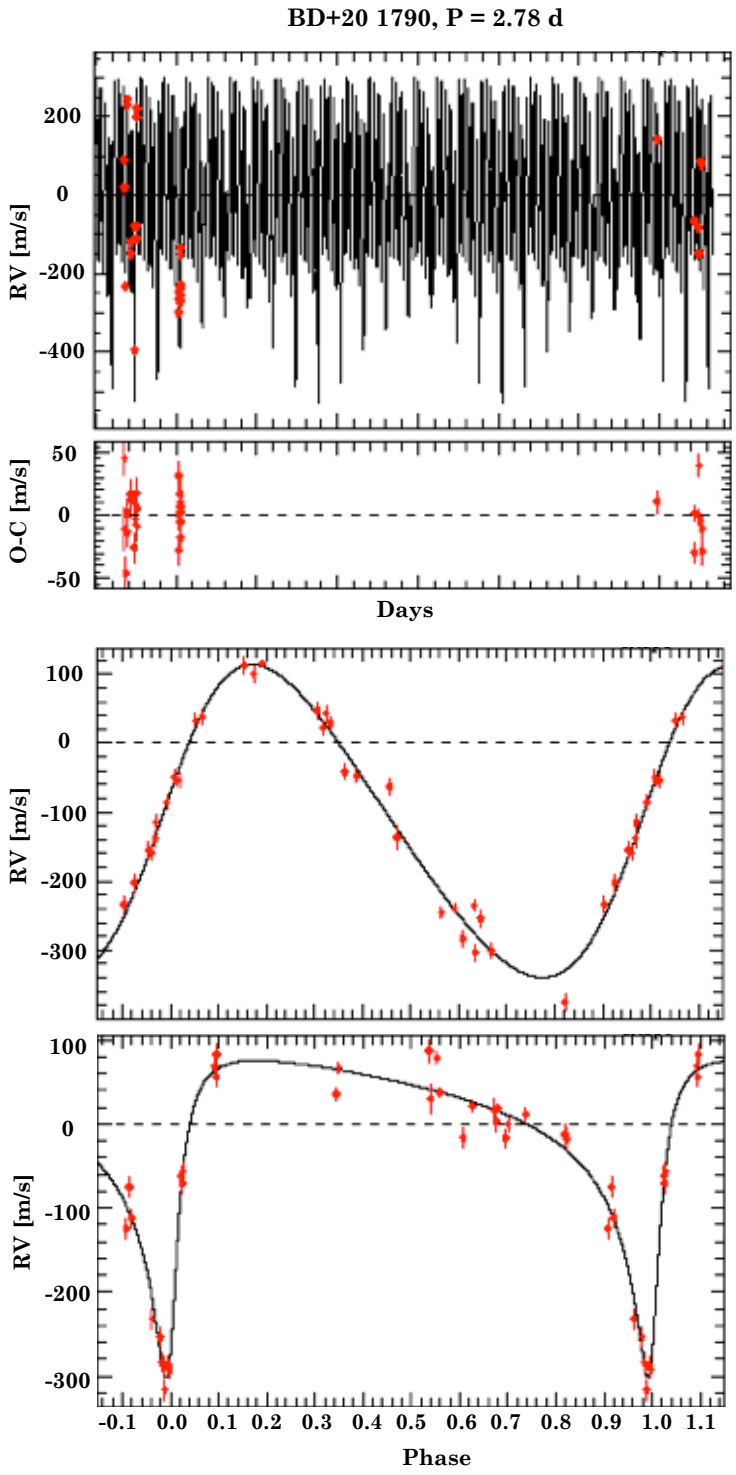

Figure 4.17 2-Keplerian RV fit for K5 AB Dor member BD+20 1790. The bottom two panels show phased relative RVs with $P_1 = 2.78$ d and $P_2 = 14.26$ d. The total RV signal (top panel) is comprised of the RV contribution from the rotational period in addition to that of the companion's orbital period.

We then constrained the possible rotation and orbital solutions to include those reported by Hernán-Obispo et al. (2015) and we find a 2-Keplerian fit of $P_{rot} = 2.79$ d and $P_{orb} = 7.08$ d (see Figure 4.18). Our new P_{orb} has slightly better error bars than our initial solution of 14.26 d, so we conclude that this is the planet's orbital period.

We present the calculated orbital parameters we obtained in Table 4.2. The planet's projected mass $M \sin i$ (1.78 M_{Jup}) is indicative of a Jovian-mass planet. Its high eccentricity is interesting, but high RV variations produced by spots could also give the appearance of high eccentricity; this is the case for IS Eri and HD 189285. These additional data further support the presence of a planet, but more observations are necessary. As a member of AB Dor, this planet would be among the youngest known if it is confirmed.

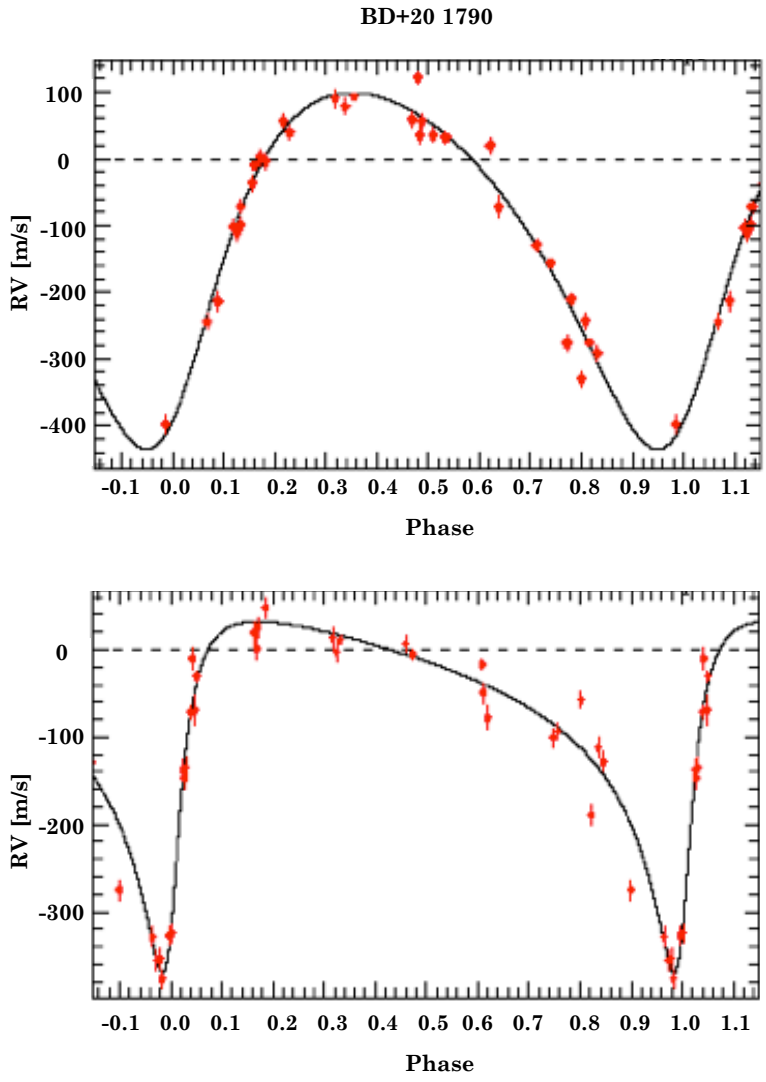

Figure 4.18 2-Keplerian RV fit for K5 AB Dor member BD+20 1790. The two panels show phased relative RVs with $P_1 = 2.79$ d (top panel) and $P_2 = 7.08$ d (bottom panel). Adding these two RV signals yields the total observed RV.

Table 4.2. Orbital Parameters of BD+20 1790 b.

Parameter	Solution
P_{orb}	7.0802 ± 0.0011 days
e	0.6879 ± 0.0339
$M_2 \sin i$	1.7789 M_{Jup}

4.2.3.4 V577 Per A

V577 Per A is a G5 AB Dor member (McCarthy & White 2012), and Nielsen & Close (2010) report it as a wide binary. McCarthy & Wilhelm (2014) report a $v \sin i$ of 8.9 km/s but no rotation period has previously been detected; we report a $v \sin i$ of 9.07 km/s.

Our periodogram analysis of V577 Per A (Figure 4.19) reveals a significant peak at ~ 3 d (FAP $< 0.1\%$), with another series of peaks at P/2 (~ 1.5 d). In Figure 4.20 we show that the RV fitting converges nicely on a P_{rot} of 3.19 d; however, a periodogram of the RV residuals shows that the ~ 3 d peak still persists.

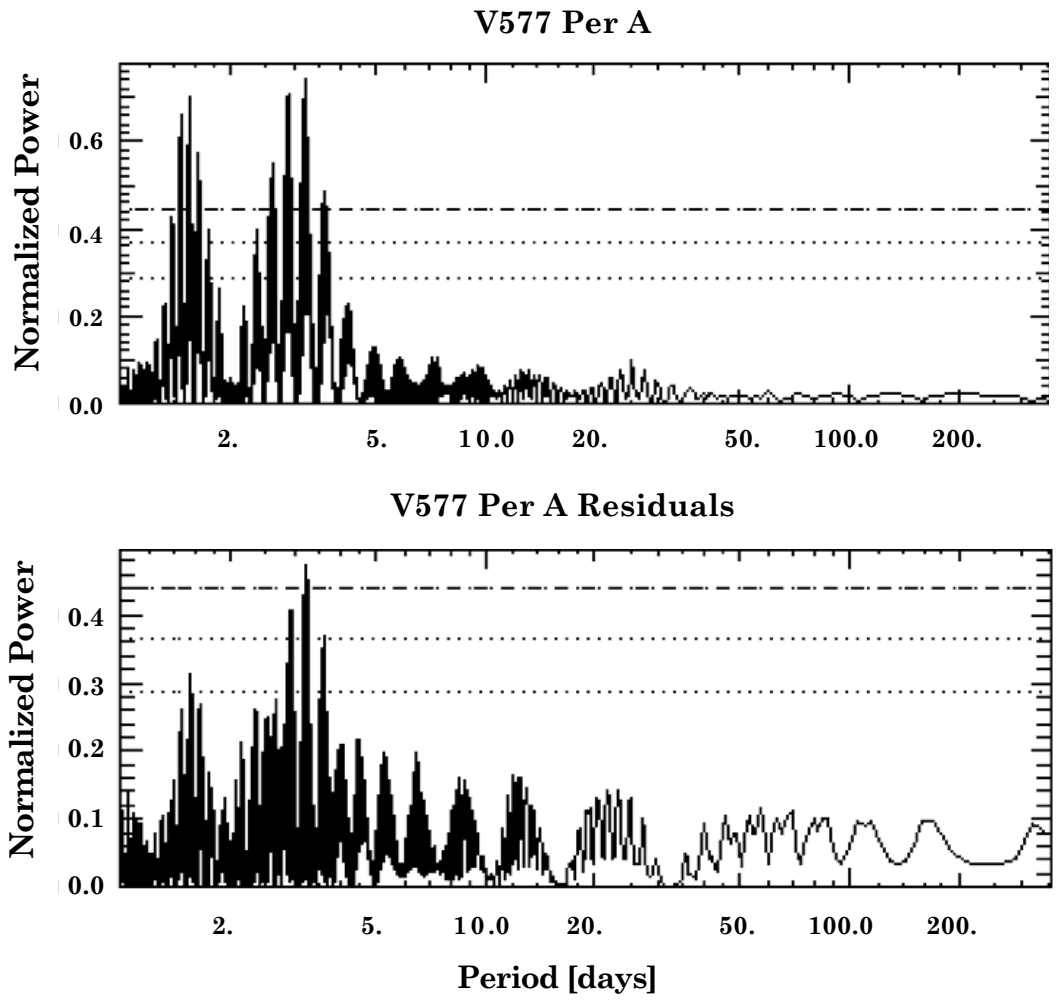

Figure 4.19 *Top Panel*: Periodogram for the G5 AB Dor member V577 Per A. The strongest peak at $\sim$ 3 d (and resonance peak at P/2$\sim$ 1.5 d) has a FAP $< 0.1\%$. *Bottom Panel*: Periodogram of RV residuals for V577 Per A, where a strong peak at $\sim$ 3 d persists (FAP $<$ 0.1%).

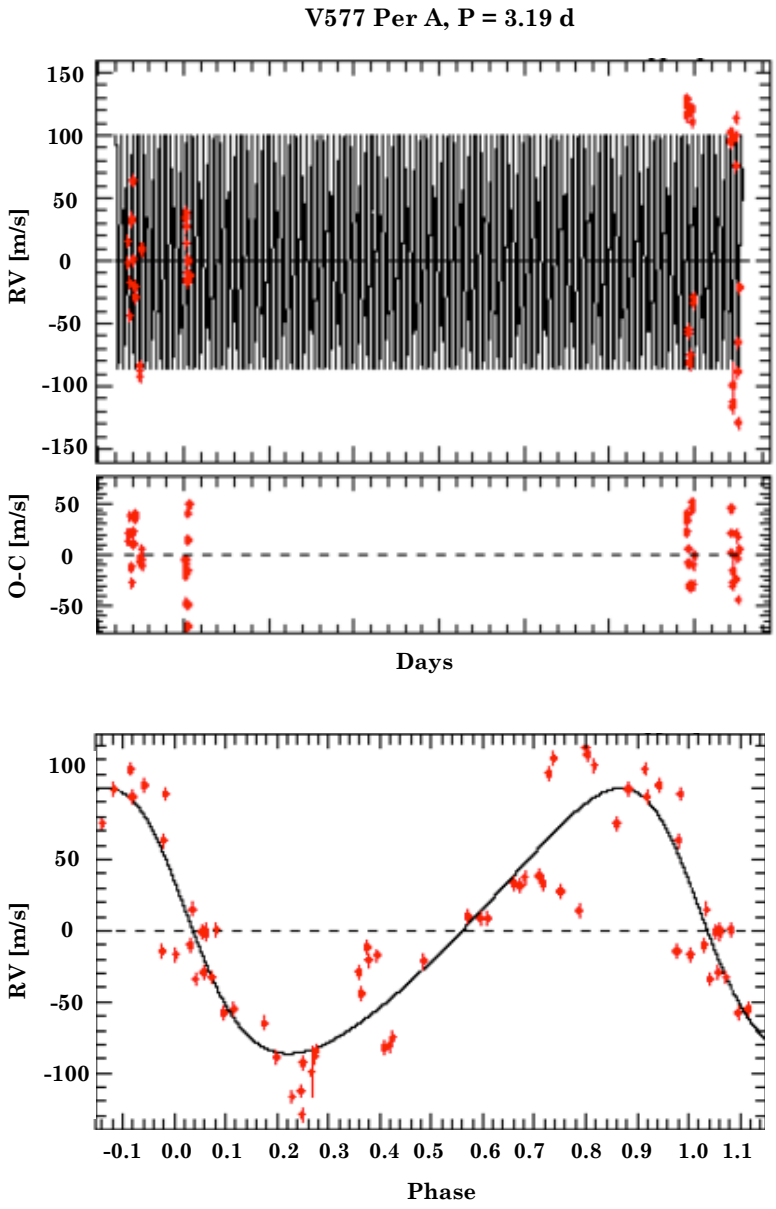

Figure 4.20 Keplerian RV fit for G5 AB Dor member V577 Per A. The bottom panel shows the phased relative RVs with P_{rot} = 3.19 d.

To test if these residuals vary due to spot evolution, we independently fit the two observing seasons (Δt = 359 d). We find that the RV fit converges on $P_{rot}\sim$ 3.2 d for both seasons,

but with slight variations in the period and more significant variations in the RV amplitude ($\sim$ 120 m/s in season 1 versus $\sim$ 240 m/s) as well as phase and shape of the RV curve. This could indicate either poor sampling within seasons or surface spots located at different latitudes *between* seasons, which would result in slightly different P_{rot} measurements due to differential rotation. We thus adopt the initial P_{rot} solution of 3.19 d.

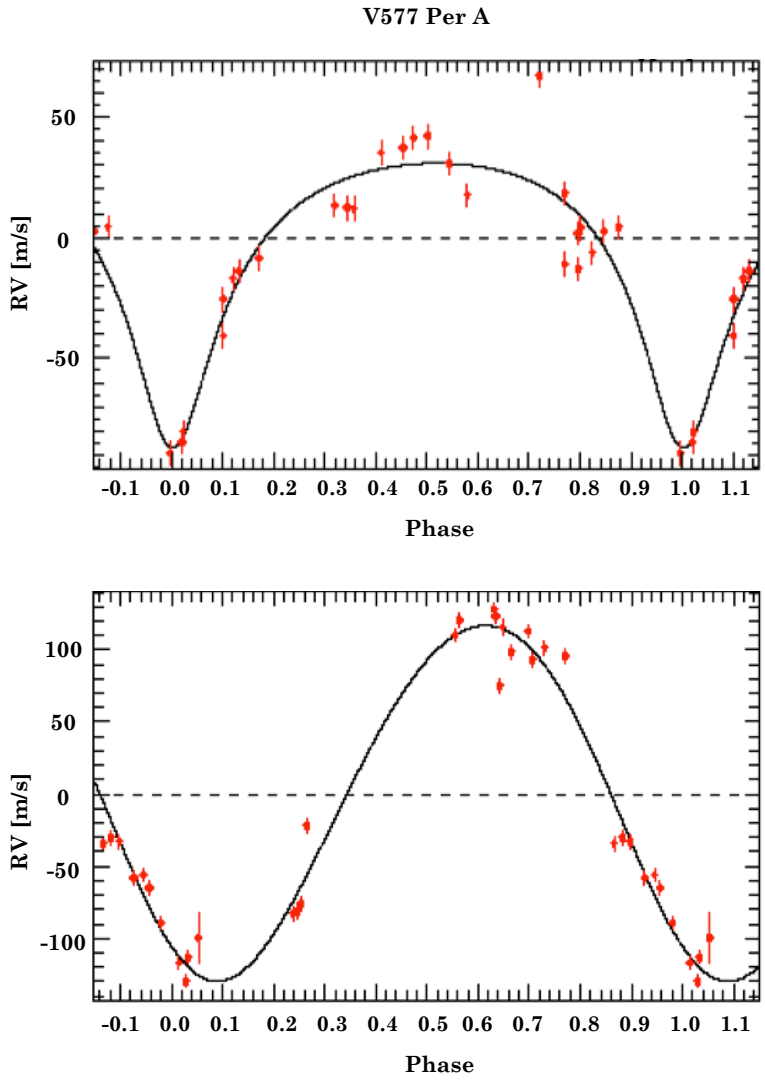

Figure 4.21 Keplerian RV fit for G5 AB Dor member V577 Per A. The two panels show phased relative RVs from season 1 (top panel) with $P_1 = 3.18$ d and season 2 (bottom panel) with $P_2 = 3.21$ d.

4.3 Chromatic Effects on Stellar Properties

Since surface features such as star spots can cause wavelength-dependent RV shifts, we investigate evidence for this at optical wavelengths by dividing the SOPHIE spectra into

Table 4.3. Summary of Spectrum Division

Star	Blue Orders	Red Orders	Blue Wavelength Range (Å)	Red Wavelength Range (Å)	Blue Photon Count	Red Photon Count	% Difference
BD+20 1790	0-29	30-38	3872.4 - 5885.8	5868.7 - 6943.5	691248	621170	10%
HD 189285	0-27	28-38	3872.4 - 5693.2	5673.4 - 6943.5	612669	599041	2%
V577 Per A	0-27	28-38	3872.4 - 5693.2	5673.4 - 6943.5	2950437	2580960	13%
IS Eri	0-28	29-38	3872.4 - 5787.9	5769.4 - 6943.5	1820174	1549033	15%

red and blue orders and measuring RV shifts in each regime. We chose to divide the full spectrum for each star such that the blue and red halves contain similar photon counts in order to achieve similar RV precisions. This is determined from the maximum number of counts per pixel in the CCF per order, which traces the SNR for that order. Having exactly equal photon counts is not possible given the discrete nature of the orders, but we minimized the difference as much as possible. A summary of the red/blue spectrum division is outlined in Table 4.3.

The percent difference in photon counts between red and blue orders ranges from 1% to 15%, and the average difference is 9.5%. Once the blue and red orders are separated, we conduct an identical cross-correlation analysis of each spectrum, as we have done with the full spectra (described in Section 3.2.2). This provides RV values for all blue and red spectra, using the appropriate spectral mask for each star. We then compare blue and red RVs (RV_{blue}, RV_{red}) as follows.

For the 4 RV variable stars with a clear bisector-RV correlation and a known rotation period, we compare RV_{blue} to RV_{red} with respect to time. We see a small but distinct amplitude difference, with RV_{red} having a smaller amplitude for each star as we expected; Figure 4.22 illustrates this amplitude difference.

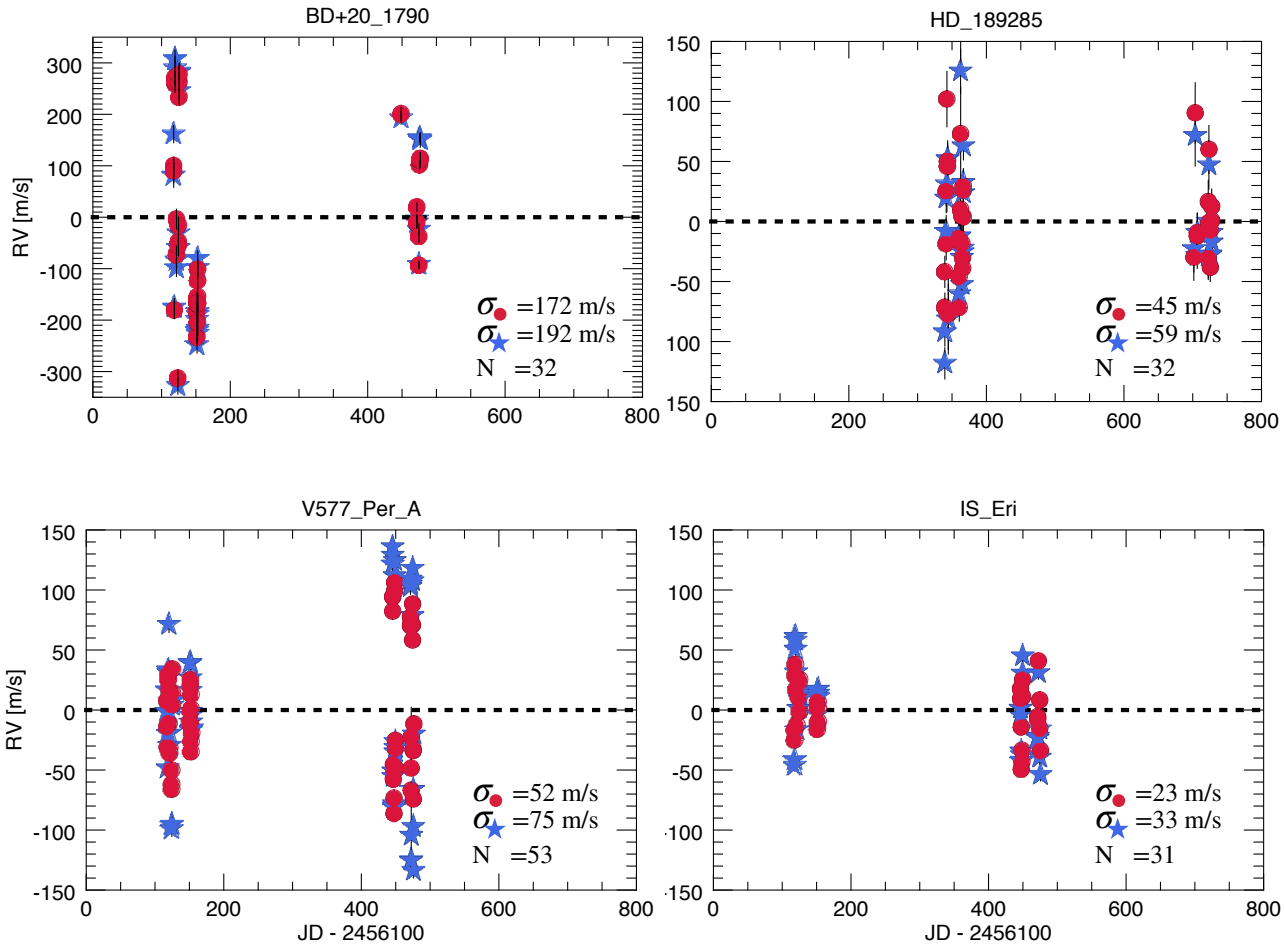

Figure 4.22 Blue (circles) and red (stars) relative RVs versus time for 4 RV variable stars.

A better way to illustrate the chromatic effect on RV is to consider the difference between blue and red RVs ($RV_{blue} - RV_{red}$) and the RVs derived from the full SOPHIE spectrum (RV_{total}). If offsets are caused by spots, we should see a larger difference when the offsets are the largest (furthest from zero). This relationship is linked directly to the temperature offset between the spot and the stellar surface. In Figure 4.23 we show that all 4 RV variable stars show the largest differences in RV_{blue} and RV_{red} when at the largest RV offsets.

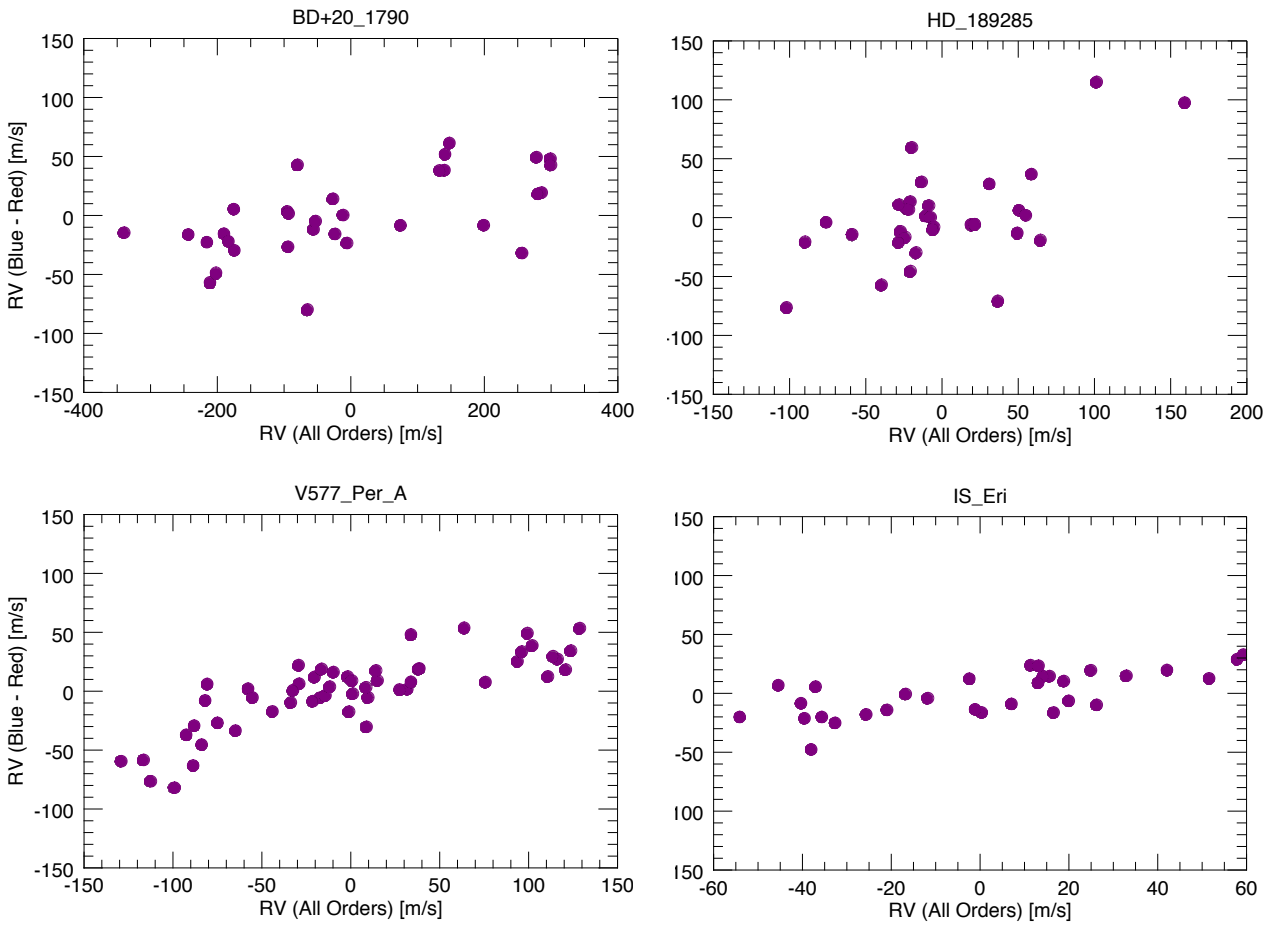

Figure 4.23 Chromatic offset $RV_{blue} - RV_{red}$ versus relative RV_{total} for the 4 RV variable stars.

4.4 Spots Not Planets and the Effectiveness of Activity Indicators

The 4 RV variable stars show bisector span variations that are anti-correlated with RV variations, and RV amplitudes that show a clear wavelength dependence. From these results we can conclude that the dominant cause of the RV variations observed for these stars is a consequence of stellar activity and not an orbiting companion. The one exception is BD+20 1790, for which evidence of a planet with semi-amplitude of 180 m/s is seen after removing a more dominant signal of semi-amplitude 220 m/s, likely caused by spots (see Figure 4.18).

The value of FWHM measurements in identifying activity induced RV variations is less convincing. The 4 RV variable stars exhibit large, measurable FWHM changes, so in principle observed changes in the FWHM value could warn of activity. However, the lack of any clear correlation with RV variations makes the interpretation difficult. It is possible that higher spectral resolution measurements could possibly demonstrate a correlation with RV variations.

Using the periodicity of the RV variability, we have demonstrated how star spots can interfere with the detection of planets. Their spot induced RV amplitudes range from ~ 175 m/s to ~ 675 m/s, and thus mimic short period (i.e. "hot") gas giants. These RV variations are also "eccentric-like" in shape, which may cast doubt on claims of young eccentric planets. Our analysis confirms that, as expected for spots, the shape of the RV curve changes over time as the spot pattern changes also. Our analysis suggests that if a Keplerian fit is forced to RV variations caused by spots, the best fit often has a high eccentricity and could be a red flag. This should serve as a cautionary tale to groups searching for young exoplanets using the RV method: spotted young stars can easily fool even the most cautious of observers.

We were also able to confirm the presence of activity on the 4 RV variable stars through a chromatic analysis of our SOPHIE spectra. To our knowledge, the chromatic effect on RV variability has never been observed simultaneously in two wavelength regions. Previous comparisons of RV amplitudes in the optical and IR used observations that are several months apart, during which time the stellar spots could have evolved (Huélamo et al. 2008). The comparison of blue versus red orders of optical spectra can be conducted without the need for further observations at longer wavelengths.

4.5 Implications for The Spectroscopic Effects of Spots

Our results for BD+20 1790 (see Figures 4.16 and 4.17) illustrate our capacity to obtain a very accurate Keplerian curve for a planet after filtering the RV jitter. Theoretically, the relationship between the bisector span and the RV could be used to remove the variations stemming from activity. However, as studies such as Boisse et al. (2009) have shown, this technique can reduce the amplitude of the RV variation but not its quasi-sinusoidal pattern.

Instead, we can combine methods that have been successful in other studies to remove activity variations and gain a deeper understanding of young stellar spots. One such method is Doppler Imaging (DI), which involves using high-cadence spectroscopic data to reconstruct temperature maps of the star at different phases of its rotation (e.g. Cole et al. 2015). These maps can be used to locate the spots (say, where the temperature difference is > 1000 K compared to the rest of the surface) and to derive spot temperatures. The strategies implemented in this work, with dense sampling of several RV measurements during one rotational period of the star, are ideal for this technique.

In another study, Boisse et al. (2011) modeled the effects of spots on several observable parameters with the SOAP software package (Boisse et al. 2012). In conjunction with stellar and instrument parameters, SOAP takes spot parameters such as longitude, latitude, and size as input and outputs the RV, bisector span, and flux as a function of the stellar phase. With the spot sizes and locations obtained from DI, we can use SOAP to model the phased RV curve produced by surface spots of the young stars we observed with SOPHIE.

Using the model of phased RV produced by SOAP, we can then filter out the RV variations from activity. The recent young exoplanet discovered by Donati et al. (2016) around the T-Tauri star V830 Tau was found by combining DI and RV modeling to filter out jitter

contributions to the RV, revealing the planet signal underneath. We propose using such a technique on the Sun-like stars studied here as possible future work (see Chapter 7).

4.6 Planet Detection Limits with SOPHIE

Despite our conclusion that the RV variations are not caused by planets, these data can nevertheless provide valuable information on the limits of what companions can be detected around young Sun-like stars with SOPHIE. In this section, we present the results of Monte Carlo simulations we conducted to investigate the completeness of our null detection.

Using an IDL program developed by collaborator S. Quinn, we conduct a P(χ^2) test to determine the probability that, given our data set, a constant velocity star would produce the observed RV variation. We define a detection as a simulated RV with P(χ^2) value $<$ 0.001, or 99% confidence of variability. Given the temporal sampling of our observations, the program uses our measured RV, RV errors, an estimated stellar mass, and the average jitter of stars of that age (see Chapter 5) to simulate 1,000,000 planetary systems of varying eccentricities and inclinations at a particular orbital period (P_{orb}) and planetary mass (M_P). For these simulations, we let the planet mass range from 0.1 to 13 M_{Jup} and we consider the orbital period regions of $0.3 < P_{orb} < 10$ days, $10 < P_{orb} < 30$ days, and $30 < P_{orb} < 100$ days.

We conducted this analysis on the 4 RV variable stars we observed with SOPHIE. Since these stars are all members of AB Dor, we used the average jitter we determined for this moving group (see Chapter 5). Figure 4.24 is an example of a completeness map generated by the simulation, where each colored square represents the percentage of planets we would have detected of the 1,000,000 simulated at that P_{orb} and M_P. For planets with $P_{orb} > 7$

days, we use the eccentricity distribution for giant planets (e.g. Jurić & Tremaine 2008); for $P_{orb} < 7$ days, we assume the orbits to be circular. The inclinations are geometrically weighted. As illustrated by Figure 4.24, P_{orb} and M_P dominate the RV at the extreme points (low P_{orb}, high M_P or high P_{orb}, low M_P), where the RV signal will be either too high or too low to be impacted by other factors such as inclination and eccentricity. However, in the central regions of the map, pole-on systems and planets that spend most of their orbit far away from their host can have a larger influence on the relatively weaker RV signal and therefore the detection probability.

We present the fraction of giant planets detected in these period ranges in Table 4.4. As expected, the detection frequency declines as companions with larger periods are considered, since they exert smaller RV variations over longer timescales. Our objective for this study was to search for short-period giant planets; Table 4.4 illustrates that our null detection is "real," with a detection frequency of over 90% within $0.3 < P_{orb} < 10$ days. In other words, we see no evidence for giant planets at short orbits around these stars because they are not there. If our survey is mostly sensitive to short period, Jupiter-mass planets and we do not observe any, then perhaps the distribution of young planets differs from that of old field stars, or they have not had time to migrate. Additional high cadence observations of more young stars could provide important insight on the distribution of young giant planets.

Table 4.4. Planet Detection Frequency for RV Variable Stars with SOPHIE

Star	Estimated Stellar Mass ($M_\odot$)	Detection Frequency ($P = 3 - 10\,d$)	Detection Frequency ($P = 10 - 30\,d$)	Detection Frequency ($P = 30 - 100\,d$)
BD+20 1790	0.7	92%	86%	81%
HD 189285	0.9	91%	85%	78%
V577 Per A	0.9	92%	87%	82%
IS Eri	0.8	91%	86%	81%

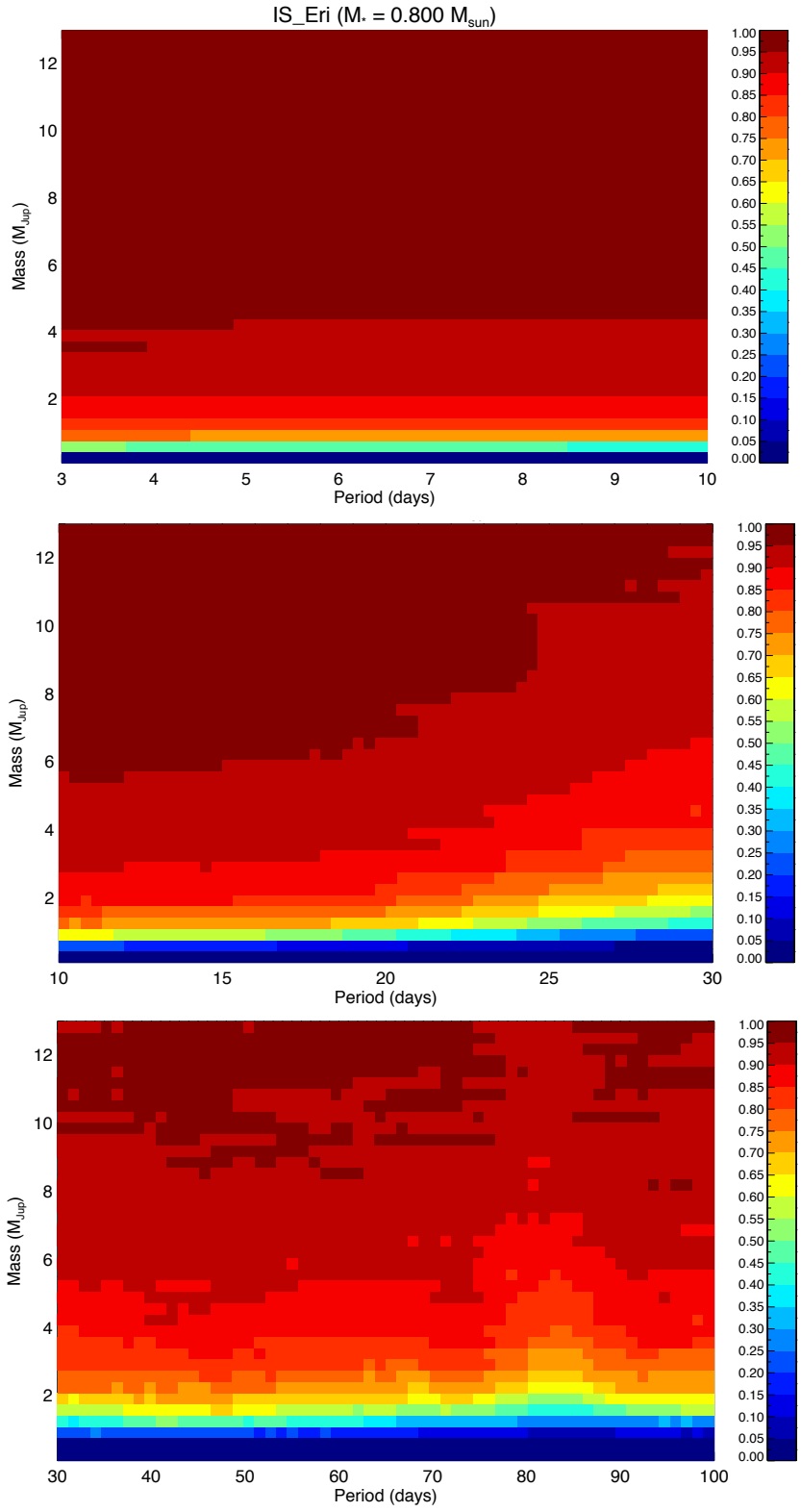

Figure 4.24 An example of a completeness map generated by the Monte Carlo simulation of potential planets around the AB Dor member IS Eri using SOPHIE data. Detection frequency of giant planets of mass $0.1 < M < 13 M_{Jup}$ for the orbital period regions of 3−10 d (top panel), 10−30 d (middle panel), and 30−100 d (bottom panel). The stellar mass for IS Eri (0.8 M$\odot$) was estimated from its K0 spectral type.

– 5 –

How Stellar Jitter Declines with Stellar Age

The previous chapter illustrates the stellar jitter induced by spots and activity of young stars. Since it is well known that both activity and stellar rotation decline with age (e.g. Skumanich 1972; Mamajek & Hillenbrand 2008), we expect stellar jitter to decline with age as well. To investigate the age dependence specifically, we combine our new optical stellar RV dispersion measurements with published RV dispersion measurements of young stars (<1 Gyr) with known ages. For the assembled sample, we select only results for Sun-like stars, which we have defined as having a spectral types between F6 and K5 (inclusive).

5.1 The Assembled Sample of Young Nearby Suns

In addition to new measurements presented in this study (see Chapter 4), the following spectroscopic surveys of young stars report RV uncertainties < 65 m/s, and are considered precise enough to measure stellar jitter: Paulson et al. (2004 ; hereafter PCH04), Paulson & Yelda (2006 ; PY06), Quinn et al. (2012 ; Q12), Lagrange et al. (2013 ; L13), and Quinn et al. (2014 ; Q14). The assembled studies do not include stars younger than $\sim 10\ Myr$ since most surveys of very young stars target non Sun-like stars (e.g. Crockett et al. 2012) or are observed at infrared wavelengths (e.g. Bailey et al. 2012; Gagné et al. 2016), or have candidate companions (e.g. Johns-Krull et al. 2016).

5.1.1 Young Open Clusters

Three of these surveys have targeted open clusters with ages less than 1 Gyr, namely the Hyades (PCH04, Q14) and Praesepe (Q12). PCH04 monitored 93 stars of varying spectral types in the Hyades; we exclude the 42 stars cooler than K5, leaving 51 Sun-like Hyades

members. Q14 monitored 27 FGK stars in the Hyades; we exclude the discovered planet host, a spectroscopic binary, 2 stars with RV uncertainties greater than 65 m/s, 3 stars hotter than F6, and 4 stars cooler than K5, leaving 16 Sun-like Hyades members. Q12 monitored 53 FGK stars in the Praesepe open cluster; we exclude the two planet hosts and 5 stars hotter than F6, leaving 46 Sun-like Praesepe members.

5.1.2 Young Associations and Moving Groups

The remaining surveys have targeted young, nearby associations and moving groups including IC 2391, Castor, and Ursa Majoris (PY06), as well as AB Doradus, Argus, and Tucana Horologium (L13); both teams observed the β Pictoris moving group.

PY06 monitored 61 stars, including 28 field stars with approximate age estimates. However, we exclude the field stars since their age estimates are not as precise as the ages of stars in moving groups or open clusters; we also exclude stars with large RV uncertainties (> 65 km/s), stars hotter than F6, and stars cooler than K5. The total number of stars gleaned from the PY06 survey for our purposes is 24, and spans 3 coeval populations; 8 stars are IC 2391 members, 7 are Castor members and 9 are Ursa Majoris members.

L13 monitored 26 stars, including 4 members of AB Dor, 3 members of Argus, 5 members of β Pic, 4 members of Tuc Hor, 7 young field stars, and one star each from the TW Hydrae association (TWA), the Columba association, and the Carina moving group. We excluded the field stars, 9 stars hotter than F6, and a spectroscopic binary. The total number of stars gleaned from this survey for our purposes is 12; they span 6 coeval populations.

From our survey we include 6 members of AB Dor observed with the TRES and SOPHIE spectrographs. As with the other surveys, we only considered stars with spectral types

between F6 and K5, without a spectroscopic stellar companion, and with RV uncertainties $< 65\ m/s$. We exclude BD+20 1790, which has a large RV variation, possibly due to a planetary companion (see Section 4.2.3.3).

5.2 RV Dispersions and Stellar Jitter

The assembled compilation consists of 113 stars from open clusters, with ages of 578 ± 12 Myr and 750 ± 100 Myr (Delorme et al. 2011; Brandt & Huang 2015 respectively). It also includes 42 stars from nearby young moving groups and associations, with ages spanning from 10 to 500 Myr. The individual dispersion measurements, spectral types, and $v \sin i$ for moving group members are provided in Table 5.2, while the slightly more extensive and uniform open cluster measurements are from the original studies (Paulson et al. 2004; Quinn et al. 2012, 2014).

Using the assembled properties, we can provide a statistically meaningful assessment of how stellar jitter changes with stellar age. We calculate stellar jitter by subtracting RV uncertainties from RV dispersions for each star in quadrature, then we average stellar jitter for each group; we do not weight averages by number of observations. Table 5.2 summarizes the jitter measurements for the assembled compilation; it includes median spectral types, mean $v \sin i$ values, and RV dispersions and uncertainties. Individual ages and age references are also listed in Table 5.2. Because the methods and techniques vary between surveys, we assemble the results of individual studies separately; thus, AB Dor and the Hyades are represented more than once.

Table 5.1. Individual RV Dispersions of Young Moving Groups and Associations

Name	Group	SpT	N	$v \sin i$ (km/s)	σ_{RV} (m/s)	RV_{unc} (m/s)	Ref.
IS Eri	AB Dor	G5	32	6.78	31.7	5.6	This work
HD 189285	AB Dor	G7	32	9.18	53.8	9.5	This work
V577 Per A	AB Dor	G5	53	9.07	71	9.8	This work
HD 17332 A	AB Dor	G1	10	13.3	49	15.5	This work
HD 17332 B	AB Dor	G6	9	2	20.2	6.7	This work
HD 152555	AB Dor	G0	23	18.1	44.7	9.3	This work
HD 37572	AB Dor	K0	15	9.6	65.1	1.5	L13
HD 45270	AB Dor	G1	13	17.7	33.9	1.7	L13
HD 217343	AB Dor	G5	16	13.3	104.5	2.5	L13
HD 224228	AB Dor	K3	14	5.7	2.5	0.9	L13
HD 61005	Argus	G8	12	9.7	40.1	2.6	L13
HD 133813	Argus	G9	2	13.3	2.2	5.2	L13
HD 174429	β Pic	G9	22	79.6	407.3	27.5	L13
HD 181327	β Pic	F6	40	17.9	15.1	3.2	L13
HD 42270	Carina	K0	2	31.2	82.7	11.8	L13
HD 987	TucHor	G8	11	7.3	90.9	2.5	L13
HD 207575	TucHor	F6	27	32.8	40.6	7.4	L13
HD 102458	TWA	G4	16	28.1	331.7	9.8	L13
BD+01 2063	IC 2391	G5	14	4	30	20	PY06
HD 111813	IC 2391	K1	4	3.8	50	60	PY06
HD 118100	IC 2391	K5	10	14	100	40	PY06
HD 120352	IC 2391	K0	9	3.2	60	40	PY06
HD 140913	IC 2391	G0	3	9	40	30	PY06
HD 142072	IC 2391	G5	8	6.1	80	60	PY06
HD 157750	IC 2391	G3	8	3.4	70	50	PY06
HD 209779	IC 2391	G5	7	6.8	30	60	PY06
BD+24 2700	Castor	K0	8	2	60	50	PY06
HD 41842	Castor	K1	22	3	50	40	PY06
HD 77825	Castor	K2	10	2	70	40	PY06
HD 94765	Castor	K0	11	2	50	30	PY06
HD 103720	Castor	K3	9	–	70	40	PY06
HD 181321	Castor	G2	8	14	60	40	PY06
HD 216803	Castor	K4	7	3	50	50	PY06
BD+19 2531	Ursa Major	K2	8	1.5	60	40	PY06
HD 165185	Ursa Major	G1	8	7.7	80	60	PY06
HD 26913	Ursa Major	G8	23	8.5	90	40	PY06
HD 38392	Ursa Major	K2	16	1	70	40	PY06
HD 41593	Ursa Major	K0	6	3.8	30	60	PY06
HD 60491	Ursa Major	K2	13	5.4	60	40	PY06
HD 64942	Ursa Major	G5	28	8.5	70	50	PY06
HD 81659	Ursa Major	G6	19	1	50	30	PY06
HD 88654	Ursa Major	G5	17	–	40	40	PY06

Note. — Individual RV dispersions for stars in young nearby moving groups and associations. Spectral types for this work were obtained from McCarthy & White (2012). RV dispersions and uncertainties were used to calculate stellar jitter for each group, listed in Table 5.2.

Table 5.2. Jitter Analysis from Optical RV Surveys of Nearby Moving Groups and Clusters

Group	Age	Age^a	N^b	Median^c	$<v \sin i>$	<Jitter>	$\sigma_{Jitter}{}^d$	RV
	(Myr)	Ref.		SpT	(m/s)	(m/s)	(m/s)	Ref.
TWA	10 ± 3	B15	1	G4	28.1	331.6	210.6	L13
β Pic	24 ± 3	B15	2	G2.5	48.8	210.6	210.6	L13
Carina	45^{+11}_{-7}	B15	1	K0	31.2	81.9	36.0	L13
Tuc Hor	45 ± 4	B15	2	G2	20.1	65.6	36.0	L13
Argus	30 ± 10	D13	2	G8.5	11.5	20.8	31.6	L13
AB Dor	149^{+51}_{-19}	B15	4	G7.5	11.6	51.5	43.7	L13
AB Dor	149^{+51}_{-19}	B15	6	G5	9.7	44.1	17.7	This work
IC 2391	30 ± 10	D13	8	G5	7.8	42	47.1	PY06
Castor	200 ± 100	B99	7	K1	2.3	41	19.7	PY06
Ursa Major	500 ± 100	K03	9	G8	4.7	37	38.9	PY06
Praesepe	578 ± 12	D11	46	G5.4	4.8	24.1	11.4	Q12
Hyades	750 ± 100	BH15	16	K4	4.4	21.8	14.1	Q14
Hyades	750 ± 100	BH15	51	G5	4.8	16	9.4	PCH04

Note. —
[a] Ages references: B15 = Bell et al. (2015); D13 = De Silva et al. (2013); B99 = Barrado y Navascues (1998); K03 = King et al. (2003); D11 = Delorme et al. (2011); BH15 = Brandt & Huang (2015).
[b] N is the number of stars observed in each group.
[c] Spectral types for this work were obtained from McCarthy & White (2012).
[d] σ_{Jitter} is the standard deviation of the individual jitter values for each group. The σ_{Jitter} value for TWA is assumed to be that of β Pic. The σ_{Jitter} value for Carina is assumed to be that of Tuc Hor.

We illustrate the relationship between average jitter and stellar age in log-linear space in Figure 5.2. The vertical error bars represent the standard deviation of the individual jitter measurements for each group. TWA and Carina have only one jitter measurement each, and we could not compute their σ_{Jitter} values; we therefore adopt the σ_{Jitter} values of β Pic and Tuc Hor, respectively, as these groups are the closest age counterparts. For the β Pic jitter calculation there are only two data points: one has a large RV jitter value and the other a much smaller one (400 m/s vs. 14 m/s), probably due to projection effects. Thus, the large error bars indicate a broader range that is not well-constrained with two data points. More jitter calculations at young ages would provide a better sense of the ?true? distribution of RV jitter in these groups. Age errors are from the literature as listed in Table 5.2; we average the asymmetric age errors of AB Dor and Carina to convert them to symmetric errors.

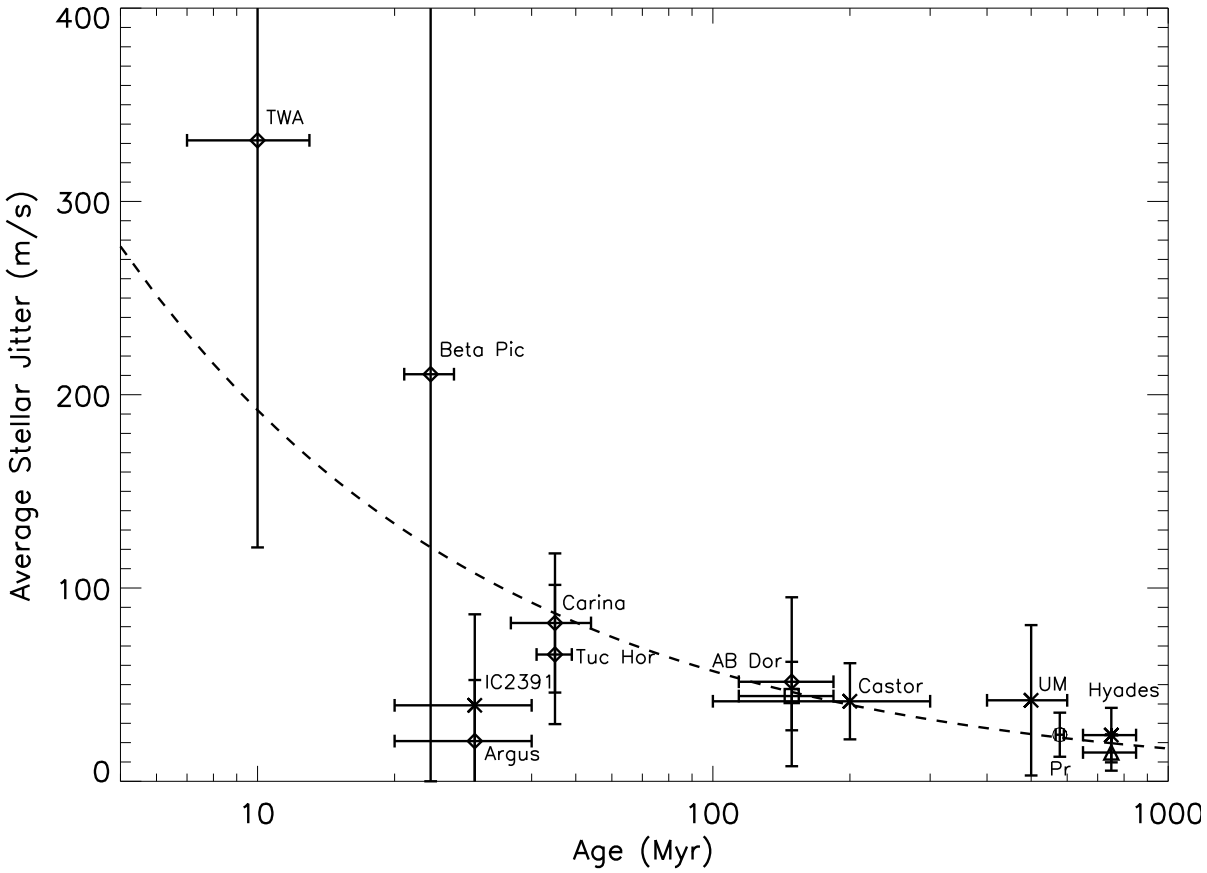

Figure 5.1 Average stellar jitter as a function of age for nearby moving groups and open clusters. A power law (dotted line) was fit to the data with a resulting $\tau \sim -0.53$, similar to a Skumanich curve. Vertical error bars represent the jitter measurement dispersions. Age errors were obtained from the literature; we averaged the asymmetric age errors of AB Dor and Carina to convert them to symmetric errors. A quantitative summary of these results is presented in Table 5.2.

Figure 5.2 shows an overall decreasing amount of stellar jitter with age. There is a steep drop between 8 Myr and 30 Myr, which then levels off. There is a large scatter of $\sim$ 120 m/s at 10 Myr that decreases to $\sim$ 50 m/s at 100 Myr and to $\sim$ 20 m/s at 500 Myr. To derive an approximate functional form of this decline with age, we fit a power law to the data using the IDL routine MPFIT, weighted by the errors. The power law has the functional form of

$$J = c\,\tau^{\alpha}, \tag{5.1}$$

where J is the stellar jitter in m/s and τ is the age in Myr. The best fit finds α = -0.53 $\pm$ 0.13 and c = 646.39. The resulting best fit exponent is remarkably close to that of the classic Skumanich law (Skumanich 1972), which states that stellar rotation declines with age as $\alpha^{-0.5}$.

While other power laws have been proposed to explain how rotation declines with age (e.g. dos Santos et al. 2016), the majority of theoretical and observational work finds an exponential decay that agrees to $\pm$ 0.1 to that of Skumanich. We caution that our best fit is heavily dependent upon the limited number of measurements of the youngest Sun-like systems. The average stellar jitter for β Pic includes only two largely differing jitter measurements of Sun-like stars (406.4 m/s versus 14.8 m/s); the latter measurement is probably low due to projection effects and disproportionately contributes to the measured RV dispersion. Additional jitter measurements for Sun-like stars at very young ages ($<$ 50 Myr) would provide a better sense of the true distribution of RV jitter in those groups, and thus establish a better relationship between stellar jitter and stellar age.

5.3 Implications for Exoplanet Detection

The increasing stellar jitter of young stars over time has negative implications for the detection of planets via the RV technique. The previous analysis enables us to begin investigating the age at which RV detection becomes ineffective, on average. For comparison, we note that the semi-amplitude of the periodic RV variation from a planetary companion is:

$$K \approx 6.54 \times 10^3 m s^{-1} \left(\frac{P}{3days}\right)^{-\frac{1}{3}} \left(\frac{M_p}{M_J}\right) \left(\frac{M_*}{M_\odot}\right)^{-\frac{2}{3}} (1-e^2)^{\frac{1}{2}} \sin i. \tag{5.2}$$

In the simple case of a hot Jupiter (M_p =1 M_J, P_{orb} = 3 days) with an edge-on, circular orbit ($i = 90°$, e = 0) around a 1 $M_\odot$ star, the semi-amplitude K $\approx$ 141 m/s (Blake et al. 2007). We consider the semi-amplitude of a hot Jupiter because these are the easiest to detect and they are the only type detected via RVs around youthful stars (e.g. Quinn et al. 2012; Donati et al. 2016; Hernán-Obispo et al. 2015).

Based on our best fit power law, the average stellar jitter will exceed 141 m/s for ages less than 20 Myr. The stellar jitter only drops below 47 m/s (a 3σ detection) above an age of $\sim$ 100 Myr. While many observations can be used to detect RV signals that are at or below the noise level (e.g. Anglada-Escudé et al. 2016 - Proxima Centauri b), this is in practice very difficult. We conclude that stellar jitter is likely to inhibit the RV detection of most planets around stars younger than 100 Myr unless longer wavelength measurements are used for confirmation (e.g. Johns-Krull et al. 2016) or techniques are developed to mitigate the distorting effects on spectral lines (e.g. Donati et al. 2016)

– 6 –

Near-Infrared Spectroscopy of Young Stars

Several studies have shown that the reduced contrast between the stellar photosphere and cool star spots at longer wavelengths relative to optical wavelengths results in reduced stellar jitter measurements (e.g. Prato et al. 2008; Mahmud et al. 2011; Bailey et al. 2012). This can be especially useful in exoplanet searches around young stars, since reduced jitter could make the slight reflex motion of a planetary companion easier to detect. However, very few longer-wavelength RV studies have targeted young Sun-like stars. In this chapter we present the results of our near-infrared (NIR) young Sun-like star survey conducted at the NASA Infrared Telescope Facility (IRTF).

6.1 Near-Infrared Sample

We obtained high dispersion near-infrared (NIR) spectra of a representative sample of 8 young Sun-like stars to test if the expected reduced contrast between star spots and the photosphere translates to improved sensitivity in this wavelength region. As with our optical survey, this sample consists of young Sun-like stars identified in the field (White et al. 2007) and as members of the moving groups AB Dor and β Pic (e.g. McCarthy & White 2012). All but one of the stars are effectively single, having no visible companions within 5; the exception is the young field star V835 Her, a spectroscopic binary.

The observed sample includes 6 stars with $v \sin i$ <20 km/s that were monitored strategically for RV variation (BD+20 1790, V577 Per A, IS Eri, HD 189285, HD 38230, V835 Her). These stars were contemporaneously monitored with SOPHIE, with observing nights either overlapping or within days of the CSHELL observations; the SOPHIE measurements

are highlighted in Chapter 3. We also observed 2 stars with no known $v \sin i$ (HIP 14809, HD 14082B) for the purpose of determining their $v \sin i$ (dubbed Reconnaissance stars; see Table 6.1) in order to more completely determine the properties of nearby young Sun-like stars (see Chapter 2). Reconnaissance stars determined to have $v \sin i < 20$ km/s could be included in future young planet searches with the RV method. The sample of 6 monitored stars includes spectral types ranging from G1 to K5, K magnitudes that range from $5.35 - 7.84$ mag, and $v \sin i$ values that range from $2.1 - 12.9$ km/s.

Most notably, our aim was to investigate whether contemporaneous observations at NIR and optical wavelengths would enable us to better distinguish an exoplanet detection from stellar activity, as the spot topology is not expected to change on the order of hours to days. Because of the large geographical separation of the two telescopes, simultaneous observations were not possible even when granted time on the same data; however, the time difference is only 12 hours, making our multiwavelength observations the closest taken of young stars to date.

6.2 Observations

We obtained our NIR data using the CSHELL spectrograph, a high-resolution echelle spectrograph mounted on the 3 m IRTF in Mauna Kea, Hawaii (Tokunaga et al. 1990; Greene et al. 1993). CSHELL uses a circular variable filter to isolate a single order of the spectrum. We used the high-resolution mode (0.5 slit, resolving power $\sim 40,000$) in the H-band, centered on the photospheric magnesium (Mg) lines at 1.576 μm with a window of 0.003 μm. We achieved precise relative wavelength calibration using telluric methane absorption features that are superimposed on the Mg lines at 1.576 μm, as illustrated in Figure 6.1; this

is analogous to the iodine absorption cell used in high-precision optical studies (e.g. Blake et al. 2010; Bailey et al. 2012). Theoretically, the abundance of spectral features in this wavelength range would allow us to measure radial velocities to a precision of $\sim$ 50 m/s, following the prescription outlined by Butler et al. (1996).

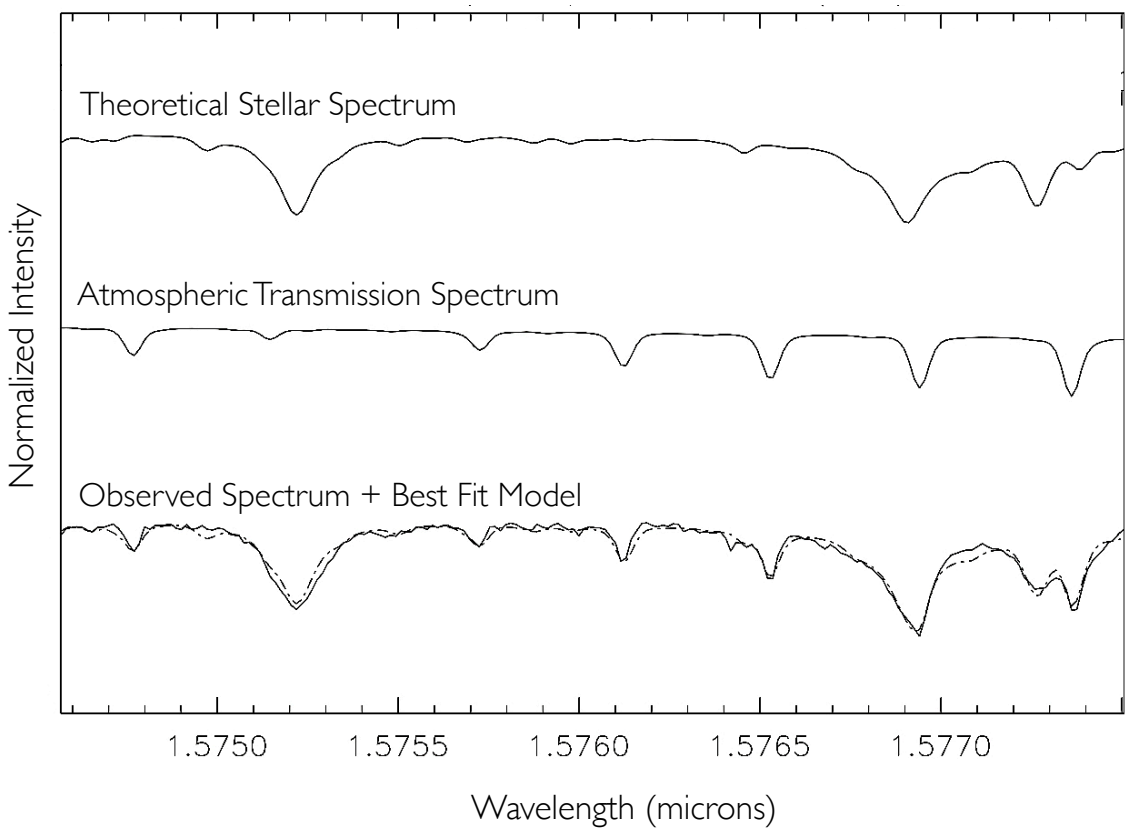

Figure 6.1 An example of our NIR spectral fitting routine as applied to V577 Per A. The observed spectra are modeled by combining a synthetic stellar spectrum (top) with a telluric spectrum (middle) that provides an absolute wavelength reference. The observed CSHELL spectrum of V577 Per A is shown (solid line; bottom) in comparison with the best fit model spectrum (dotted-dashed line; bottom). The mean residuals of the best-fit spectrum in this case are 2.42%.

Two consecutive observations of each star were obtained by "nodding" along the slit, meaning that the star was positioned near the top of the vertical slit for the first observation,

then positioned near the bottom for the second observation. The vertical nod separation is approximately 10. Exposure times were set to obtain a signal-to-noise ratio (SNR) of 100 based on previous sensitivities measured during good weather (SNR = 100 for H = 6.5 in 9 minutes).

In addition to the stellar spectra, we also obtained 20 flats and darks with integration times of 20 seconds each night. Several spectra of the standard A1V star Sirius (or the A0V star Vega, depending on the observing season) were also obtained each night for wavelength calibration purposes and to determine the instrumental profile. These stars have no absorption lines in the observed wavelength region so any lines in the spectra would originate from telluric lines in the Earth's atmosphere.

Our observing strategy for CSHELL was similar to that of SOPHIE. CSHELL observations were obtained in two runs of ~ 4 half-nights each scheduled about a month apart in order to be sensitive to Jupiter mass planets ($m \sin i > \sim 0.5\ M_{Jup}$) with orbital periods of a few days, as well as slightly longer period Jupiter mass companions. We obtained data over a temporal baseline of 2 years, spanning between 18 October 2012 and 17 June 2014.

6.3 Reduction, Extraction, and Analysis

To reduce the CSHELL spectra, we first median-combine the dark-subtracted flat images for each night to make a master flat, then divide the spectral images by the master flat to correct for pixel-to-pixel light variations. We then subtract nodded pair images from each other, which allows us to subtract sky emission, dark current, and detector bias from the spectra; we assume that changes in the instrumental profile are negligible in the minimal

time between nods. Once the images are calibrated, we use a bad pixel mask to replace hot or dead pixels with a zero value.

We then perform an optimal spectral extraction, developed by Horne (1986) and modified for nodded pairs (Bailey et al. 2012). Compared to a standard extraction, which simply sums the vertical pixels of the 2-dimensional spectrum to obtain a 1-dimensional spectrum, this method uses a weighted variance to sum the vertical pixels, giving preference to the central pixels where the signal is higher.

To obtain RV and $v \sin i$ values we fit the optimally extracted spectra with a model composed of high-resolution spectra convolved to the resolution of CSHELL. The model is a composite between PHOENIX models pertaining to the star's spectral type (Husser et al. 2013) and telluric models extracted from KPNO/FTS empirical telluric solar spectra (Livingston & Wallace 1991); however, we used a T=4900 K, log g=4.5 synthetic template for all stars as an approximate solar spectrum. We use a pipeline developed by Bailey et al. (2016) for observations in the NIR K-band at 2.3 μm, which we optimized for use in the H band for this program. A full description of this method is provided in Bailey et al. (2016), but we provide a general description here.

Our routine fits 11 total parameters: the limb darkening coefficient is set to 0.6, which is appropriate for cool stars at NIR wavelengths (Claret 2000), while the other 10 are allowed to vary. Of the variable parameters, 3 are for the quadratic wavelength solution and 1 is a Gaussian used to fit the spectral point-spread function (PSF). The remaining parameters include one variable each to describe the depth of features in the telluric and synthetic spectra, $v \sin i$, RV, and 2 normalization constants. The $v \sin i$ is calculated following the prescription in Gray & Corbally (2009) with the adopted limb darkening coefficient. Our

fitting routine then takes these initial guesses and uses them to fit each stellar epoch, from which we obtain RVs and $v \sin i$. Errors in RV are calculated based on the number of telluric and stellar features and SNR, as described in Butler et al. (1996); this accounts for statistical RV uncertainties but not systematic uncertainties. Since $v \sin i$ is not expected to change over time, we adopt the dispersion of individual $v \sin i$ measurements as the $v \sin i$ uncertainty.

6.4 Radial and Rotational Velocity Measurements

6.4.1 Rotational Velocity Measurements

Here we discuss the $v \sin i$ results for the 7 effectively single stars monitored with CSHELL; a separate discussion of the newly identified spectroscopic binary V835 Her is provided in Section 6.7.

Because each spectrum provides a $v \sin i$ estimate, we take the mean of these as the measured $v \sin i$ and the dispersion of individual $v \sin i$ values as the uncertainty. Mean $v \sin i$ values for each of the 6 monitored stars are reported in Table 6.1 and range from 4.3 km/s to 18.4 km/s. Of these, V577 Per A, IS Eri, and HD 189285 have mean $v \sin i$ values that agree to within 2σ with the mean $v \sin i$ measured contemporaneously with SOPHIE. The 2 remaining stars have mean $v \sin i$ that are about twice the value measured with SOPHIE: BD+20 1790 and HD 38230. This may point to a limitation of the fitting prescription used, including a possible mismatch of the single adopted stellar template (see Section 6.5). Individual epochs of the determined $v \sin i$ for the 6 stars monitored with CSHELL are presented in Appendix B, Tables B.1 to B.5; each $v \sin i$ epoch represents the average of two nodded spectra.

Table 6.1. Summary of Near-Infrared Spectroscopic Observations

Star	SpT	N	$< v \sin i >$	$\sigma_{v \sin i}$ [1]	$< RV >$	RV_{unc}	σ_{RV} [3]
		(km/s)	(km/s)	(km/s)	(km/s)	(km/s)	(km/s)
HD 14082B[3]	G1	1	13.01	···	5.811	0.017	···
HIP 14809[3]	G1	1	14.56	···	5.753	0.022	···
BD+20 1790	K5	6	17.71	0.51	7.655	0.032	0.273
V577 Per A	K2	12	9.62	2.13	-4.683	0.020	0.140
IS Eri	G8/K0	13	5.113	1.29	15.23	0.018	0.283
HD 189285	G7	11	12.81	0.35	-18.512	0.025	0.369
HD 38230	K0	10	4.25	2.79	-28.547	0.015	0.206
V835 Her	G8+K7	22	18.444	0.57	-16.719	0.019	26.647

Note. —
[1]The $v \sin i$ dispersion ($\sigma_{v \sin i}$) is the standard deviation of the individual $v \sin i$ measurements.
[2]The RV dispersion (σ_{RV}) is the standard deviation of the individual RV measurements.
[3]Single epoch stars, for which $\sigma_{v \sin i}$ and σ_{RV} is not reported.

Measured $v \sin i$ values of the 2 Reconnaissance stars observed with CSHELL are also reported in Table 6.1. These stars were observed to obtain their $v \sin i$ values only, in order to determine their feasibility for future inclusion in young planet searches with the RV method. The average $v \sin i$ values for the Reconnaissance stars HD 14082B and HIP 14809 were 13.0 km/s and 41.9 km/s, respectively; thus, only HD 14082B may be viable for future observations for RV planet searches.

6.4.2 Radial Velocity Measurements

A summary of the results for the CSHELL observations is presented in Table 6.1. We averaged multiple epochs for each star to obtain the mean RV ($< RV >$) and mean RV uncertainties ($< RV_{unc} >$). The RV dispersion (σ_{RV}) is simply the standard deviation of the individual RV values and includes internal errors and photon noise, but also physical variations such as stellar jitter. Here we discuss the RV results for the 7 effectively single stars monitored with CSHELL; a discussion of the newly identified spectroscopic binary V835 Her is provided in Section 6.7.

Of the 5 effectively stars monitored with CSHELL, 4 have mean RV values that agree to within 2σ with the mean RVs measured contemporaneously with SOPHIE: BD+20 1790, IS Eri, HD 189285 and HD 38230. The mean RV value for V577 Per A measured with CSHELL (-4.68 $\pm$ 0.02 km/s) is consistent with the measured SOPHIE values (-5.37 $\pm$ 0.01 km/s) to $\sim$ 1 km/s, but do not agree within 2σ; we are uncertain of the cause of the offset in this case.

Individual epochs of the determined RV and uncertainties along with Julian date for the 6 stars monitored with CSHELL are presented in Appendix B, Tables B.1 to B.5. We observed on average 2 epochs per star per night, with each epoch representing the average of two nods. The collective observations span a temporal baseline of 2 years. CSHELL RV results for the AB Dor members BD+20 1790, V577 Per A, IS Eri, and HD 189285, and the young field star HD 38230 are illustrated in Figure 6.2; their observed RV dispersions range from 140 to 369 m/s.

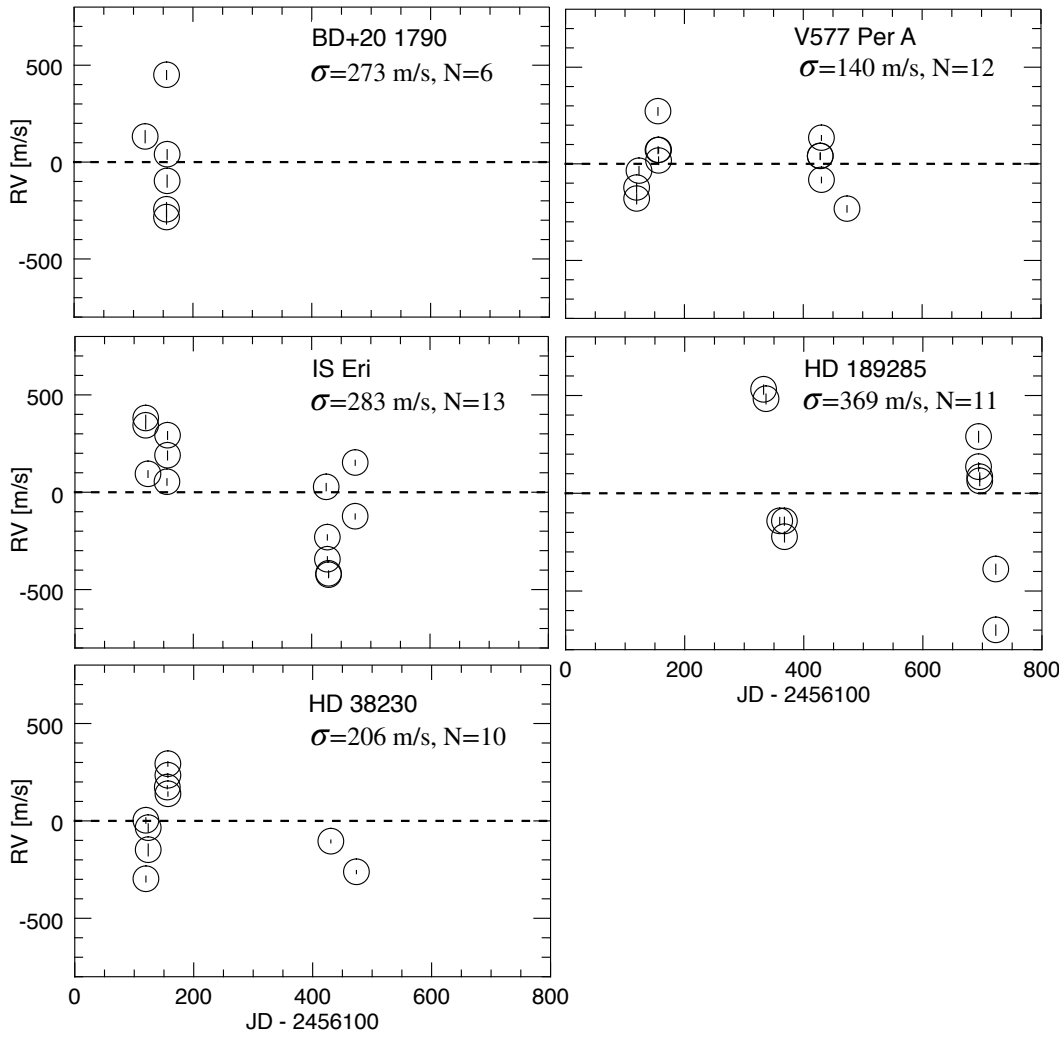

Figure 6.2 Near-infrared relative RV measurements of the AB Dor members BD+20 1790, V577 Per A, IS Eri, and HD 189285, and the young field star HD 38230.

6.5 Radial Velocity Precision at 1.576 μm with IRTF CSHELL

While observations at NIR wavelengths are expected to mitigate the effects of star spots and enable clearer exoplanet detection, accomplishing this requires using a technique that can achieve sufficient RV precision. Here we empirically investigate the RV precision achieved using CSHELL at 1.576 μm with Sun-like stars.

Since no RV standards were observed, we use the low RV dispersion star HD 38230 to assess the precision of our NIR RV measurements. We note that while we observed a σ_{RV} <8 m/s for HD 38230 at optical wavelengths, NIR observations of HD 38230 yielded σ_{RV} of 206 m/s. Since this is much larger than the theoretical RV dispersion expected ($\sim 50m/s$), we expect that there are systematic errors introduced by the 1980s generation detector (see Tokunaga et al. 1990) that are not accounted for in our analysis. One factor may be the small observing window for CSHELL (∼29 Å) that contains only 3 strong stellar absorption features (see Figure 6.1) and is more susceptible to biases caused by features Doppler shifting on or off the edge of the detector. Because the RV precision depends on the number of stellar and telluric absorption features, the model is not as well-constrained when computing the wavelength solution, resulting in poorer RV precision.

For comparison, we note that the best achieved precisions for CSHELL are 55 m/s (Crockett et al. 2012) and 68 m/s (Davison et al. 2014). Both of these studies utilized a slightly larger wavelength window (54 Å vs. 29 Å) with more densely spaced stellar and telluric lines for cooler K and M stars in the K band. With achieved precisions of about ∼50 m/s in the IR, it is possible to compare the RV jitter measured at optical wavelengths to those measured at IR wavelengths (e.g. Bailey et al. 2012). In this case such a comparison is not meaningful because instrumental effects dominate the observed scatter at IR wavelengths.

The H-band work presented here has been a pioneering effort to observe hotter stars that do not have strong stellar and telluric features in the K band. Our RV measurement dispersions confirm that the theoretical precision obtainable is optimistic. Future observations with the newly installed iSHELL (Tokunaga et al. 2016), a multi-order echelle spectrograph

that has recently replaced CSHELL, will likely yield much more desirable results because it will encompass more stellar lines.

Possible improvements to the measured RV precision in this data set could include further steps in post-processing. For example, since our fitting routine is sensitive to initial guesses for the variable parameters, a more thorough analysis of the data to fine-tune the initial guesses would be beneficial. Perhaps a more robust calculation of the barycentric corrections based on the prescription by Wright & Eastman (2014) could be implemented to help account for RV offsets, although we do not expect this to be a significant contributor the large RV dispersions we observe. More importantly, a careful choice of the synthetic stellar models matched to the known parameters of each star may also improve the spectral fitting and therefore the RV precisions. Despite these issues, the achieved precision of 200 m/s is roughly a factor of 5 better than previous measures of stars in the IR that relied on emission lamps for calibrations (e.g. Prato 2007), and equally better than the design specifications of the instrument (Tokunaga et al. 1990). The consistent radial velocities over a 2 year baseline rule out the majority of short period brown dwarfs around our 6 monitored stars.

6.6 Planet Detection Limits with CSHELL

As demonstrated with SOPHIE in Chapter 4, the IR RV data we obtained can provide information on the limits of planet detection around young Sun-like stars with CSHELL. Using the method described fully in Section 4.6, we conducted a Monte Carlo simulation to investigate the completeness of our null detection.

Figure 6.3 is an example of the completeness maps generated by the simulation in each orbital period range. For planets with $P_{orb} > 7$ days, we again use the eccentricity distribution

Table 6.2. Planet Detection Frequency for RV Variable Stars with CSHELL

Star	Estimated Stellar Mass ($M_\odot$)	Detection Frequency ($P = 3 - 10\,d$)	Detection Frequency ($P = 10 - 30\,d$)	Detection Frequency ($P = 30 - 100\,d$)
BD+20 1790	0.7	28 %	11 %	4 %
HD 189285	0.9	45 %	27 %	14 %
V577 Per A	0.9	46 %	28 %	13 %
IS Eri	0.8	51 %	33 %	16 %

for giant exoplanets (e.g. Jurić & Tremaine 2008); for $P_{orb} < 7$ days, we assume the orbits to be circular. The inclinations are geometrically weighted.

We conducted this analysis on the 4 RV variable stars observed with CSHELL. Because the jitter for stars of this age and at this wavelength range is not well known, we used 266 m/s, the average CSHELL RV dispersion of these 4 stars as the jitter. Again, we restricted the mass range to $0.1 - 13\ M_{Jup}$; the orbital period regions investigated are $0.3 < P_{orb} <$ 10 days, $10 < P_{orb} < 30$ days, and $30 < P_{orb} < 100$ days.

We present the fraction of giant planets detected in these regions in Table 6.2. As expected, the detection frequency declines as companions with larger periods are considered. Compared to SOPHIE observations (see Section 4.6), our CSHELL data is not as sensitive to short-period giant planets, which can be attributed to the limitations mentioned above. The median giant planet detection frequency we achieve within $0.3 < P_{orb} < 10$ days is 45.5 %. Better detection limits could be achieved with the suggested improvements at IR wavelengths as well as further high cadence observations of young Sun-like stars.

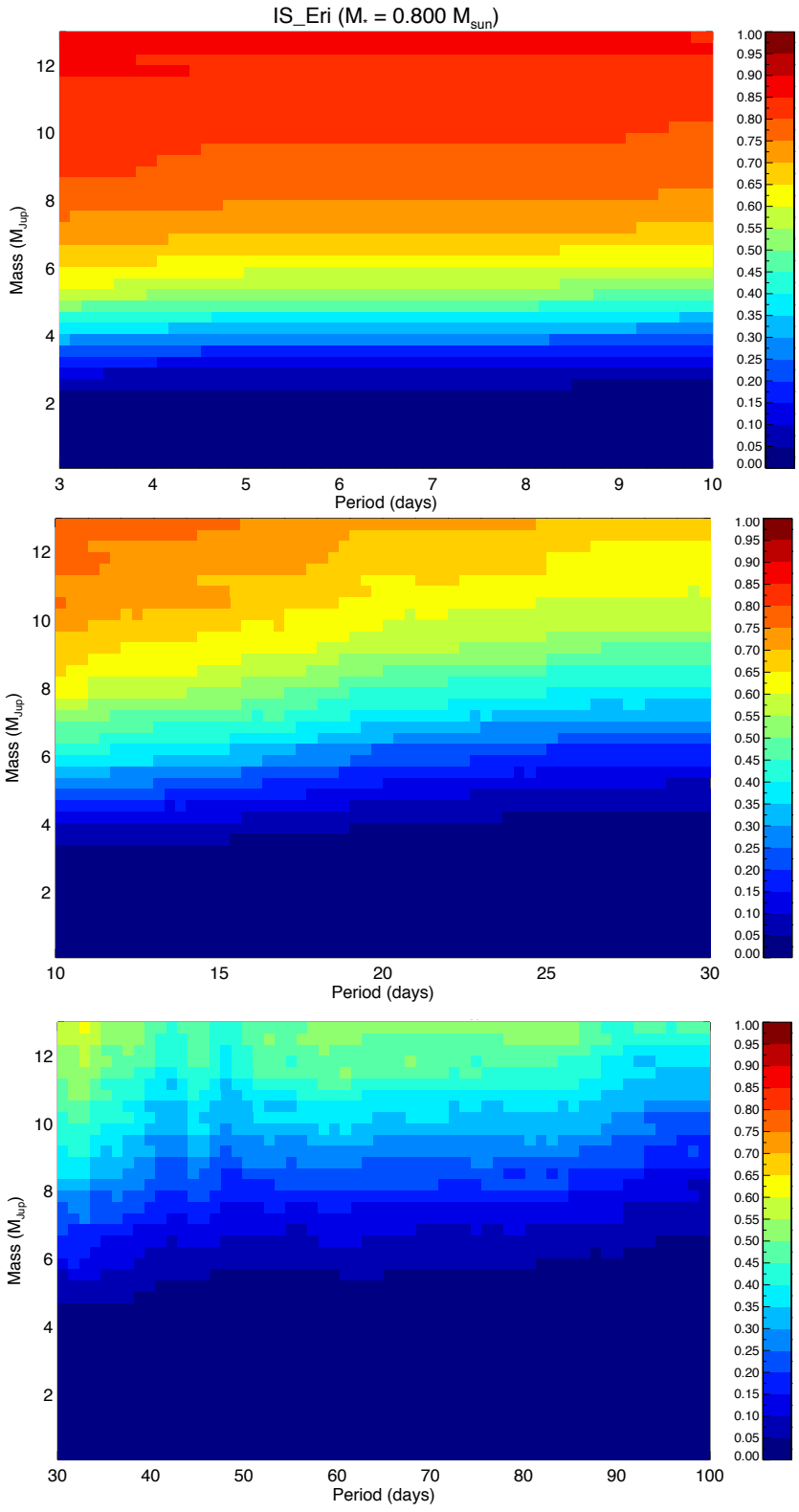

Figure 6.3 An example of a completeness map generated by the Monte Carlo simulation of potential planets around the AB Dor member IS Eri using CSHELL data. Detection frequency of giant planets of mass $0.1 < M < 13 M_{Jup}$ for the orbital period regions of 3−10 d (top panel), 10−30 d (middle panel), and 30−100 d (bottom panel). The stellar mass for IS Eri (0.8 M$\odot$) was estimated from its K0 spectral type.

6.7 The Spectroscopic Binary V835 Her

The modestly precise CSHELL RV measurements we have obtained enable us to conduct classic binary star analysis. In this section, we present our confirmation of V835 Her as a spectroscopic binary at both optical and infrared wavelengths. To summarize, the mean RV value for V835 Her measured with CSHELL (-16.72 $\pm$ 0.02 km/s) is consistent with the measured SOPHIE value (-17.97 $\pm$ 3.66 km/s). Individual RV and uncertainty measurements along with Julian date for the newly identified spectroscopic binary V835 Her are presented in Appendix B in Table B.6. We observed a total of 22 epochs for V835 Her with both CSHELL and SOPHIE, spanning a temporal baseline of 1 year.

As was noted for the single stars, we find that the mean $v \sin i$ for V835 Her measured with CSHELL and reported in Table 6.1 is about twice the value measured with SOPHIE (18.44 km/s vs. 8.83 km/s, respectively). Again, we note that a possible explanation could be the stellar template (see Section 6.5). Individual epochs of the $v \sin i$ for V835 Her measured with CSHELL are presented in Appendix B, Table B.6; each $v \sin i$ epoch represents the average of two nodded spectra.

Using Systemic Console 2 (Meschiari et al. 2009), an interactive software package to analyze exoplanetary data, we obtained a binary orbital fit of V835 Her. In Figure 6.4 we present the orbital fits at optical and IR wavelengths using SOPHIE and CSHELL data. The third panel in Figure 6.4 shows both optical (blue circles) and IR data (red circles); we corrected for a systematic 0.5 offset in JD that seems to stem from a conversion error.

In Table 6.3 we present the quantitative results of the orbital fits for V835 Her. We find the same orbital period with both SOPHIE and CSHELL data, and the eccentricities are coherent between the two data sets. Most importantly, we find a significant difference

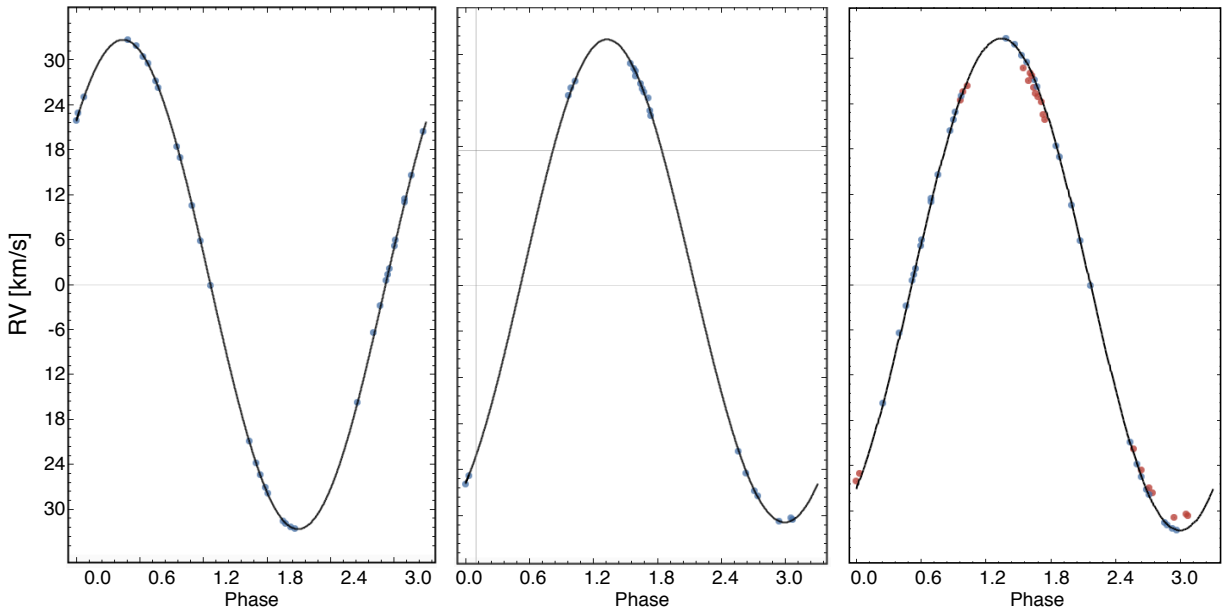

Figure 6.4 Optical and IR relative RV versus phase for the G5 young field binary V835 Her. *Left Panel:* Optical RVs observed with SOPHIE. *Middle Panel:* IR RVs observed with CSHELL. *Right Panel:* Optical and IR RVs plotted together, with P_{orb} = 3.30 d.

Table 6.3. Orbital Parameters of V835 Her at Optical and IR Wavelengths

Wavelength Regime	N	Period (d)	e	K km/s	RMS (km/s)
Optical	22	3.305	0.019	31.414	0.290
Infrared	22	3.304	0.000	32.640	0.105

of 1.226 km/s in the RV semi-amplitude (K) between the optical and IR data. With the orbital period being essentially equal to the rotational period (P_{rot} = 3.35 days; Hooten & Hall 1990), the binary components are likely tidally locked; this means that RV variations stemming from the binary companion are difficult to disentangle from the variations from stellar activity. However, the difference in K between optical and IR indicates that we have detected the activity signal. We note that this is a work in progress that will require a more robust analysis for confirmation.

– 7 –

Summary of Results

7.1 Dissertation Overview

A complete understanding of the properties of young Sun-like stars is essential for understanding the building blocks of planetary systems. In this dissertation we conducted a census and an assessment of young Suns in our own Solar neighborhood. Our goal was to elucidate the potential to find young exoplanets, which would shed light on our current understanding of giant planet formation. This work is important for NASA's *Kepler-2* and *TESS* missions, both of which will target young moving groups and open clusters and would benefit from our investigation of spectroscopic techniques that can distinguish activity from planets for young Sun-like stars.

Building on the existing body of knowledge in this field, we assembled a list of young Sun-like stars in the nearby young moving groups AB Doradus, β Pictoris, and Tucana Horologium and provided a statistical overview of their fundamental properties (Chapter 2). We then presented new projected rotational velocity and radial velocity measurements of a representative sample of 12 nearby young Suns in AB Doradus and in the field using high-dispersion optical spectroscopy (Chapter 3). In Chapter 4, we conducted a stellar activity analysis for a subset of young Suns observed with the SOPHIE spectrograph at the *Observatoire de Haute Provence*, including a study of the chromatic effects of stellar activity using the red and blue orders of the observed spectra. We then combined our optical spectroscopy results with results from the literature to study the relationship between stellar jitter and stellar age (Chapter 5). Finally, we presented new near-infrared spectroscopy of

6 young Suns obtained with CSHELL, taken contemporaneously with our SOPHIE data (Chapter 6).

7.2 Accomplishments of This Work

By studying Sun-like stars in nearby young moving groups we were able to gain insight into the statistical distribution of their fundamental properties as well as the effects of activity and implications for finding young exoplanets. Below we highlight the specific accomplishments made as a result of this work.

7.2.1 Properties of Young Nearby Suns

We found that about 50% of the nearest young Suns with known projected rotational velocities have $v \sin i$ values <20 km/s and 50% of the stars with known rotational periods have P_{rot} values <4 days. This implies that while single epoch RV measurements may achieve precisions of $\lesssim$100 m/s, multi-epoch RV accuracy is likely to be degraded by rotational induced activity. About 20% of the assembled sample does not have multiplicity information and less than 50% of the assembled sample are known multiples; a more complete assessment would be helpful for exoplanet searches. We also found that 7 of the 16 stars with the known properties necessary to calculate an inclination angle are nearly edge-on and ideal candidates for exoplanet searches with the transiting method.

7.2.2 Optical Spectroscopy

We presented optical spectroscopy of 12 nearby young Suns obtained with the TRES and SOPHIE spectrographs, which cover nearly the full optical spectral region with resolving powers R of 44,000 and 75,000, respectively. We identified a new spectroscopic binary star

(BD+05 4576), confirmed the known spectroscopic binary V835 Her, and presented new $v \sin i$ values for 3 stars. The high precision obtained with both spectrographs allowed us to assess the typical dispersions of young stars due to stellar jitter: about 40 m/s on average, with high-activity stars measuring up to 200 m/s.

7.2.3 RV Variability and Activity Analysis

We identified 4 RV variable stars with amplitudes of 45 - 210 m/s. However, based on a thorough analysis of young stars observed with SOPHIE we found a strong negative correlation between the measured bisector span and radial velocity for these 4 stars (BD+20 1790, HD 189285, V577 Per A, IS Eri); thus, the RV variables are interpreted as caused by star spots and not planets. Focusing on these 4 spotted stars, we also found that no such correlation exists for the full width at half maximum versus radial velocity of young stars, suggesting this may be a less effective technique. However, comparing FWHM to the stellar rotation phase may be more promising if the rotation period is well known. We also presented a stellar rotation period analysis for the 4 RV variables, reporting new measurements of P_{rot} for each. Through this analysis we tentatively confirmed the planetary companion around BD+20 1790 in the presence of activity. In our analysis of chromatic effects of activity, we showed that the red orders of the SOPHIE spectra yielded smaller jitter effects compared to the blue orders. This was the first analysis of its kind that has been done to date and shows that wavelength shifts of 0.015 μ, in the optical are sufficient to reveal RV variations caused by spots. Finally, we conducted a Montecarlo simulation to test our planet detection limits and found that, for SOPHIE data, we were sensitive to over 90% of close period (3−10 d) giant planets (0.1−13 M_{Jup}).

7.2.4 Jitter Dependence on Age

Using our new measurements along with those in the literature, we assembled a list of young Sun-like stars in nearby young moving groups and open clusters with known stellar jitter measured to a high precision ($RV_{unc} < 65$ km/s). With these values we were able to conduct an assessment of how stellar jitter changes with stellar age. We found that the stellar jitter falls off as $\tau^{-0.53\pm0.13}$ (where τ is the age of the star), which aligns remarkably well with the finding from Skumanich (1972) that stellar rotation period falls off as $\tau^{-0.5}$. This relationship indicates that stellar jitter is likely to inhibit exoplanet detection with the RV method for stars with ages < 100 Myr when observing at optical wavelengths alone.

7.2.5 Near Infrared Spectroscopy

We presented near-infrared spectroscopy of 8 nearby young Suns taken with the CSHELL spectrograph centered at 1.576 μm (R$\sim 40,000$), obtained contemporaneously with SOPHIE spectra and, to our knowledge, the first multiwavelength observing campaign of its kind. We presented new $v \sin i$ values for 2 reconnaissance stars in AB Doradus and monitored the 6 remaining stars. Unfortunately, the poor RV precision we obtained with CSHELL made it difficult to meaningfully compare this data to the optical wavelength region. RV dispersions measured with CSHELL averaged about 206 m/s, with the highest dispersion measurement at 369 m/s for HD 189285. We expect this is a consequence of the small CSHELL observing window (29 Å in the H band), where a smaller density of stellar and telluric features translate to less precise RV measurements. Nevertheless, this precision enabled us to map the orbit of the young field spectroscopic binary V835 Her. For this star, we discovered a significant different in the RV amplitude between the optical and IR data, which could be indicative

of stellar activity. Finally, we conducted a Montecarlo simulation of the 4 RV variable stars to test our planet detection limits and found that we were sensitive to 42% of close period (3−10 d) giant planets (0.1−13 M_{Jup}), on average.

7.3 Future Work

To bolster the research conducted for this dissertation, a number of improvements and additions could be made. Using the chromatic method to compare blue and red orders of optical spectra on the more slowly rotating young stars we could not include in our study would expand the activity information for young stars. Combining Doppler Imagine with models of the spot topology of young Sun-like stars using tools such as the SOAP package would allow for up to 90% of the RV variations from stellar jitter to be removed, which could enable the possible detection planet-induced RV variations beneath the jitter. The pioneering discovery by Donati et al. (2016) is a testament to this method, as is our tentative confirmation of a planetary companion around the active star BD+20 1790 once the spot RVs were removed.

To better constrain the relationship between stellar jitter and stellar age, additional measurements of Sun-like stars will be necessary, especially for ages of 10-20 Myr. An example of open cluster data contributing to this work is Bailey et al. (2016), who surveyed two ∼100 Myr clusters at optical wavelengths with the Michigan/Magellan Fiber System (M2FS; Mateo et al. 2012).

As mentioned in Chapter 6, a more careful analysis of the near-infrared spectra obtained with CSHELL could yield better results in terms of RV precision. Near-infrared observations using instruments with broader wavelength coverage, such as the newly installed iSHELL spectrograph at the NASA IRTF, may also yield radial velocity measurements with pre-

cisions high enough to mitigate stellar jitter effects and detect planetary companions. If contemporaneous observations with high precision optical spectra are obtained, a relationship between the semi-amplitudes of the RV variations in the two wavelength regimes could be used to subtract the signal induced by activity jitter.

Finally, obtaining spectropolarimetric data of young Sun-like stars with an instrument such as the upcoming SpectroPolarimètre InfraROuge (SPIRou; Moutou et al. 2015) will yield important information about their surface spot topology and activity patterns in two ways. First, spectropolarimetry can be used to model the activity-induced stellar jitter by studying the distortions of Stokes I profiles (e.g. Hébrard et al. 2016); second, by using the Zeeman signatures to recover the large-scale magnetic field of the star.

REFERENCES

Anglada-Escudé, G., et al. 2016, Nature, 536, 437

Bailey, III, J. I., Mateo, M., White, R. J., Shectman, S. A., Crane, J. D., & Olszewski, E. W. 2016, AJ, 152, 9

Bailey, III, J. I., White, R. J., Blake, C. H., Charbonneau, D., Barman, T. S., Tanner, A. M., & Torres, G. 2012, ApJ, 749, 16

Barrado y Navascues, D. 1998, A&A, 339, 831

Beatty, T. G., & Gaudi, B. S. 2015, PASP, 127, 1240

Bell, C. P. M., Mamajek, E. E., & Naylor, T. 2015, MNRAS, 454, 593

Berdyugina, S. V. 2005, Living Reviews in Solar Physics, 2, 8

Biller, B. A., et al. 2007, ApJS, 173, 143

—. 2010, ApJ, 720, L82

Blake, C. H., Charbonneau, D., & White, R. J. 2010, ApJ, 723, 684

Blake, C. H., Charbonneau, D., White, R. J., Marley, M. S., & Saumon, D. 2007, ApJ, 666, 1198

Boisse, I., Bonfils, X., & Santos, N. C. 2012, A&A, 545, A109

Boisse, I., Bouchy, F., Hébrard, G., Bonfils, X., Santos, N., & Vauclair, S. 2011, A&A, 528, A4

Boisse, I., et al. 2009, A&A, 495, 959

—. 2010, A&A, 523, A88

Bonfils, X., et al. 2013, A&A, 549, A109

Boss, A. P. 1997, in Lunar and Planetary Science Conference, Vol. 28, Lunar and Planetary Science Conference, 137

Bouchy, F., Pepe, F., & Queloz, D. 2001, A&A, 374, 733

Bouchy, F., et al. 2009, A&A, 505, 853

Brandt, T. D., & Huang, C. X. 2015, ApJ, 807, 58

Buchhave, L. A., et al. 2010, ApJ, 720, 1118

—. 2011, ApJS, 197, 3

—. 2012, Nature, 486, 375

Butler, R. P., Marcy, G. W., Williams, E., McCarthy, C., Dosanjh, P., & Vogt, S. S. 1996, PASP, 108, 500

Chauvin, G., et al. 2010, A&A, 509, A52

Claret, A. 2000, A&A, 363, 1081

Cole, E. M., Hackman, T., Käpylä, M. J., Ilyin, I., Kochukhov, O., & Piskunov, N. 2015, A&A, 581, A69

Courcol, B., et al. 2015, A&A, 581, A38

Crockett, C. J., Mahmud, N. I., Prato, L., Johns-Krull, C. M., Jaffe, D. T., Hartigan, P. M., & Beichman, C. A. 2012, ApJ, 761, 164

Cumming, A., Butler, R. P., Marcy, G. W., Vogt, S. S., Wright, J. T., & Fischer, D. A. 2008, PASP, 120, 531

Cutispoto, G., Pastori, L., Tagliaferri, G., Messina, S., & Pallavicini, R. 1999, A&AS, 138, 87

Cutispoto, G., Tagliaferri, G., de Medeiros, J. R., Pastori, L., Pasquini, L., & Andersen, J. 2003, A&A, 397, 987

Cutri, R. M., et al. 2003

David, T. J., et al. 2016, Nature, 534, 658

Davison, C. L., et al. 2014, AJ, 147, 26

De Silva, G. M., D'Orazi, V., Melo, C., Torres, C. A. O., Gieles, M., Quast, G. R., & Sterzik, M. 2013, MNRAS, 431, 1005

Delorme, P., Collier Cameron, A., Hebb, L., Rostron, J., Lister, T. A., Norton, A. J., Pollacco, D., & West, R. G. 2011, MNRAS, 413, 2218

Desidera, S., et al. 2015, A&A, 573, A126

Desort, M., Lagrange, A.-M., Galland, F., Udry, S., & Mayor, M. 2007, A&A, 473, 983

Donati, J.-F., et al. 2015, MNRAS, 453, 3706

Donati, J. F., et al. 2016, Nature, 534, 662

dos Santos, L. A., et al. 2016, A&A, 592, A156

Evans, T. M., et al. 2012, ApJ, 744, 120

Fabrycky, D., & Tremaine, S. 2007, ApJ, 669, 1298

Fűrész, G., Hartmann, L. W., Megeath, S. T., Szentgyorgyi, A. H., & Hamden, E. T. 2008, ApJ, 676, 1109

Figueira, P., et al. 2010, A&A, 513, L8

Gagné, J., et al. 2016, ApJ, 822, 40

Gray, D. F. 2008, The Observation and Analysis of Stellar Photospheres

Gray, R. O., & Corbally, J., C. 2009, Stellar Spectral Classification

Greene, T. P., Tokunaga, A. T., Toomey, D. W., & Carr, J. B. 1993, in Proc. SPIE, Vol. 1946, Infrared Detectors and Instrumentation, ed. A. M. Fowler, 313–324

Hatzes, A. P. 2002, Astronomische Nachrichten, 323, 392

Hébrard, É. M., Donati, J.-F., Delfosse, X., Morin, J., Moutou, C., & Boisse, I. 2016, MNRAS, 461, 1465

Hernán-Obispo, M., De Castro, E., Cornide, M., Crespo-Chacón, I., Gálvez, M. C., & López-Santiago, J. 2005, in ESA Special Publication, Vol. 560, 13th Cambridge Workshop on Cool Stars, Stellar Systems and the Sun, ed. F. Favata, G. A. J. Hussain, & B. Battrick, 647

Hernán-Obispo, M., Gálvez-Ortiz, M. C., Anglada-Escudé, G., Kane, S. R., Barnes, J. R., de Castro, E., & Cornide, M. 2010, A&A, 512, A45

Hernán-Obispo, M., et al. 2015, A&A, 576, A66

Hewett, P. C., Irwin, M. J., Bunclark, P., Bridgeland, M. T., Kibblewhite, E. J., He, X. T., & Smith, M. G. 1985, MNRAS, 213, 971

Hirano, T., Sanchis-Ojeda, R., Takeda, Y., Winn, J. N., Narita, N., & Takahashi, Y. H. 2014, ApJ, 783, 9

Høg, E., et al. 2000, A&A, 355, L27

Holmberg, J., Nordström, B., & Andersen, J. 2007, A&A, 475, 519

Hooten, J. T., & Hall, D. S. 1990, ApJS, 74, 225

Horne, K. 1986, PASP, 98, 609

Houdashelt, M. L., Bell, R. A., & Sweigart, A. V. 2000, AJ, 119, 1448

Howard, A. W., et al. 2010, Science, 330, 653

Huélamo, N., et al. 2008, A&A, 489, L9

Husser, T.-O., Wende-von Berg, S., Dreizler, S., Homeier, D., Reiners, A., Barman, T., & Hauschildt, P. H. 2013, A&A, 553, A6

Johns-Krull, C. M., et al. 2016, ApJ, 826, 206

Jurić, M., & Tremaine, S. 2008, ApJ, 686, 603

Kasper, M., Apai, D., Janson, M., & Brandner, W. 2007, A&A, 472, 321

King, J. R., Villarreal, A. R., Soderblom, D. R., Gulliver, A. F., & Adelman, S. J. 2003, AJ, 125, 1980

Kiss, L. L., et al. 2011, MNRAS, 411, 117

Koen, C., & Eyer, L. 2002, MNRAS, 331, 45

Lafrenière, D., et al. 2007, ApJ, 670, 1367

Lagrange, A.-M., Meunier, N., Chauvin, G., Sterzik, M., Galland, F., Lo Curto, G., Rameau, J., & Sosnowska, D. 2013, A&A, 559, A83

Latham, D. W., Stefanik, R. P., Mazeh, T., Mayor, M., & Burki, G. 1989, Nature, 339, 38

Livingston, W., & Wallace, L. 1991, An atlas of the solar spectrum in the infrared from 1850 to 9000 cm-1 (1.1 to 5.4 micrometer)

López-Santiago, J., Montes, D., Gálvez-Ortiz, M. C., Crespo-Chacón, I., Martínez-Arnáiz, R. M., Fernández-Figueroa, M. J., de Castro, E., & Cornide, M. 2010, A&A, 514, A97

Mahmud, N. I., Crockett, C. J., Johns-Krull, C. M., Prato, L., Hartigan, P. M., Jaffe, D. T., & Beichman, C. A. 2011, ApJ, 736, 123

Mamajek, E. E., & Hillenbrand, L. A. 2008, ApJ, 687, 1264

Mann, A. W., et al. 2016, AJ, 152, 61

Martin, R. G., & Livio, M. 2012, MNRAS, 425, L6

Mateo, M., Bailey, J. I., Crane, J., Shectman, S., Thompson, I., Roederer, I., Bigelow, B., & Gunnels, S. 2012, in Proc. SPIE, Vol. 8446, Ground-based and Airborne Instrumentation for Astronomy IV, 84464Y

Mayor, M., Lovis, C., Pepe, F., Ségransan, D., & Udry, S. 2011, in Reviews in Modern Astronomy, Vol. 23, Reviews in Modern Astronomy, ed. R. von Berlepsch, 1

McCarthy, K., & White, R. J. 2012, AJ, 143, 134

McCarthy, K., & Wilhelm, R. J. 2014, AJ, 148, 70

Meibom, S., Barnes, S. A., Platais, I., Gilliland, R. L., Latham, D. W., & Mathieu, R. D. 2015, Nature, 517, 589

Meschiari, S., Wolf, A. S., Rivera, E., Laughlin, G., Vogt, S., & Butler, P. 2009, PASP, 121, 1016

Messina, S. 1998, PhD thesis, Catania Astrophysical Observatory; University of Catania

Messina, S., Desidera, S., Turatto, M., Lanzafame, A. C., & Guinan, E. F. 2010, A&A, 520, A15

Moór, A., Kóspál, Á., Ábrahám, P., Balog, Z., Csengeri, T., Henning, T., Juhász, A., & Kiss, C. 2016, ArXiv e-prints

Morlet, G., Salaman, M., & Gili, R. 2000, A&AS, 145, 67

Morton, T. D., & Winn, J. N. 2014, ApJ, 796, 47

Moutou, C., Boisse, I., Hébrard, G., Hébrard, E., Donati, J.-F., Delfosse, X., & Kouach, D. 2015, in SF2A-2015: Proceedings of the Annual meeting of the French Society of Astronomy and Astrophysics, ed. F. Martins, S. Boissier, V. Buat, L. Cambrésy, & P. Petit, 205–212

Nielsen, E. L., & Close, L. M. 2010, ApJ, 717, 878

Osten, R. A., & Saar, S. H. 1998, MNRAS, 295, 257

Paulson, D. B., Cochran, W. D., & Hatzes, A. P. 2004, AJ, 127, 3579

Paulson, D. B., & Yelda, S. 2006, PASP, 118, 706

Pollack, J. B., Hubickyj, O., Bodenheimer, P., Lissauer, J. J., Podolak, M., & Greenzweig, Y. 1996, Icarus, 124, 62

Prato, L. 2007, ApJ, 657, 338

Prato, L., Huerta, M., Johns-Krull, C. M., Mahmud, N., Jaffe, D. T., & Hartigan, P. 2008, ApJ, 687, L103

Queloz, D., et al. 2001, A&A, 379, 279

Quinn, S. N., et al. 2012, ApJ, 756, L33

—. 2014, ApJ, 787, 27

Reid, I. N., et al. 2004, AJ, 128, 463

Reiners, A. 2009, A&A, 498, 853

Ricker, G. R., et al. 2016, in Proc. SPIE, Vol. 9904, Society of Photo-Optical Instrumentation Engineers (SPIE) Conference Series, 99042B

Riddle, R. L., et al. 2015, ApJ, 799, 4

Roberts, Jr., L. C., Tokovinin, A., Mason, B. D., Hartkopf, W. I., & Riddle, R. L. 2015, AJ, 150, 130

Saar, S. H., & Donahue, R. A. 1997, ApJ, 485, 319

Santos, N. C., Israelian, G., & Mayo, M. 2004, in IAU Symposium, Vol. 202, Planetary Systems in the Universe, ed. A. Penny, 118

Santos, N. C., et al. 2002, A&A, 392, 215

Setiawan, J., Henning, T., Launhardt, R., Müller, A., Weise, P., & Kürster, M. 2008, Nature, 451, 38

Simon, M., & Schaefer, G. H. 2011, ApJ, 743, 158

Skumanich, A. 1972, ApJ, 171, 565

Tokunaga, A. T., Bus, S. J., Connelley, M., & Rayner, J. 2016, in AAS/Division for Planetary Sciences Meeting Abstracts, Vol. 48, AAS/Division for Planetary Sciences Meeting Abstracts, 123.39

Tokunaga, A. T., Toomey, D. W., Carr, J., Hall, D. N. B., & Epps, H. W. 1990, in Proc. SPIE, Vol. 1235, Instrumentation in Astronomy VII, ed. D. L. Crawford, 131–143

Torres, C. A. O., Quast, G. R., da Silva, L., de La Reza, R., Melo, C. H. F., & Sterzik, M. 2006, A&A, 460, 695

Torres, C. A. O., Quast, G. R., Melo, C. H. F., & Sterzik, M. F. 2008, , 757

Torres, R. M., Loinard, L., Mioduszewski, A. J., & Rodríguez, L. F. 2009, ApJ, 698, 242

Valenti, J. A., & Fischer, D. A. 2005, in Protostars and Planets V Posters, Vol. 1286, 8592

van Leeuwen, F. 2007, A&A, 474, 653

Weise, P., Launhardt, R., Setiawan, J., & Henning, T. 2010, A&A, 517, A88

White, R. J., Gabor, J. M., & Hillenbrand, L. A. 2007, AJ, 133, 2524

Winn, J. N., & Fabrycky, D. C. 2015, ARA&A, 53, 409

Wright, J. T., & Eastman, J. D. 2014, PASP, 126, 838

Wright, J. T., Marcy, G. W., Howard, A. W., Johnson, J. A., Morton, T. D., & Fischer, D. A. 2012, ApJ, 753, 160

Zuckerman, B., Rhee, J. H., Song, I., & Bessell, M. S. 2011, ApJ, 732, 61

Zuckerman, B., & Song, I. 2004, ARA&A, 42, 685

Appendices

– A –

Optical Spectroscopy Data Tables

Table A.1. Optical Spectroscopic Data of HD 152555 with TRES

BJD	RV (m/s)	RV error (m/s)	$v \sin i$ (km/s)	SNR (per pixel)
56106.778181	-15.77	34.29	–	35.3
56107.838175	-34.42	18.08	–	60.8
56108.761790	0.00	13.52	–	82.6
56108.767872	-7.93	14.52	–	77.3
56108.776685	24.91	14.99	–	76.7
56108.782026	24.12	13.52	–	74.4
56115.664064	3.59	21.06	–	76.6
56115.669231	1.76	17.50	–	75.6
56115.675111	16.14	21.06	–	73.9
56115.680267	13.34	20.14	–	75.3
56115.685718	-2.32	16.30	–	76.0
56176.650605	70.76	28.58	–	34.9
56178.699395	69.29	38.15	–	25.9
56195.601413	-1.90	27.68	–	33.2
56196.593970	10.65	20.88	–	61.8
56199.585221	-66.95	24.78	–	36.8
56200.581965	44.59	27.65	–	45.6
56203.580231	84.13	23.90	–	51.3
56204.582290	85.68	25.63	–	46.0
56206.582150	63.68	38.94	–	27.5
56207.584523	7.48	29.84	–	45.5
56208.584108	-94.19	22.10	–	48.1
56210.574103	-20.79	22.57	–	34.0

Table A.2. Optical Spectroscopic Data of HD 17332A with TRES

BJD	RV (m/s)	RV error (m/s)	$v \sin i$ (km/s)	SNR (per pixel)
56193.812915	21.01	18.09	–	47.7
56194.844820	63.31	16.53	–	91.2
56196.951556	0.00	16.53	–	87.5
56201.832110	16.79	16.60	–	51.4
56204.900338	110.40	27.95	–	34.7
56205.831846	44.29	17.38	–	50.8
56223.838288	40.50	19.22	–	66.2
56224.749571	145.16	17.33	–	53.6
56225.793436	36.10	18.92	–	47.2
56226.805251	-14.47	19.48	–	57.2

Table A.3. Optical Spectroscopic Data of HD 17332B with TRES

BJD	RV (m/s)	RV error (m/s)	$v \sin i$ (km/s)	SNR (per pixel)
56193.814831	-23.52	10.79	–	37.4
56194.847737	0.00	8.47	–	62.6
56201.833580	-23.59	10.31	–	52.6
56204.901947	31.37	13.20	–	34.8
56205.833432	-3.82	8.47	–	49.0
56223.840579	4.45	10.91	–	48.9
56224.751018	-3.17	11.29	–	54.5
56225.795346	-38.84	11.02	–	45.2
56226.806860	-14.16	9.72	–	55.9

Table A.4. Optical Spectroscopic Data of BD+20 1790 with SOPHIE

BJD	RV (m/s)	RV error (m/s)	$v \sin i$ (km/s)	SNR (at 500 nm)
56217.60175	7.95145	0.012284	8.96	38.4
56217.64655	7.87814	0.016946	9.02	30.8
56218.61676	7.62843	0.012335	8.51	37.6
56219.54315	8.10290	0.012469	8.49	38.1
56219.59813	8.08971	0.011637	8.47	39.0
56219.64805	8.10365	0.004548	8.48	82.3
56221.63004	7.70975	0.011822	8.43	38.2
56221.69160	7.73890	0.014038	8.43	33.5
56223.66907	7.46436	0.011892	8.55	38.7
56224.55745	7.74800	0.011416	8.39	39.1
56224.57416	7.75114	0.011265	8.43	39.4
56224.59666	7.78033	0.011068	8.35	39.6
56225.53649	8.08416	0.011671	8.47	39.2
56225.57131	8.06033	0.011479	8.43	39.2
56225.58679	8.08200	0.011438	8.38	39.2
56251.44505	7.59272	0.012335	8.90	39.6
56251.54693	7.61367	0.011756	8.73	39.3
56251.61180	7.56016	0.011463	8.62	39.3
56252.45206	7.58806	0.011380	8.55	39.6
56252.51333	7.60180	0.011131	8.42	39.3
56252.55798	7.62924	0.011016	8.37	39.5
56252.58648	7.62036	0.010986	8.34	39.3
56252.67979	7.70864	0.010999	8.28	39.2
56252.71911	7.72400	0.010958	8.27	39.4
56548.66647	8.00296	0.008801	8.36	48.1
56571.59405	7.79241	0.008258	8.69	58.9
56571.66989	7.79821	0.006393	8.36	61.3
56574.56833	7.77714	0.008143	8.78	59.1
56574.66557	7.71069	0.005022	8.58	76.5
56575.62313	7.94486	0.006166	8.08	62.0
56576.60376	7.94405	0.010349	8.53	42.9
56576.67053	7.93665	0.008109	8.48	51.2

Table A.5. Optical Spectroscopic Data of HD 377 with SOPHIE

BJD	RV (m/s)	RV error (m/s)	$v \sin i$ (km/s)	SNR (at 500 nm)
56545.44702	1.16582	0.006866	14.24	93.6
56545.48982	1.16098	0.006838	14.22	93.3
56545.50366	1.16521	0.006827	14.24	93.5
56546.53728	1.28931	0.006832	14.25	93.2
56546.59990	1.27411	0.006844	14.24	93.5
56547.44119	1.17081	0.006855	14.16	93.8
56547.47449	1.17089	0.006822	14.17	93.6
56547.55911	1.16501	0.006811	14.13	93.6
56548.49267	1.11145	0.006844	14.21	93.4
56548.52312	1.11775	0.006838	14.17	93.3
56549.39911	1.13357	0.006817	14.17	94.4
56549.43050	1.14786	0.006756	14.14	94.1
56571.36358	1.22451	0.006808	14.12	94.0
56571.42604	1.24043	0.006811	14.11	93.7
56571.51981	1.24839	0.006794	14.14	94.0
56572.33453	1.18012	0.006762	14.28	94.8
56572.38939	1.16087	0.006775	14.33	94.1
56572.47381	1.15952	0.006770	14.27	94.1
56572.52871	1.14499	0.010669	14.30	62.7
56573.32469	1.19702	0.007504	14.64	103.0
56573.39908	1.19944	0.006928	14.33	92.1
56574.39722	1.14482	0.006779	14.08	94.3
56574.44804	1.14227	0.006732	14.06	94.5
56575.31324	1.21314	0.007457	14.41	105.0
56575.42432	1.26287	0.010814	14.08	61.8
56576.33643	1.16993	0.011503	14.05	58.1
56576.41104	1.20930	0.006781	13.99	92.5
56576.51297	1.24197	0.006782	14.03	93.4

Table A.6. Optical Spectroscopic Data of HD 38230 with SOPHIE

BJD	RV (m/s)	RV error (m/s)	$v \sin i$ (km/s)	SNR (at 500 nm)
56217.45793	-28.9986	0.001788	2.07	96.1
56217.53833	-28.9919	0.001803	2.09	94.6
56218.44760	-28.9941	0.001825	2.11	95.8
56218.49215	-28.9972	0.001819	2.10	94.8
56218.64071	-28.9970	0.001805	2.07	94.3
56219.47637	-28.9937	0.001822	2.09	94.5
56219.49724	-28.9918	0.001811	2.09	94.6
56219.67458	-28.9954	0.001239	2.10	204.3
56220.61255	-28.9487	0.001836	2.07	92.4
56221.61871	-28.9900	0.001794	2.06	94.3
56221.66294	-28.9907	0.001799	2.05	94.3
56223.66080	-28.9892	0.001812	2.07	93.7
56224.54852	-28.9913	0.001807	2.07	93.9
56224.56785	-28.9908	0.001804	2.07	93.8
56224.60471	-28.9937	0.001788	2.06	94.7
56225.50355	-28.9948	0.001800	2.09	94.9
56225.56535	-28.9927	0.001795	2.05	94.2
56225.58055	-28.9892	0.001800	2.06	94.0
56251.36084	-28.9959	0.001803	2.12	95.3
56251.54135	-28.9896	0.001783	2.07	94.2
56251.60690	-28.9950	0.001780	2.08	94.2
56251.72160	-28.9893	0.001785	2.10	95.5
56252.36745	-28.9956	0.001796	2.11	95.4
56252.41256	-28.9922	0.001787	2.09	95.0
56252.49969	-28.9934	0.001783	2.06	94.1
56252.57104	-28.9937	0.001781	2.06	93.9
56252.67406	-28.9927	0.001784	2.09	94.7
56252.71400	-28.9962	0.001795	2.10	94.7
56253.60638	-28.9914	0.001806	2.08	93.7
56545.53645	-28.9943	0.001906	2.39	105.8
56545.57982	-28.9979	0.002129	2.09	77.5
56546.63553	-28.9959	0.001881	2.11	89.4
56547.59392	-28.9950	0.001773	2.11	97.0
56547.62919	-28.9945	0.001771	2.10	96.7
56548.53521	-28.9952	0.001866	2.32	103.2
56548.58374	-28.9983	0.001772	2.12	97.2
56549.66399	-29.0004	0.001754	2.09	96.9
56571.49885	-28.9968	0.001757	2.10	97.6
56571.62888	-29.0027	0.001750	2.10	97.2
56572.48731	-28.9971	0.001760	2.12	97.8
56574.48641	-28.9959	0.001758	2.12	97.9
56575.50722	-28.9979	0.001760	2.11	97.3

Table A.7. Optical Spectroscopic Data of HD 138004 with SOPHIE

BJD	RV (m/s)	RV error (m/s)	$v \sin i$ (km/s)	SNR (at 500 nm)
56439.43611	-15.0119	0.002037	2.85	93.3
56439.48272	-15.0055	0.002024	2.86	93.4
56439.53157	-15.0017	0.002017	2.84	93.5
56440.38662	-15.0055	0.002051	2.85	93.8
56440.41974	-15.0073	0.002044	2.85	93.7
56441.44769	-15.0054	0.002045	2.85	92.9
56441.49334	-15.0075	0.002026	2.85	93.1
56441.58892	-15.0021	0.002043	2.85	93.6
56442.36201	-15.0091	0.002043	2.85	93.2
56442.41661	-15.0088	0.002036	2.84	92.9
56442.47571	-15.0064	0.002020	2.85	93.5
56442.54086	-15.0079	0.002022	2.85	93.8
56443.37764	-15.0075	0.002035	2.84	93.0
56443.47908	-15.0044	0.002041	2.85	93.0
56443.54186	-15.0038	0.002037	2.84	93.3
56444.36601	-15.0063	0.002053	2.86	92.4
56444.43702	-15.0026	0.002036	2.85	92.7
56444.47571	-15.0063	0.002034	2.85	92.8
56445.38148	-15.0085	0.002043	2.85	92.8
56460.36381	-15.0052	0.002012	2.84	93.4
56460.43770	-15.0104	0.002018	2.83	93.6
56460.53695	-15.0041	0.002021	2.83	93.8
56462.36179	-15.0027	0.002023	2.84	93.2
56464.36602	-15.0013	0.002020	2.83	92.8
56465.36208	-15.0048	0.002031	2.83	93.3
56466.36265	-15.0063	0.002024	2.84	93.1
56801.49550	-14.8857	0.001750	2.93	97.1
56801.54011	-14.8834	0.001751	2.96	98.5
56802.53633	-14.8828	0.001754	2.94	98.4
56803.53110	-14.8816	0.001752	2.96	99.1
56803.59985	-14.8922	0.001815	3.04	101.5
56804.54084	-14.8841	0.001757	2.95	98.3
56804.58835	-14.8882	0.001771	2.98	99.4
56805.42537	-14.8830	0.001739	2.93	97.2
56805.46040	-14.8858	0.001738	2.94	97.3
56805.51150	-14.8849	0.001729	2.94	98.0
56805.53641	-14.8840	0.001748	2.96	98.8
56806.39420	-14.8805	0.001743	2.94	98.2
56806.42083	-14.8792	0.001734	2.94	97.7
56806.44517	-14.8843	0.001732	2.93	97.6
56806.49026	-14.8852	0.001736	2.95	98.0
56822.37409	-14.8645	0.001728	2.93	97.8
56823.36996	-14.8704	0.001737	2.93	98.4
56825.39934	-14.8715	0.001756	2.95	98.0
56827.37152	-14.8663	0.001719	2.92	98.1
56827.45572	-14.8740	0.001738	2.96	99.8

Table A.8. Optical Spectroscopic Data of HD 189285 with SOPHIE

BJD	RV (m/s)	RV error (m/s)	$v \sin i$ (km/s)	SNR (at 500 nm)
56439.55098	-19.0863	0.009353	9.24	49.2
56439.59587	-19.0741	0.008511	9.12	47.1
56441.54902	-18.9928	0.009606	9.15	46.4
56441.60625	-18.9654	0.008685	9.05	46.5
56442.59979	-18.9477	0.016478	9.01	28.3
56443.56748	-18.9338	0.008658	9.27	46.9
56443.59409	-18.9293	0.010770	9.25	39.4
56444.59157	-19.0603	0.020805	9.11	24.3
56460.46196	-19.0432	0.009961	9.33	53.5
56460.51686	-18.9948	0.008230	9.01	48.0
56460.55890	-19.0040	0.008228	9.06	47.9
56462.49629	-18.8828	0.013230	9.32	40.5
56462.57134	-18.8251	0.027514	9.15	19.8
56464.48528	-19.0114	0.011053	9.22	42.5
56464.55216	-19.0239	0.008560	9.18	46.9
56465.48282	-19.0075	0.009701	9.20	49.6
56465.57543	-19.0050	0.008332	9.08	47.6
56466.47090	-18.9628	0.009666	9.13	48.0
56466.53676	-18.9533	0.008409	9.00	47.4
56466.57939	-18.9256	0.008344	9.04	47.6
56801.59917	-19.0060	0.013737	9.24	35.0
56803.57618	-18.9197	0.017970	9.25	29.7
56806.56058	-19.0084	0.007667	9.31	58.9
56806.60294	-18.9917	0.011628	9.30	41.0
56822.51530	-18.9895	0.009510	9.14	44.6
56822.56999	-19.0049	0.012832	9.17	38.4
56822.60040	-18.9976	0.012974	9.18	37.8
56823.50378	-18.9349	0.014277	9.22	34.8
56825.55848	-19.0124	0.008523	9.28	53.1
56825.59915	-19.0126	0.010902	9.30	45.5
56827.49384	-18.9900	0.010155	9.09	40.9
56827.57132	-19.0012	0.010514	9.22	44.6

Table A.9. Optical Spectroscopic Data of IS Eri with SOPHIE

BJD	RV (m/s)	RV error (m/s)	$v \sin i$ (km/s)	SNR (at 500 nm)
56218.47850	14.6874	0.003618	6.77	75.3
56218.51483	14.6805	0.003574	6.74	75.3
56219.46464	14.7779	0.003594	6.70	75.2
56219.51115	14.7793	0.003569	6.73	75.1
56219.58836	14.7716	0.003613	6.72	75.4
56220.54485	14.7530	0.003357	6.70	80.0
56221.60196	14.7083	0.003595	6.78	75.5
56224.48255	14.7271	0.003542	6.62	75.3
56224.51875	14.7400	0.003537	6.61	75.3
56225.49205	14.7366	0.003540	6.74	76.2
56225.52794	14.7357	0.003549	6.72	75.7
56225.55234	14.7342	0.003569	6.72	75.8
56251.38797	14.7176	0.003512	6.62	75.8
56251.47556	14.7314	0.003489	6.64	76.1
56252.38806	14.7389	0.003511	6.69	75.9
56252.44395	14.7331	0.003503	6.68	76.2
56252.50683	14.7332	0.003507	6.70	75.9
56546.57894	14.7204	0.004776	6.92	64.8
56546.61934	14.7189	0.005540	6.77	52.1
56547.57715	14.6746	0.003697	6.81	80.4
56547.61518	14.6844	0.003729	6.83	81.0
56548.60294	14.6797	0.003788	6.93	82.0
56548.65243	14.6830	0.003510	6.71	76.9
56549.58966	14.7450	0.003837	6.96	83.6
56549.62414	14.7621	0.003463	6.74	77.5
56571.48729	14.6944	0.003903	7.03	85.0
56571.62290	14.6991	0.003493	6.75	77.7
56572.50826	14.7463	0.003921	6.97	85.9
56574.50196	14.6820	0.004027	7.09	88.0
56574.60070	14.7033	0.003451	6.69	77.5
56575.49535	14.6659	0.003958	7.03	85.8
56576.49281	14.6959	0.006482	6.79	48.5

Table A.10. Optical Spectroscopic Data of V577 Per A with SOPHIE

BJD	RV (m/s)	RV error (m/s)	$v \sin i$ (km/s)	SNR (at 500 nm)
56217.38647	-5.35519	0.004670	9.11	75.1
56217.46969	-5.37194	0.004661	9.09	74.5
56218.43594	-5.41431	0.004687	8.94	74.7
56218.53433	-5.38759	0.004362	8.96	79.1
56219.41981	-5.33847	0.004730	9.04	74.5
56219.56198	-5.33647	0.004744	9.04	74.0
56220.40288	-5.30652	0.004772	9.10	74.9
56220.66042	-5.36958	0.004748	9.13	73.8
56221.61317	-5.39927	0.004667	8.92	74.1
56221.67406	-5.39062	0.004658	8.95	74.4
56224.45771	-5.46286	0.004724	9.00	74.0
56224.53317	-5.45836	0.004663	8.95	74.0
56224.54051	-5.45415	0.004669	8.96	74.1
56225.48303	-5.36045	0.004706	9.05	74.4
56225.56094	-5.36138	0.004705	9.05	74.1
56225.60518	-5.36162	0.004685	9.04	74.5
56251.31041	-5.33647	0.004719	9.05	74.8
56251.38058	-5.33241	0.004696	9.07	74.3
56251.46880	-5.33172	0.004679	9.10	74.2
56251.60195	-5.34289	0.004702	9.16	74.9
56251.71637	-5.35603	0.004754	9.19	75.8
56252.32339	-5.38450	0.004679	9.09	74.6
56252.40704	-5.38661	0.004640	9.07	74.4
56252.49451	-5.37998	0.004647	9.05	74.2
56252.56608	-5.37122	0.004639	9.03	74.1
56252.65778	-5.36909	0.004683	9.03	75.1
56253.59545	-5.38202	0.004726	9.07	73.9
56545.50981	-5.24143	0.004649	9.14	76.2
56545.51924	-5.24644	0.004641	9.11	76.1
56545.56238	-5.25396	0.004956	9.11	71.7
56546.45510	-5.42804	0.004689	9.08	76.1
56546.51773	-5.42554	0.004680	9.10	75.9
56547.45430	-5.45218	0.004725	9.10	76.5
56547.48387	-5.45102	0.004684	9.08	76.4
56547.50471	-5.44525	0.004695	9.08	76.0
56548.47271	-5.25940	0.004681	9.06	76.3
56548.50279	-5.24936	0.004651	9.08	76.2
56549.47480	-5.40398	0.004612	9.14	76.7
56549.52473	-5.39958	0.004649	9.12	75.7
56549.57380	-5.40276	0.004583	9.11	76.0
56571.43341	-5.27650	0.004601	9.03	76.5
56571.50783	-5.26818	0.004557	9.02	76.4
56571.63892	-5.27408	0.004555	9.07	76.9
56572.42244	-5.48673	0.004649	9.09	76.4
56572.47961	-5.48269	0.004588	9.05	76.4
56572.54523	-5.46935	0.017664	9.06	26.4
56574.43805	-5.29451	0.004585	9.02	76.9
56574.51095	-5.27091	0.004539	8.99	76.7
56574.61501	-5.25650	0.004524	8.99	77.3
56575.44475	-5.43511	0.004674	9.22	76.7
56575.52102	-5.45894	0.004678	9.19	75.9
56575.67858	-5.49931	0.004631	9.09	76.2
56576.43402	-5.39158	0.005036	9.12	71.2

Table A.11. Optical Spectroscopic Data of V835 Her with SOPHIE

BJD	RV (m/s)	RV error (m/s)	$v \sin i$ (km/s)	SNR (at 500 nm)
56439.44981	1.211160	0.003303	8.88	96.8
56439.47296	2.277400	0.003292	8.86	96.4
56439.52224	4.341850	0.003273	8.86	96.4
56440.40401	-2.28505	0.003260	8.62	97.0
56440.43131	-3.71612	0.003234	8.60	96.9
56441.42833	-52.4972	0.003344	8.73	93.6
56441.47304	-52.9716	0.003282	8.66	94.1
56441.51779	-53.2245	0.003233	8.65	96.0
56442.37737	-20.0877	0.003064	8.81	96.7
56442.40632	-18.4926	0.003178	9.12	96.6
56442.46596	-14.7251	0.003351	9.18	95.8
56442.55471	-9.23791	0.003272	8.58	96.3
56443.38951	9.742760	0.003252	8.68	96.6
56443.50414	6.502910	0.003215	8.60	96.2
56443.52895	5.639590	0.003218	8.61	95.9
56444.39064	-41.5404	0.003841	8.88	84.0
56444.45239	-44.4531	0.003313	8.89	95.8
56444.49223	-46.0683	0.003316	8.89	95.5
56444.53863	-47.7488	0.003315	8.87	95.5
56445.40725	-36.3399	0.003259	8.62	95.7
56460.37172	-10.1294	0.003248	8.49	96.8
56460.44654	-14.7634	0.003297	9.01	96.4
56460.54657	-20.7558	0.002999	8.61	96.4
56462.37372	-9.66282	0.003325	8.71	96.5
56462.43727	-6.04566	0.003290	8.90	96.5
56462.54942	-0.22718	0.003316	8.97	96.1
56464.38775	-48.5188	0.003607	8.85	88.0
56464.53444	-52.1481	0.003291	8.90	95.6
56465.38914	-27.0521	0.003324	8.80	95.9
56465.45201	-23.4478	0.003430	9.23	92.2
56465.52393	-19.2671	0.003086	8.90	95.9
56465.58640	-15.4658	0.003355	9.37	96.7
56466.37385	12.01070	0.003306	8.85	96.4
56466.45077	11.23620	0.003262	8.85	96.3
56466.56259	8.909410	0.003260	8.88	96.7

Table A.12. Optical Spectroscopic Data of BD+05 4576 with SOPHIE

BJD	RV (m/s)	RV error (m/s)	$v \sin i$ (km/s)	SNR (at 500 nm)
56439.57324	-37.71820	0.010250	2.00	31.1
56822.49511	23.79350	0.010372	2.27	30.3
56825.53079	-25.94390	0.007652	3.20	43.2
56827.47367	-19.21900	0.009753	3.03	31.8
56827.55125	-18.92380	0.008524	3.14	36.7

– B –

Near-Infrared Spectroscopy Data Tables

Table B.1. Near-Infrared Observations of HD 189285 with CSHELL

BJD	RV (m/s)	RV error (m/s)	$v \sin i$ (km/s)	SNR (per pixel)
56432.51953	-17.98	0.0249523	12.6937	127.025
56436.55859	-18.029	0.0265728	12.7989	129.964
56459.57813	-18.653	0.020517	13.3326	168.715
56467.45313	-18.654	0.0220518	13.4128	158.546
56467.59766	-18.734	0.026967	12.8981	122.966
56793.50781	-18.376	0.0226234	13.0008	137.431
56793.57422	-18.222	0.0291579	12.9103	115.646
56795.50000	-18.428	0.0229941	12.4568	134.343
56795.52344	-18.448	0.0250138	12.5169	126.397
56822.46484	-18.9	0.0270987	12.3472	115.696
56822.50000	-19.211	0.0278352	12.5015	116.324

Table B.2. Near-Infrared Observations of HD 38230 with CSHELL

BJD	RV (m/s)	RV error (m/s)	$v \sin i$ (km/s)	SNR (per pixel)
56219.56641	-28.543	0.0157172	0	176.811
56219.65234	-28.844	0.0163316	7.14915	160.312
56223.48828	-28.694	0.031776	3.76357	80.7517
56223.49609	-28.581	0.0223145	7.207	119.109
56255.61328	-28.373	0.009311	3.76196	249.955
56256.52344	-28.253	0.0130795	7.35835	188.97
56256.60547	-28.312	0.011021	3.24545	209.868
56256.64453	-28.407	0.0123692	3.51311	176.343
56530.58203	-28.651	0.0088302	8.88E-16	229.862
56573.58203	-28.808	0.0096009	6.49678	263.227

Table B.3. Near-Infrared Observations of IS Eri with CSHELL

BJD	RV (m/s)	RV error (m/s)	$v \sin i$ (km/s)	SNR (per pixel)
56219.52734	15.5752	0.0193733	6.14321	157.835
56219.60156	15.6125	0.0171726	5.34005	159.372
56223.44922	15.3258	0.0187323	5.80998	157.628
56255.48828	15.2852	0.0182873	6.4218	156.397
56256.44922	15.4214	0.0243184	6.93278	121.122
56256.47266	15.5242	0.0214518	6.56357	134.838
56524.57031	15.259	0.0202211	3.4543	223.349
56526.51563	15.0006	0.0148795	4.80144	197.815
56526.56641	14.8871	0.0156085	3.87628	199.821
56528.53516	14.8077	0.0154537	5.21223	207.272
56528.58984	14.8147	0.0156194	4.51369	216.636
56573.53125	15.108	0.0145181	4.86799	207.72
56573.60547	15.3839	0.0142511	2.52673	189.65

Table B.4. Near-Infrared Observations of V577 Per A with CSHELL

BJD	RV (m/s)	RV error (m/s)	$v \sin i$ (km/s)	SNR (per pixel)
56219.54688	-4.8051	0.0253894	9.67539	135.577
56219.62109	-4.8622	0.0277439	9.4662	114.991
56223.54688	-4.7179	0.0245945	8.66507	136.203
56255.46094	-4.4101	0.0211743	5.44934	202.195
56255.57422	-4.6112	0.0189308	11.5277	195.775
56256.50000	-4.6653	0.0213654	5.46385	178.901
56256.54297	-4.6102	0.0160731	11.3179	234.386
56528.49219	-4.6412	0.0176142	10.9642	180.691
56528.62891	-4.6422	0.018513	10.5885	191.039
56530.55469	-4.5474	0.0139515	11.0769	240.531
56530.59766	-4.765	0.0158256	11.2069	213.96
56573.56250	-4.9145	0.018188	9.99442	187.909

Table B.5. Near-Infrared Observations of BD+20 1790 with CSHELL

BJD	RV (m/s)	RV error (m/s)	$v \sin i$ (km/s)	SNR (per pixel)
56219.57813	7.78747	0.0327932	17.3093	122.561
56255.52344	7.41168	0.0375074	17.8403	111.36
56255.54688	7.37141	0.0364256	16.9325	110.721
56255.63672	8.10589	0.0245664	17.8018	166.575
56256.57031	7.55832	0.0322993	18.0006	135.649
56256.62500	7.69585	0.0264235	18.3567	161.777